

STRETCHABLE STRAIN SENSORS MADE OF MULTI-WALL CARBON NANOTUBE-BASED COMPOSITE

Xiang Fu

Phd

2018



AUCKLAND, NEW ZEALAND
SUPERVISORS: Dr. Maximiano Ramos
Prof. Ahmed Al-Jumaily

Stretchable Strain Sensors Made of Multi-Wall Carbon Nanotube-Based Composite

Xiang Fu

A thesis submitted to Auckland University of Technology
in fulfilment of the requirements for the degree of

Doctor of Philosophy (PhD)

2018

Faculty of Design & Creative Technology

School of Engineering

Institute of Biomedical Technologies

Auckland University of Technology

Auckland, New Zealand

Declarations

I hereby declare that this submission is my own work and that, to the best of my knowledge and belief, it contains no material previously published or written by another person non material which to substantial extent has been accepted for the award of any other degree or diploma of a university or other institution of higher learning, except where due acknowledgement is made in the acknowledgments

Signature

Date

Xiang Fu

I further authorize the Auckland University of Technology to reproduce this thesis by photocopying or by other means, in total or in part, at the request of other institutions or individuals for the sole purpose of scholarly research.

Signature

Date

Xiang Fu

Borrowers Page

The Auckland University of Technology requires the signatures of all people using or photocopying this thesis. Accordingly, all borrowers are required to fill out this page.

Date

Name

Address

Signature

Acknowledgements

First and foremost, I appreciate Auckland University of Technology's Institute of Biomedical Technologies for giving me a comfortable learning atmosphere for three years. Second, I would like to show my deepest gratitude to my supervisors, Dr. Maximiano Ramos and Prof. Ahmed M.Al-Jumaily, both of who have walked me through all the stages of the writing of this thesis. Without their illuminating instruction and patience, this thesis could not have reached its present form. Third, I would like to express my heartfelt gratitude to technicians Jim Crossen and Mark Masterton at the mechanical workshop, both of who give me a great help on doing mechanical tests. I would like to thank research officer Tao Yuan from faculty of Design & Creative Technologies for helping in taking SEM images. Fourthly, I would like to appreciate that the Auckland University of Technology Ethics Committee (AUTECH) approved my ethics application (18/354). Lastly my thanks would go to my beloved family for their loving considerations and great confidence in me all through these years. I also owe my sincere gratitude to my friends and my fellow classmates who gave me their help and time in listening to me and helping me work out my problems during the difficult course of the thesis.

Table of Contents

Declarations	i
Borrowers Page	ii
Acknowledgements.....	iii
Table of Contents	iv
List of Figures.....	viii
List of Tables	xii
Abstract.....	xiii
Abbreviations	xv
Symbols	xvii
Chapter 1 Introduction.....	1
<i>1.1 Background.....</i>	<i>1</i>
<i>1.2 Research Motivation and Objectives</i>	<i>3</i>
<i>1.3 Thesis Overview.....</i>	<i>5</i>
Chapter 2 Literature Review.....	7
<i>2.1 Introduction</i>	<i>7</i>
<i>2.2 Carbon Nanotubes.....</i>	<i>8</i>
<i>2.2.1 Structure of Carbon nanotubes</i>	<i>8</i>
<i>2.2.2 Properties of Carbon nanotubes</i>	<i>10</i>

2.3 Composite based on Carbon Nanotubes.....	12
2.3.1 Dispersion of CNTs.....	12
2.3.2 The Interaction between CNTs and Polymers.....	17
2.3.3 Fabrication of CNTs/polymer composite.....	22
2.3.4 Electrical Properties of Carbon Nanotubes-based Composite.....	24
2.4 Stretchable Strain Sensor	27
2.4.1 Transduction Mechanism for Sensing.....	27
2.4.2 Performance of Stretchable Strain Sensor	31
2.4.3 Applications.....	36
2.4 Summary	39
Chapter 3 Computational Analysis of Electrical Properties.....	41
3.1 Introduction	41
3.2 Modelling and Simulation	43
3.2.1 Building the Model.....	43
3.2.2 Resistance Calculation.....	45
3.3 Static Electrical Behavior Analysis	50
3.3.1 Influence of CNT Volume Fraction	51
3.3.2 Influence of CNTs Polar Angles.....	54
3.4 Piezoresistivity Analysis	54
3.4.1 Effect of CVF on Piezoresistivity.....	55
3.4.2 Effect of AR on Piezoresistivity	56
3.4.3 Effect of PR of Matrix on Piezoresistivity	58

3.5 Conclusion.....	59
Chapter 4 Preparation of the MWCNTs/PDMS Composite	61
4.1 Introduction	61
4.2 Experimental Investigation.....	63
4.2.1 Materials	63
4.2.2 Selection of CNTs Concentration.....	63
4.2.3 Preparation of CNTs/PDMS Nanocomposites	65
4.2.4 Characterization of the Nanocomposites	66
4.3 Characterization Results	67
4.3.1 Morphology.....	67
4.3.2 Mechanical Properties	68
4.3.3 Electrical Properties	70
4.4 Conclusion.....	71
Chapter 5 Fabrication and Characterization of the Stretchable Sensor based on the MWCNTs/CNTs Composite	72
5.1 Introduction	72
5.2 Experimental Investigation.....	73
5.2.1 Materials	73
5.2.2 Selection of the Concentration of MWCNTs	74
5.2.3 Sensor Fabrication.....	77
5.2.4 Sensors Characterization	78
5.3 Sensitivity and Hysteresis	79

5.4 Response Time	82
5.5 Durability.....	84
5.6 Human Motions Detection.....	85
5.7 Conclusion.....	89
Chapter 6 Fabrication and Characterization of the Serpentine Sensor.....	91
6.1 Introduction	91
6.2 Experimental Investigation.....	92
6.2.1 Design of the Sensor.....	92
6.2.2 Materials	93
6.2.3 Sensor Fabrication and Characterization.....	93
6.3 Characterization Results	95
6.3.1 Sensitivity	96
6.3.2 Response time.....	101
6.3.3 Hysteresis	103
6.4 Conclusion.....	105
Chapter 7 Summary and Future Work.....	106
7.1 Research Summary	106
7.2 Summary of Contributions.....	107
7.3 Recommendations of Future Work	109
Chapter 8 Appendix: List of MATLAB Programs	110
References	153

List of Figures

Figure 2-1 Schematic diagram showing a CNT is rolled up from a graphene sheet.....	8
Figure 2-2 Schematic diagram showing how a hexagonal sheet of graphene is rolled to form a CNT with different chiralities.	9
Figure 2-3 TEM images of different CNTs (A: SWCNTs; B: MWCNTs with different layers of 5, 2 and 7) ⁴⁹	9
Figure 2-4 Schematic diagram showing the general configuration of a three-roll mill ⁶³	14
Figure 2-5 Functionalization possibilities for SWNTs: A) covalent sidewall functionalization, B) defect-group functionalization, C) noncovalent functionalization with polymers wrapping, D) noncovalent functionalization with surfactants, and, E) endohedral functionalization with guest atoms or molecules ⁹⁶	20
Figure 2-6 The formation process of percolation paths in conductive composites based on CNTs/polymer.....	26
Figure 2-7 Schematic of deformable CNT model with mild deformation and severe deformation ¹²⁸	27
Figure 2-8 (a) Schematic illustration of stretchable transparent ultrasensitive strain sensors attached to face to sense skin strains induced by muscle movements during expression of emotions and daily activities. (b) Schematic illustration of the cross-section of the strain sensor consisting of the three-layer stacked nanohybrid structure of PU-PEDOT:PSS/SWCNT/PU-PEDOT:PSS on a PDMS substrate ¹¹⁹	37
Figure 2-9 Schematic showing the working principle of the electronic skin. The external pressure concentrates stress at the contact spots, deforming the microdomes, which in turn causes an increase in the contact area and the tunneling currents ¹⁵⁶	38
Figure 3-1 (a) Parameters of a 3D CNT, (b) Definition of location and orientation of a CNT and (c) the schematic of an electrical conductive CNTs network and tunneling effect in the resistor network.	44
Figure 3-2 A 3D representative cube model with conductive paths depicted using blue color and bold line.	47

Figure 3-3 The relationship between CNT Volume Fraction and electrical conductivity of the composite with different aspect ratios using linear scale (a) and logarithmic scale (b).....	50
Figure 3-4 (a) The comparison between the Bruggeman theoretical estimation ³⁰⁻³² and the evaluation of electrical conductivity of the composite in this paper and (b) The relationship between the probability of conduction and the CNT Volume Fraction for composites models with different aspect ratios.	52
Figure 3-5 Influence of the electrical conductivity of CNTs on the electrical conductivity of composites and (b) the relationships between the maximum polar angle and the electrical conductivity of the composite as well as the percentage of connected CNTs.	54
Figure 3-6 The relationship between strain and resistance change for composites models (a) with different CNT Volume Fractions and (c) with different aspect ratios as well as CNT Volume Fractions. The correlation between CNT Volume Fraction variation and strain for composites models (b) with different CNT Volume Fractions and (d) with different aspect ratios as well as CNT Volume Fractions.....	56
Figure 3-7 The variation of the distribution state of polar angles of CNTs along with strain increasing.	58
Figure 3-8 The resistance changes and the CNT Volume Fraction variation along with strain growing for composites models with different Poisson's Ratios.....	59
Figure 4-1 The horn ultrasonication device.	65
Figure 4-2 The schematic of the MWCNTs/PDMS nanocomposite film fabrication.....	66
Figure 4-3 The field emission scanning electron microscope (Hitachi SU-70).....	67
Figure 4-4 FESEM images of CNTs/PDMS nanocomposites prepared using different solvents: (a) pentane (b) IPA (c) toluene.....	68
Figure 4-5 The average mechanical properties of the 5% CNTs/PDMS nanocomposite films prepared with different solvents and the neat PDMS film ((a) The tensile modulus, (b) elongations at break and (c) tensile strengths), and (d) The electrical conductivity of the CNTs/PDMS nanocomposite films incorporating 5% CNTs handled by different solvents.	69
Figure 5-1 The average resistance variation of MWCNTs composite with different concentration of MWCNTs upon stretching.....	75

Figure 5-2 (a) Fabrication procedure of the strain sensor based on MWCNTs/PDMS composite with sandwich-like structure. (b) Photographs of the as-prepared sandwich-like strain sensor connected with copper wires. (c) The SEM image of the cross-section of the MWCNTs/PDMS composite.	77
Figure 5-3 The sample are measured under the initial state (a) and stretched state (b) in the tensile test.....	79
Figure 5-4 (a) the curve of relative change in resistance against the applied strain upon stretching in different strain for the sandwich-like sensor. (b) the correlation between the relative variation in resistance versus time subjected stretching of 10% strain at different tension speed.	81
Figure 5-5 the relative change in resistance and the applied strain as a function of time at different tension rates 0.1mm/sec (A), 0.2mm/sec (B), 0.5mm/sec (C), 1mm/sec (D).	82
Figure 5-6 Resistance Response of the strain sensor to the cycle of stretching/releasing with 0%-10% strain variation (a) and 0-20% strain variation (b).....	84
Figure 5-7 (a) the long-term relative variation in resistance of the strain sensor when subjected to the 1000 cycles of stretching/releasing (from 0% to 10% strain). (b) the relative change in resistance of the strain sensor magnified from the red circle part in (a).	85
Figure 5-8. (a) to (j) the curves of relative change in resistance versus time for the strain sensor when subjected to wrist bending from ten volunteers.....	87
Figure 5-9 (a) to (j) the curves of relative change in resistance versus time for the strain sensor when subjected to finger bending from ten volunteers.	89
Figure 6-1 (a) Stretchable Sensor with serpentine MWCNTs/PDMS composite encapsulated by PDMS. (b) Schematic illustration of the structure of the stretchable sensor.	92
Figure 6-2 The schematic of the serpentine shape design.....	93
Figure 6-3 (a) Fabrication procedure of the stretchable strain sensor based on serpentine MWCNTs/PDMS composite via molding technique. (b) The SEM image of the cross-section of the serpentine MWCNTs/PDMS composite. (c)The Cross-sectional SEM image of the stretchable sensor in the interaction zone between MWCNTs/PDMS composite layer and the PDMS layer.	94

Figure 6-4 (a) The schematic of the stretchable sensor applied with tensile strain along the transverse direction or the longitudinal direction. (b) The curve of average relative change in resistance against the applied tensile strain in transverse and longitudinal direction for the serpentine stretchable sensor as well as the curve for the rectangular stretchable sensor..... 97

Figure 6-5 (a) The schematic of the FEM model applied with transverse or longitudinal strain. (b) Illustration of the part of serpentine shapes stretched along the transverse direction for analytical calculation. (c) Contour plot of the transverse strain in the MWCNTs/PDMS composite. (d) Contour plot of the longitudinal strain in the MWCNTs/PDMS composite..... 98

Figure 6-6 (a) The average relative variation in resistance for the sensor based on rectangular MWCNTs/PDMS composite applied with tension deformation as well as its polynomial fitted curve. (b) The average relative variation in resistance for the sensor based on serpentine MWCNTs/PDMS composite applied with transverse tension deformation as well as its linear fitted curve 101

Figure 6-7 The relative change in Resistance of the serpentine sensor subjected to the cycle of stretching/releasing with 0%-10% strain variation (a) and 0%-20% strain variation (b). 103

Figure 6-8 (a) The relationships between relative change in resistance and the applied strain when serpentine sensor experiences transverse stretching and releasing with 10% and 20% strain respectively and (b) the dependences between relative variation in resistance and the applied strain when the rectangular one undergoes transverse stretching/releasing cycle with 10% and 20% strain respectively 104

Figure 8-1 The resistance change of the CNTs composite model and the variation of the contacted CNTs percentage when the model is stretched with different polymer matrix Poisson's Ratio (a) 0.25, (b) 0.3 and (c) 0.35..... 152

List of Tables

Table 2-1 Comparison of different dispersion approaches for CNTs in polymer composites....	17
Table 2-2 Advantages and disadvantages of interaction techniques with covalent and noncovalent	22
Table 2-3 Summary of performance results of stretchable strain sensors reported in recent literature.....	34
Table 4-1 The resistance of four samples in each type of MWCNTs/PDMS composite with different mass fraction of MWCNTs (5% and 7%) as well as the average value of every four samples.....	64
Table 5-1 The amounts of MWCNTs, liquid PDMS, curing agent and solvent PDMS used in the experiment.....	73
Table 5-2 The electrical resistance of four samples in each type of MWCNTs/PDMS membranes with different concentrations of MWCNTs (5%, 7%, and 9%) as well as the average values and standard deviation of every four samples.	74
Table 6-1 The initial measured resistance of three serpentine sensors based on the MWCNTs/PDMS composite with 7% MWCNTs as well as the average value of the three sensors.	95
Table 6-2 The experimental data of the MWCNTs/PDMS composite and PDMS for the FEM simulation.....	97

Abstract

With the advancement of the living standard worldwide, an increasing number of people pay more attention to their health. Consequently, the industry of wearable devices for health monitoring has been experiencing rapid development. Stretchable sensors are the core components for wearable devices. However, further research is still needed to improve performance and reduce cost. In addition, stretchable sensors are currently always employed in other emerging industries, such as robotics, smart textiles, electronic skins and so forth. These fields not only require the sensors to possess excellent sensing performance but also need multi-functionality for practical applications.

In this study, two types of stretchable sensors based on MWCNTs/PDMS composite were fabricated and characterized. At first, the mechanism of the conductivity of the CNTs-based composite was theoretically investigated through numerical simulation. The shape of CNTs has a significant influence on the percolation threshold for conductivity, but the electrical conductivity of CNTs merely influences the electrical conductivity of the composite. With regards to the piezoresistivity of the composite, not only does the property of CNTs play an essential role, but also the Poisson's ratio of the polymer matrix. This work gives some suggestion to select elastic polymer and CNTs. The suitable polymer needs to have lower Poisson's ratio and CNT should have large aspect ratio. In addition, the volume fraction of CNTs embedded in the polymer is suggested to be slightly more than the percolation threshold. Following these, the composite sensor can acquire better performance.

Then, the core material for the stretchable sensor, the MWCNTs/PDMS composite, was made. The common issue in the fabrication process is the agglomeration of MWCNTs in

the matrix. This was resolved by using pentane as a solvent. It is attributed to the low boiling point of the pentane, which significantly shortens the evaporation period in the fabrication process.

Thirdly, the sandwich-like sensor based on MWCNTs/PDMS composite was fabricated. Due to the encapsulation of PDMS, the stretchable sensor can be biocompatible and mechanically compliant with human bodies. Although the stretchable sensor performed not very well in the aspect of hysteresis, they exhibited excellent sensitivity, response time and durability. Moreover, the stretchable sensor successfully detects simple human motions, like wrist and finger bending.

Finally, a stretchable strain sensor based on MWCNTs/PDMS composite with serpentine shape was devised and fabricated. Not only can this sensor distinguish tension strain from transverse and longitudinal direction, but also exhibit good linearity of response to tensile strain. In terms of sensitivity, hysteresis and response time, the stretchable strain sensor showed good performance.

Even though this research successfully fabricated the MWCNTs/PDMS composite and corresponding stretchable sensors with good performance, the excellent multifunction of sensors still need to be developed in future work.

Abbreviations

1D	One-dimensional
3D	Three-dimensional
ABS	Acrylonitrile butadiene styrene
AgNW	Silver Nanowire
AR	Aspect ratio
BICG	Biconjugate gradients
CNT	Carbon Nanotube
CNTs	Carbon Nanotubes
CVF	Carbon nanotube volume fraction
DTAB	Dodecyltri-methyl ammoniumbromide
FEM	Finite element models
FESEM	Field emission scanning electronic microscope
GF	Gauge Factor
IPA	Isopropanol alcohol
MLE	Maximum likelihood estimator
MWCNTs	Multi-wall Carbon Nanotubes
PDMS	Polydimethylsiloxane
PEDOT:PSS	Poly(3,4-ethylenedioxythiophene) polystyrene sulfonate
PR	Poisson's Ratio
PTR	Percolation threshold range
PU	Polyurethane
SDS	Sodium dodecylsulfate
SEM	Scanning Electron Microscope

SWCNTs	Single-wall Carbon Nanotubes
TPU	Thermoplastic polyurethane
-COOH	Carboxylic acid
-OH	Hydroxyl

Symbols

A	Cross-sectional area of the tunnel
C_{ij}	Conductivity of the effective conductive segment of a CNT
C_m	Electrical conductivity of the model
C_v	Dimension coefficient
D	Diameter of a CNT
d	Minimal distance between two the centerlines of CNTs
d_l	Length of the linear part in the serpentine shape
e	Charge quantum
f	CNT volume fraction
f_a	Proportion of the arc parts to the total actual length
f_c	Percolation threshold
f_l	Proportion of the linear parts to the total actual length
h	Minimal distance between the surfaces of two CNTs
J	Tunneling current density
L_w	Total actual length of the serpentine structure
L_x	Depolarization factor
l	Length of a CNT
l_0	Mean length of CNTs
l_a	Arc length of the arc part in the serpentine shape
l_a'	Arc length of the arc part in the stretched serpentine shape
l_m	Side length of the cube model
m	Mass of an electron
N_i	Total number of nodes near the node i

θ_i	Maximum polar angle of a CNT
P	Planck's constant
R_{ij}	Resistance of the effective conductive segment of a CNT
R_m	Macroscopic electrical resistance of the model
R_t	Tunneling resistance
r	Radius of the arc part in the serpentine shape
r'	Radius of the arc part in the stretched serpentine shape
$rand$	Random value ranging from 0 to 1
s_w	Width strain of the serpentine structure after stretching
V	Electrical potential difference
V_i, V_j	Electrical potentials of points i and j
w	Width of the serpentine shape
x, y, z	Coordinate of the center point of a CNT
x', y', z'	Coordinate of the center point of a CNT after stretching
x_e, y_e, z_e	Coordinates of two endpoints of a CNT
Y	Maximum full scale $\Delta R/R_0$ in the stretching and releasing cycle
γ_H	Hysteresis error index
ε	Strain of the composite model
θ	Polar angle
θ'	Updated polar angle after stretching
θ_a	The angle of the stretched arc part in serpentine shape
λ	Barrier height of the polymer matrix
ν	Poisson's ratio of the composite model
σ	Electrical conductivity of composite

σ_{CNT}	Electrical conductivity of a CNT
φ	Azimuthal angle
φ'	Updated azimuthal angle after stretching
ΔH_{max}	Maximum difference between the $\Delta R/R_0$ in the stretching and releasing cycle
ΔL	Difference between the initial length of the serpentine structure and the stretched length
$\Delta L_1, \Delta L_2$	Stretched lengths induced by the serpentine structure
ΔR	Difference between the initial resistance of the model and the one after stretching
ΔR_r	Relative change in resistance of the serpentine structure

Chapter 1 Introduction

1.1 Background

In recent years, wearable sensors have drawn a great deal of attention due to the increasing focus on human health and the advancement of biomedical devices. Wearable sensors are mainly employed to detect human motions and health conditions, providing accurate and reliable information¹⁻⁵. For instance, some wearable sensors are designed to continuously monitor people's pulse and heartbeat so that people can have an overview of their human health conditions at any time without hospitalization⁶⁻⁸. Also, when people are engaged in sports activities, wearable sensors are possible for the improvement of their sports techniques by recording their motions precisely⁹⁻¹¹.

In particular, wearable sensors based on nanocomposite are most popular owing to their many peculiar advantages comparing with traditional sensors based on metals or semiconductors, including high stretchability of elastomer (stretchability means the elongation of the polymer without plastic deformation), ease of fabrication, light-weight and vice versa¹²⁻¹⁴. Nanocomposites sensors are utilised to monitor large strain variation, mainly through the change of percolation network in the polymer/conductive fillers composite. There are a variety of conductive fillers that are compatible with polymers producing a synergistic effect, including carbon nanotubes (CNTs)¹⁵⁻¹⁸, graphene¹⁹⁻²¹, silver nanowires²² and so forth^{9, 23, 24}. Among them, it is proved by many studies that CNTs can endow polymer composite with excellent electrical properties, due to their rather high aspect ratio coupling with their exceptional electrical conductivity²⁵⁻²⁷. The percolating network structure built by CNTs will have a distinct transformation when the polymer nanocomposite filled with CNTs is subjected to the applied strain variation,

exhibiting more outstanding piezoresistivity compared with other fillers, due to their curvilinear shapes^{28, 29}. Also, when combining with a highly elastic polymer, CNTs can allow the polymer matrix to maintain their excellent stretchability as much as possible due to the entanglement of CNTs³⁰. However, CNTs are inclined to form agglomeration because of the presence of the high van der Waals force between adjacent CNTs³¹. Therefore, the preliminary task for preparation of desirable CNTs polymer nanocomposite is to make CNTs homogeneously dispersed in the polymer matrix.

With regards to the polymer matrix, Polydimethylsiloxane (PDMS) is viewed as the ideal candidate. This elastomer has a couple of distinctive characters, such as biocompatibility and mechanical stretchability, chemical stability and so on, making it suitable in the field of wearable device^{32, 33}. Furthermore, the cast moulding technique that is employed to fabricate nanocomposite with PDMS resin is simple and inexpensive³⁴. In this context, PDMS is the suitable choice to be used as the matrix of the nanocomposite filled with CNTs.

To date, many studies not only focus on the enhancement of nanocomposite electrical and mechanical properties for wearable sensors but also embark on designing unique and productive structures of sensors to allow them to possess many functions. Amjadi et al. reported the stretchable sensor based on the composite of silver nanowires (AgNW) and PDMS showed strong piezoresistivity with gauge factor between 2 and 14, and high stretchability up to 70%²². Nevertheless, the sensor had poor response time and exhibited non-linearity. Additionally, Zhu and his co-worker developed highly stretchable multifunctional sensors consisting of two electrodes made of silver nanowires and a dielectric layer of Ecoflex, through the capacitive sensing mechanism³⁵. It not only could differentiate the tension and pressure but also exhibited fantastic properties that can detect

strain (up to 50%), pressure (up to ~1.2 MPa), fast response time (~40 ms) and good pressure mapping function. Nevertheless, the gauge factor which is a critical sensing index was just around 0.7. In addition, to overcome the limitation of the conventional single axis-strain sensor, many studies have been conducted to develop multi-dimensional strain sensors. Kim et al. reported a multi-dimensional strain sensor consisting of two layers of the prestrained AgNW network with decoupled and polarised electrical response in axial and longitude directional strain³⁶. Moreover, it could successfully withstand up to 35% maximum strain with a large gauge factor (>20). It is worth mentioning that this stretchable sensor was unable to withstand a repeated cycle of tension for a long time as a result of the intrinsic prestrained silver NW network. To this end, despite the significant development of various stretchable sensors at present, there are still some considerable drawbacks.

1.2 Research Motivation and Objectives

According to the current development of stretchable sensor, this research aims to develop a kind of multifunctional sensor that is capable of detecting tension from two directions (longitudinal and transverse directions). There are three purposes for completing this research.

First of all, as mentioned earlier, manufacture of CNTs/PDMS nanocomposite with good quality is the primary issue at present. According to the previous studies in the literature, there are two approaches to improve it. On the one hand, the purpose is to get a thorough understanding of what material parameters would produce a significant effect on the electrical properties of nanocomposite embedded with CNTs. In this regard, the three-dimensional (3D) resistor network model based on composite filled with CNTs should be built and investigated computationally in depths. If the principle of the piezoresistivity of

the nanocomposite as well as the relevant influencing factors are understood, it will be helpful to the fabrication of high-class CNTs/PDMS nanocomposite. On the other hand, considering the intractable issue that it is difficult to disperse CNTs uniformly and break up the CNTs clusters, how to make CNTs evenly disperse in the PDMS matrix, with little deterioration to their mechanical and electrical properties is the preliminary task.

Second, after preparation of nanocomposite based on CNTs/PDMS, the sensor based on this nanocomposite should be developed. With the aim of the application on human bodies, the nanocomposite was sandwiched by two PDMS layers to form a biocompatible sensor. Following this, the integrated sensor was characterised to investigate the piezoresistive performance, including response time, sensitivity, stretchability, durability, and hysteresis. If the sandwiched-like sensor was capable of monitoring the strain variation excellently, it would provide evidence that the nanocomposite of CNTs/PDMS could be eligible to be a candidate of sensing material for further development.

Finally, the stretchable sensor that can monitor strain in longitudinal and transverse direction was designed and manufactured. Based on the as-prepared nanocomposite of CNTs/PDMS, the serpentine shape was introduced to distinguish tension in longitudinal and transverse direction. After that, the multifunction sensor should be characterised to verify whether it is qualified to monitor the strain change and tension direction. In parallel, it will be verified whether the serpentine shape will bring a positive effect on the sensing performance compared with other conventional sandwich-like sensors.

To conclude, the objectives of this research can be listed as follows

- To develop a dynamic model of a 3D resistor network to evaluate the parameters which will affect the electrical conductivity and piezoresistivity of the

nanocomposite. These parameters include the electrical conductivity of CNTs, the alignment of CNTs, the Poisson Ratio of the polymer matrix, the concentration of CNTs. This model not only can provide the theoretical support for the practical experiment, but also is helpful to have a better understanding of the conductivity and piezoresistivity of composites.

- An improved fabrication method of the CNTs/PDMS composite should be proposed, which can ensure that the CNTs are homogeneously dispersed in the PDMS resin.
- To fabricate the stretchable sensor composed of rectangular CNTs/PDMS nanocomposite, achieving excellent piezoresistivity, in the aspect of sensitivity, response speed, hysteresis, durability and so forth.
- On the basis of the stretchable sensor made of rectangular CNTs/PDMS composite, a novel stretchable sensor with serpentine CNTs/PDMS composite will be designed and made. Compared to the sensor made of rectangular composite, not only the sensing performance can be improved, but also some specific functions would be imparted to the new sensor, like the capability of detection the tension from both transverse and longitudinal directions.

1.3 Thesis Overview

We have introduced the background of this research and explained the motivations and objectives in this chapter. The remaining chapters are organised in the following orders: Chapter 2 is devoted to a literature review. It concentrates on the fundamental principle of the electrical properties of nanocomposite filled with particles and fabrication approaches of nanocomposite embedded with CNTs. In addition, a variety of stretchable sensors referred from previous studies are described in the categories of mechanism,

performance, and applications. In chapter 3, a model of 3D resistor network based on nanocomposite filled with CNTs is proposed. The factors influencing electrical properties of nanocomposite are discussed through computational simulations. Chapter 4 illustrates the experimental procedure of preparing CNTs/PDMS composite and proposes a useful method to improve the dispersion state of CNTs in the PDMS matrix. Chapter 5 describes the fabrication approach of the rectangular stretchable sensor comprised of PDMS and the CNTs/PDMS nanocomposite. Besides, its piezoresistivity performance is characterized. In Chapter 6, a stretchable sensor with serpentine CNTs/PDMS composite are made. This sensor not only possesses better sensing performance compared to the sensor with rectangular composite, but also has the potential to distinguish tension in transverse and longitudinal direction. Finally, Chapter 7 summarizes the outcomes of this research and outlines the future work.

Chapter 2 Literature Review

2.1 Introduction

As mentioned in Chapter 1, a great deal of attention has been paid to the wearable electronic devices for human activity and real-time health monitoring due to the increasing emphasis on human health. At present, wearable sensors are usually put into the applications of health-monitoring, soft robotics, and human detection. As the traditional strain sensors (metal and semiconductor strain gauges) regularly exhibit low stretchability, they are mainly used in engineering fields for damage detection and characterisation. Hence, researching and developing skin-mountable and wearable sensors, which can be mounted on the skin or embedded in clothes with little discomfort, has become a more popular trend, compared to the traditional sensors. The requirements for the stretchable sensors included high stretchability, durability, low power consumption, portability and so forth³⁷⁻⁴⁰. Elastic polymer composites based on conductive nanoparticles were proposed as the sensing element material for the wearable sensors^{22, 41}. This is because some elastic polymers can be adopted as the support matrix owing to the high stretchability and biocompatibility. In parallel, nanoparticles can construct the electrically conductive network inside the polymers, thanks to their outstanding mechanical and electrical properties as well as compatibility with polymers. As mentioned earlier, Carbon nanotubes (CNTs) is one of the ideal candidates for nanocomposite fillers due to its well-known excellent mechanical and electrical properties^{11, 42-46}.

Therefore, this chapter firstly makes a review of CNTs in terms of its structures and properties. Then, the electrical conductivity and piezoresistivity of the nanocomposite

embedded with CNTs are described, while its principle of conductivity and corresponding theory investigation are also explained and reviewed. Finally, the current studies concerning highly stretchable sensors made of nanoparticle-embedded composites are presented in detail. They will be described in the aspects of the fabrication method, the sensing mechanism, the practical performance in characterisation and so forth. A comprehensive literature review will give us useful information in designing the following studies.

2.2 Carbon Nanotubes

2.2.1 Structure of Carbon nanotubes

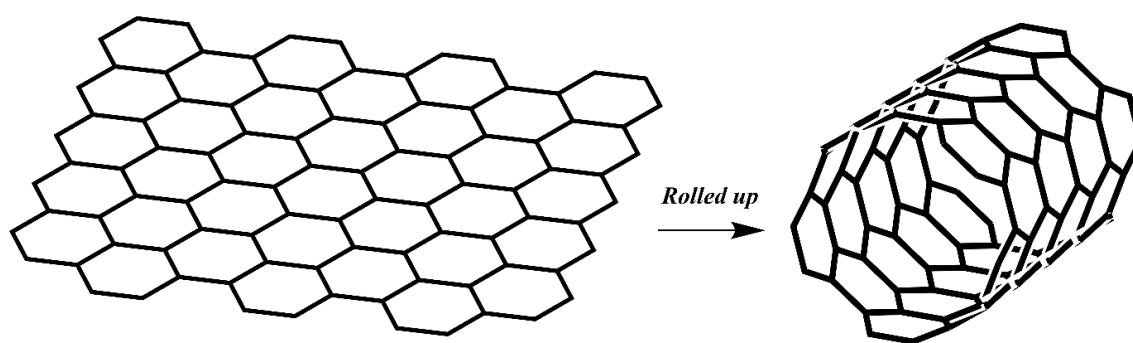


Figure 2-1 Schematic diagram showing a CNT is rolled up from a graphene sheet.

Carbon nanotube (CNT) has a unique structure, which results in superior properties, such as mechanical property, electrical property and thermal conductivity. The CNT has a large aspect ratio owing to its one-dimensional (1D) size and curvilinear shape. A CNT can be viewed as a seamless cylinder which is seemingly generated by rolling graphene layers along a defined angle as depicted in Figure 2-1. The cylindrical nanotube generally has at least one end capped with a hemisphere of fullerene structure.

In light of different rolling angles of the graphene layers, there are three kinds of chiralities: armchair, zigzag and chiral as depicted in Figure 2-2. The chirality can be

described by a chiral vector $C = na_1 + ma_2$. n and m denote the chiral indices, while a_1 and a_2 are the graphene lattice vectors^{47, 48}. When n is equal to m , CNT is defined as armchair. If m is zero, CNT is called zigzag. Elsewise, they are named as chiral.

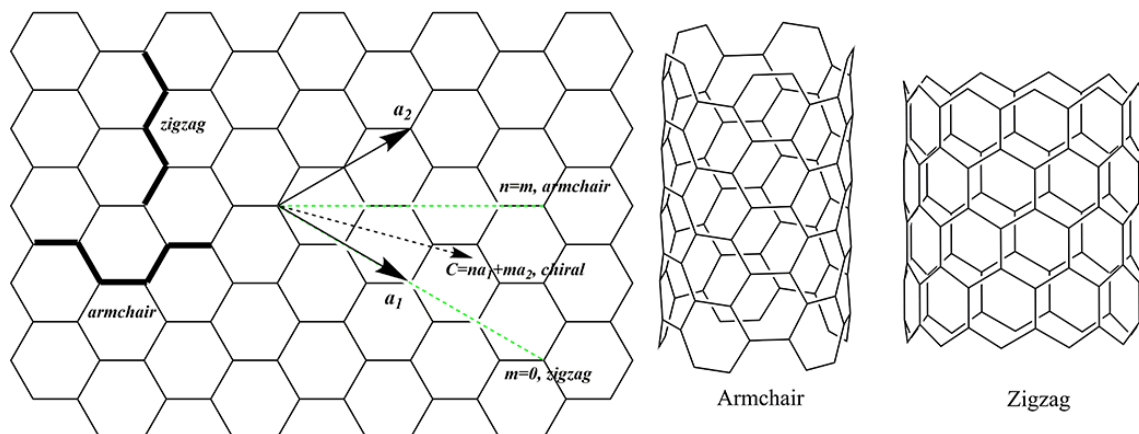


Figure 2-2 Schematic diagram showing how a hexagonal sheet of graphene is rolled to form a CNT with different chiralities.

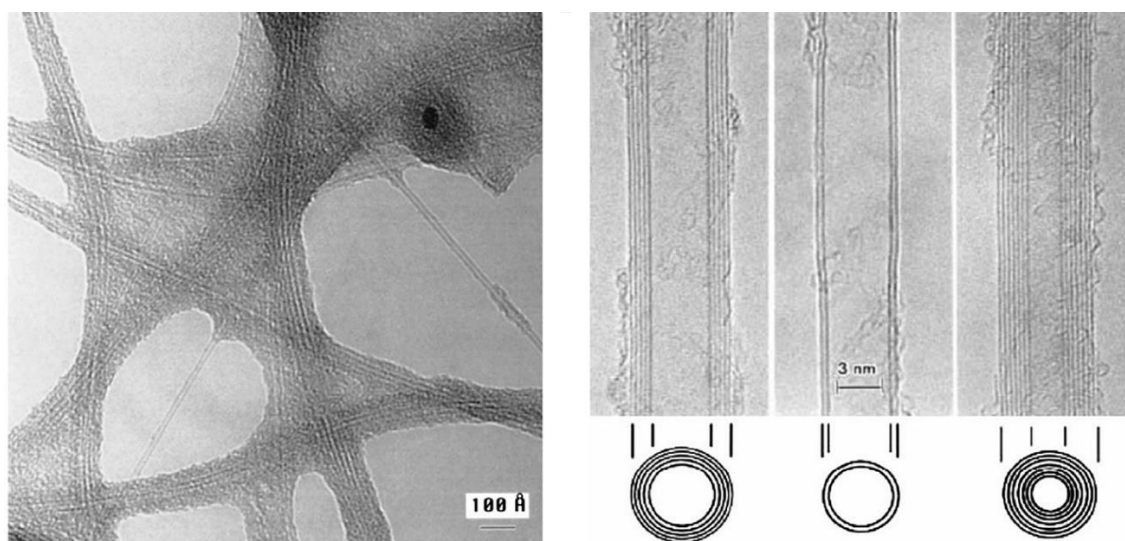


Figure 2-3 TEM images of different CNTs (A: SWCNTs; B: MWCNTs with different layers of 5, 2 and 7)⁴⁹.

According to the number of the rolled graphene layer, there are two types of CNTs, single-walled carbon nanotubes (SWCNTs) which are composed of a single rolled graphene sheet, and multi-walled carbon nanotubes (MWCNTs) which are formed by rolling up two or more graphene sheets as depicted in Figure 2-3. The diameter of SWCNTs typically ranges from 0.8 to 2 nm, while MWCNTs varies from 5 to 180 nm. CNT lengths

vary from less than 100 nm to several centimetres, thereby bridging molecular and macroscopic scales²⁵. Notably, with regards to the MWCNTs, the rolled graphene sheets are coaxially arranged around a central hollow core by van der Waals force between neighbouring layers. In addition, owing to the presence of the van der Waals force between the consecutive cylinders, the interlayer spacing of MWCNTs is approximately 0.34 nm, which is slightly bigger than graphite (0.335nm)⁵⁰.

2.2.2 Properties of Carbon nanotubes

CNTs have attracted much attention since their first discovery by Iijima in 1991 due to their extraordinary mechanical and electrical properties⁵¹.

Mechanical Properties. It is well-known that CNTs has excellent mechanical properties. This is ascribed to the σ bonds and the tubular structure of CNTs. Based on a couple of analytical calculations, Young's modulus of SWCNTs is estimated to be least 1 TPa⁵². Demczyk et al. measured the mechanical parameters for MWCNTs, achieving a mean value of 0.9 TPa for Young's Modulus and a tensile strength of 1.5TP⁵³. This can be explained by the fact that extra energy absorption is required for the hollow structures of CNTs in contrast to other materials.

Owing to these superior mechanical properties, CNTs becomes one of the most suitable options as reinforcing fillers materials for composites synthesis⁵⁴. For instance, Jyoti et al. embedded MWCNTs into acrylonitrile butadiene styrene (ABS) using a micro twin screw extruder with backflow channel. The mechanical property of the pure ABS was remarkably improved. Compared to the tensile strength of pure ABS, when ABS composite incorporated 3 wt. % MWCNTs, a significant enhancement (up to 69.4 MPa) was produced, which was equivalent to 29% increase over pure ABS⁵⁵.

Electrical Properties. With the help of their conjugated and highly anisotropic 1D structures, CNT is the fascinating type of electronic material from both theoretical and practical standpoints^{56,57}. The electrical conductivity has been measured to be high as 10^6 S/m for SWCNTs and 3×10^5 S/m for MWCNTs, respectively, suggesting that CNTs perhaps may be a more suitable choice as a conductor instead of metals^{58,59}. However, in most cases, the conductivities of CNTs are not able to reach the ideal values because of the unavoidable defects or impurities formed in the course of CNTs production⁶⁰.

The electrical conductivity of CNT in part depends on its chirality. If the chirality of CNT is armchair, that is $n = m$ with no band gap as illustrated in section 2.2.1; the CNT is metallic. When n is not equal to m with some band gap, CNT exhibits semi-conductivity. Worth of mentioning is that when the $n-m = 3q$ where q is an integer, a small band gap will be induced by the curvature of the graphene sheet. In this case, CNT is called semimetallic, quasi-metallic, or small-gap semiconducting. The band gaps of both semiconducting and small-gap semi-conducting SWCNTs decrease by $1/r_t$ and $1/r_t^2$, respectively. The small-gap semiconducting CNT, which is formed by means of curvature effects, is often viewed as metallic at room temperature for experimental condition^{47, 56}. The outstanding electrical properties of carbon nanotubes make them useful in electronic devices and sensor applications. CNTs are usually employed to make composites by combining with polymers. Based on the different contents of CNTs, the composite will exhibit different electrical conductivities. This will be elaborately reviewed in section 2.3.2.

2.3 Composite based on Carbon Nanotubes

2.3.1 Dispersion of CNTs

A load of studies have been devoted to fabricating excellent CNTs/polymer composites for functional applications. Although a great stride has been made after a decade of research, the maximum potential of adopting CNTs as reinforcements in composites still cannot be fully realised due to the difficult problem of many CNTs agglomerations and weak interfacial interaction between polymer matrix and CNTs. It is more difficult to disperse CNTs compared with other conventional fillers, such as carbon black and graphene. This is attributed to the particular shape of CNTs, which possesses small diameter in nanometer scale coupling with large length, thus producing high aspect ratio and enormous surface energy. Tremendous van der Waals force, which plays a significant role in the formation of MWCNTs, exists between adjacent CNTs. In addition to the inherent defects of CNTs, the as-produced CNTs purchased in the market are usually in the form of severely entangled bundles, which leads to the difficulty in preparing good composites.

Also, the presence of agglomeration and bundles in CNTs are detrimental to the mechanical and electrical properties of composites in contrast to the theoretical enhancement of composite embedded with CNTs homogeneously dispersed. With the aim of fabrication of CNTs/polymer composite with improved performance, the challenge is how to evenly incorporate CNTs into a polymer matrix or avoid forming CNTs clusters. There are a couple of traditional methods to separate individual CNTs from CNTs cluster and bundles as well as maintain the dispersion state of CNTs in the polymer matrix to avoid re-agglomeration. They will be introduced in the following sections.

2.3.1.1 Ultrasonication Method

As for the solution incorporating nanoparticles, ultrasonication is the most frequently employed route to disperse nanoparticles in the laboratory. There are two types: ultrasonic bath and ultrasonic probe horn also called a probe sonicator. The principle of these two ultrasonication techniques are same, which is that ultrasound shock waves propagate in the solution and agitate the nanoparticles clusters, resulting in a separation of individualised nanoparticle from clusters and promoting nanoparticles to be dispersed evenly^{61, 62}. Besides, due to the presence of the powerful van der Waals force between neighbouring CNTs, the sonicator, which can produce more ultrasound energy compared to the sonicate bath, has a distinct advantage.

It is worth noting that ultrasonicator is usually utilised for solution or mixture with a low viscosity. Hence, as to the majority of polymers which are either viscous liquids or solids, they are required to be dissolved or diluted in a suitable solvent to mitigate the viscosity for better utilisation of ultrasonication⁴⁹. Also, with regards to the sonicator, it generates considerable heat rapidly in the course of sonication around the probe. As a consequence, if the CNTs are dispersed in volatile solvents, such as Pentane and isopropanol alcohol (IPA), the mixture solution is required to keep cold to avoid quick evaporation. Moreover, the sonication pulse interval should be short to avoid a quick rise of temperature.

Once the CNTs suspension is dispersion by sonication for a long time or with a strong power, their structures would be readily and severely damaged, especially when a probe sonicator is used. If the sonication power is not very strong, some defects would still be generated on the surface of CNTs. In the extreme case, the graphene shells of CNTs would be completely destroyed and the whole CNTs are thus converted into amorphous carbon.

As a result, both the electrical and mechanical properties of CNTs/polymer composites deteriorate due to the damage of the CNTs.

2.3.1.2 Calendaring

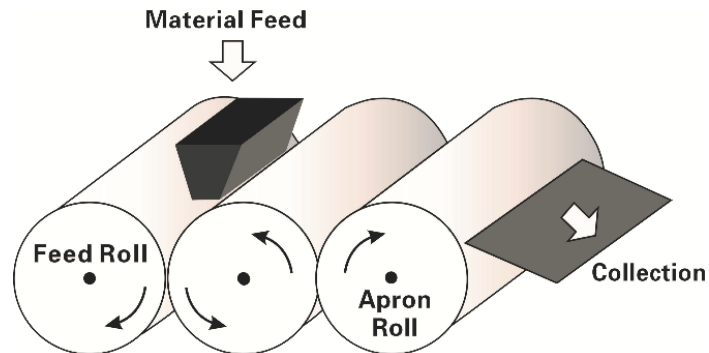


Figure 2-4 Schematic diagram showing the general configuration of a three-roll mill⁶³

The calendar, which is also named as three-roll mills, is a facility that is employed to mix and homogenise viscous materials via large shear force generated by its rollers. The typical configuration of one calendaring machine composed of three adjacent cylindrical rollers each of which rotates at a different rate^{63, 64}. As depicted in Figure 2-4, the first and third rollers are called the feeding and apron rollers respectively. They rotate in the same direction whereas the centre roller does on the contrary direction to them. A hopper is placed between the feeding and centre rollers, which is used for the addition of material. Notably, the narrow gaps between the rollers, associated with the mismatch in the angular velocity of the adjacent rollers, lead to locally high shear forces within short residence time.

Generally, calendaring is widely used to mix ceramic, printing inks, carbon and so forth. Although some researchers have employed this technique for dispersion of nanomaterial like CNTs and predicted it as a relatively promising method in future, there are still several concerns for CNTs dispersion that needs to be addressed. On the one hand, the minimum gap between the rollers is around 1-5 μm . In spite of the approximate length of

individual CNT to the gap, its diameter is much smaller than the width of the gap. Furthermore, the shape of CNT is not a straight tube but curvilinear, indicating that the actual length of CNT is less than the intrinsic length. Due to the dimensional disparities between the rollers gap and the CNT dimension, the rollers are only capable of separating the big CNTs clusters into small clusters at sub-micron level but has little impact on the relatively small entangled CNTs clusters. Hence, MWCNTs with relatively large size may be evenly dispersed using this machine. On the other hand, the feeding materials are required to be viscous so that they can be put into the machine together with CNTs. Thus, this machine is perhaps not suitable for the liquid polymer.

2.3.1.3 Ball Milling

Ball milling is always employed to grind materials into fine powders like paints, pyrotechnics and ceramics. This tool consists of a cylindrical container and rigid balls in the container. During the rotation of the mill, high pressure is produced by the collision between the tiny and rigid balls. Then the feeding material would be squeezed and fined by this pressure. Finally, after a couple of time, the material is converted into fine powders⁴⁹.

It was found that if the high energy ball-milling of CNTs were utilised in an inorganic material, CNTs would be more efficiently disentangled and more uniformly dispersed⁶⁵.⁶⁶. Liu et al. employed CNTs reinforced pure aluminum using a ball milling method. The yield strength of the composite was increased by 42.3% compared with the pure aluminum matrix⁶⁷. It is noteworthy that this process would be detrimental to the morphology and structure of CNTs due to the high pressure generated by balls⁶⁸.

2.3.1.4 Melt Stirring and Extrusion

Melting stirring and extrusion is a common technique to disperse particles in the solid material which is melt. This method has been widely used due to its simple procedures. Some studies have prepared the CNTs/polymer with excellent performance using this method⁶⁹. Firstly, CNTs mixed with polymer pellets are fed into the extruder hopper. Then the mixture is heated until the polymer converts into melting state. At the same time, the mixture is being stirred by the twin screws at a high rate that produces a high shear flow, resulting in uniform mixture and dispersion of CNTs in the melt polymer. Worthy of mention is that this technique is particularly helpful in preparing CNTs composite with a high content⁷⁰.

Bilotti and his group fabricated a thermoplastic polyurethane (TPU) incorporating MWCNTs via an extrusion method⁷¹. It is demonstrated CNTs were homogenous in the TPU and exhibited excellent electrical conductivity. Also, Esawi successfully embedded the CNTs into an aluminum matrix using the hot extrusion. Although the bonds between CNTs and the aluminum matrix were not superior enough, the enhancement of tensile strength was apparent (21% increase compared to pure aluminum)⁷².

In the end, the various dispersion techniques for CNTs are summarised in Table 2-1, which is helpful to select an appropriate dispersion technique to prepare CNTs/PDMS nanocomposites. When choosing a proper method for CNTs dispersion, several factors are needed to be taken into consideration, including types of the polymers matrix, the content of CNTs to be added and fabrication process. It is worth noting that the approaches to disperse CNTs in the polymer matrix are certainly not limited to those described above. Furthermore, a couple of recent studies managed to acquire better CNTs

dispersion state through combining these approaches above, like a hybrid of ultrasonication and ball milling⁷³, a combination of ultrasonication and extrusion⁷⁴.

Table 2-1 Comparison of different dispersion approaches for CNTs in polymer composites

Technique	Factors			
	<i>Damage to CNTs</i>	<i>Suitable polymer matrix</i>	<i>Governing factors</i>	<i>Availability</i>
<i>Ultrasonication</i>	Yes, up to the time and amplification	Soluble polymer, low viscous polymer	Power and time of sonication	Commonly employed in lab, easy operation
<i>Calendaring</i>	No	Viscous polymer	Rotation speed, the distance between neighbouring rolls	Complicated operation, hard to clean after use
<i>Ball Milling</i>	Yes	Powder (polymer or monomer)	Rotation speed, balls size, milling time	Easy operation
<i>Melting Extrusion</i>	no	Thermoplastics	Temperature, configuration and rotation speed of the screw	Large-scale production, hard to clean after use

2.3.2 The Interaction between CNTs and Polymers

As illustrated in section 2.3.1, the dispersion state of CNTs is mainly related to the interaction between different CNTs. Besides, the interaction between CNTs and polymer matrix also plays a critical role in the overall performance of the composite⁷⁵. In retrospect, a large number of CNTs composites fabricated could not achieve the expected properties⁷⁶⁻⁷⁸. The root reason for these unexpected performances may be ascribed to the poor interaction behaviour of the nanocomposite constituents^{75, 79}. Furthermore, due to the curvilinear shape of CNTs, there is a fundamental difference between the interaction

characteristics in conventional composites and nanocomposites based on CNTs. Therefore, in this section, the interaction improvement techniques are reviewed, including the non-covalent and covalent approaches, and corresponding improvements in nanocomposites properties are covered. Notably, the interaction improvement techniques not only enhance the interface bondings between CNTs and polymer matrix but also help CNTs to evenly disperse in the matrix.

2.3.2.1 Covalent Interaction

When polymer chains are chemically bonded to the CNTs for interfacial reinforcements, the linkage is called covalent interaction in CNTs/polymer nanocomposites. There are two typical methods to achieve covalent interaction, sidewall functionalization and defect functionalization. Also, the majority of functionalization techniques require CNTs to be pre-modified by the introduction of functional groups to their surfaces. Moreover, these functional groups should be compatible with polymer matrix^{80, 81}. Direct covalent sidewall functionalization is concerned with a change of hybridisation from sp^2 to sp^3 and a simultaneous loss of π -conjugation system on graphene layer. This process can be accomplished by reaction with some molecules of a high chemical reactivity⁴⁹. In recent years, many methods have been developed for sidewall functionalization, such as cycloaddition⁸², chlorination⁸³, fluorination⁸⁴ and so forth⁸⁵.

Compared with sidewall functionalization of CNTs, defect functionalization takes advantage of chemical transformation of defect positions on CNTs. Defect positions can be the open ends and holes in the sidewalls, pentagon or heptagon irregularities in the hexagon graphene framework. Defects can be created on the sidewalls as well as at the open ends of CNTs by an oxidative process with strong acids such as HNO_3 , H_2SO_4 or a mixture of them⁸⁶, or with strong oxidants such as $KMnO_4$ ⁸⁷, ozone⁸⁸, reactive plasma⁸⁹.

The defects on CNTs created by oxidants are stabilised by bonding with carboxylic acid (–COOH) or hydroxyl (–OH) groups. The chemically functionalized CNTs can produce strong interfacial bonds with many polymers, allowing CNT based nanocomposites to possess high mechanical and functional properties⁴⁹.

Although covalent functionalization of CNTs is conducive to interaction between CNTs and polymer matrix as well as among adjacent CNTs, some drawbacks along with the covalent functionalization are indispensable. On the one hand, with the aim of placing function groups on the CNTs, a large number of defects are inevitably generated on the CNTs sidewalls during the functionalization process. This resulted damage is not only detrimental to the mechanical properties of CNTs but also disrupted π electron system in CNTs. The disruption of π electron degrades transport properties of CNTs, which will lead to deterioration of the electrical and thermal conductivity of CNTs. On the other hand, in light of the employment of concentrated acid or strong oxidants, covalent functionalization is unfriendly to the environment.

2.3.2.2 Non-covalent Interaction

In contrast to covalent interaction, non-covalent functionalization has a remarkable advantage that it can reserve the conjugated system of the CNTs sidewalls so that the structural properties of CNTs are not degraded. The non-covalent functionalization is an alternative method for tuning the interfacial properties of nanotubes⁹⁰. The CNTs are functionalized non-covalently by aromatic compounds, surfactants, and polymers for the most part. No matter what these approaches are, the root principle is to remarkably improve the solubility of CNTs in the polymer matrix. There are several common routes, including polymer wrapping⁹¹, surfactants absorption⁹² and endohedral method⁹³.

Polymer wrapping is not only a feasible way to produce favorable interaction between CNTs and polymers but also helps to improve the dispersion of CNTs. This type of non-covalent functionalization of CNTs is achieved through van der Waals interactions and π - π stacking between the polymer chains containing aromatic rings and the surfaces of CNTs as shown in Figure 2-5⁹⁴. The reinforcement effect depends on the structure of the polymer, chemical composition of the polymer molecules and geometric parameters of the constituents in the nanocomposite⁹⁵.

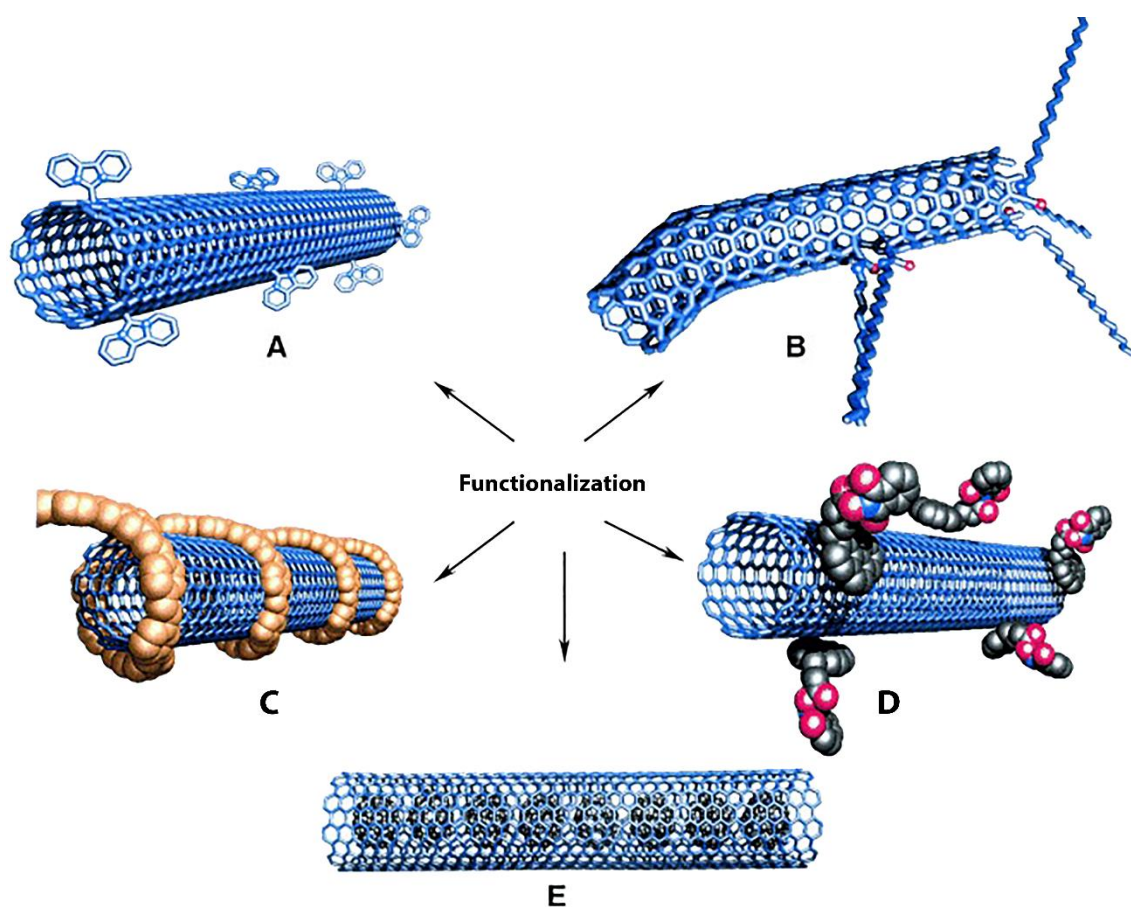


Figure 2-5 Functionalization possibilities for SWNTs: A) covalent sidewall functionalization, B) defect-group functionalization, C) noncovalent functionalization with polymers wrapping, D) noncovalent functionalization with surfactants, and, E) endohedral functionalization with guest atoms or molecules⁹⁶.

In addition, surfactant absorption is also employed to functionalize CNTs. The physical adsorption of surfactant on the CNTs surface lowers the surface tension of CNTs, which effectively prevents the aggregation of CNTs, as displayed in Figure 2-5D. Furthermore,

the surfactant treated CNTs overcame the van der Waals attraction by electrostatic/steric repulsive forces. The efficiency of this method strongly depends on the properties of surfactants, medium chemistry and polymer matrix⁹⁰. Generally, the surfactant can be categorised into three types: non-ionic surfactants, like Triton X-100⁹⁷; anionic surfactants, such as sodium dodecyl sulfate (SDS)⁹⁸; cationic surfactants, such as dodecyltri-methylammonium bromide (DTAB)⁹⁹. Based on previous studies, cationic surfactants have some advantages for water-soluble polymers, whereas CNTs dispersion was improved by a non-ionic surfactant in water-insoluble polymers¹⁰⁰. Unfortunately, although surfactants may be efficient in the solubilisation of CNTs, they are toxic for biological applications. Therefore, the use of surfactant-stabilised CNTs complexes is potentially limited to biomedical applications¹⁰¹.

The endohedral method is also commonly adopted for non-covalent CNTs functionalization. In this method, guest atoms or molecules are stored in the inner cavity of CNTs through the capillary effect. The insertion often takes place at defect sites localised at the ends or on the sidewalls. The inclusion of inorganic nanoparticles into the tubes, such as C₆₀, Au, Ag and Pt, is a typical example of endohedral functionalization¹⁰². The combination of these CNTs and guest molecules is particularly beneficial to integrate the properties of the two components in hybrid materials for applications in catalysis, energy storage, nanotechnology and molecular scale devices⁴⁹.

To summaries, the fundamental principle of covalent and noncovalent interaction techniques associated with corresponding strengths and shortcomings are listed in Table 2-2. Notably, despite visible improvement in the dispersion of CNTs brought from covalent interaction, the severe damage to CNTs structures is inevitable, perhaps leading to degradation of electrical conductivity^{103, 104}. With regards to noncovalent interaction,

thanks to the protection on the structure of CNTs, its intrinsic electrical property still maintains excellent after non-covalent functionalization. However, the functionalization groups attached to the sidewall of CNTs increase the contact resistance between CNTs. Thus, although the dispersion of CNTs is improved, whether the electrical conductivity of the composite is reinforced or not, depends on the experimental procedure and materials^{105, 106}.

Table 2-2 Advantages and disadvantages of interaction techniques with covalent and noncovalent

Techniques	Routes	Principle	Possible damage to CNTs	Interaction with polymer matrix
Covalent interaction	Sidewalls functionalization	Hybridization of C atoms from sp^2 to sp^3	Yes	Strong
	Defect functionalization	Defect transformation	Yes	Strong
Noncovalent interaction	Polymer wrapping	van der Waals force, π - π stacking	No	Variable
	Surfactant absorption	Physical absorption	No	Weak
	Endohedral method	Capillary effect	No	Weak

2.3.3 Fabrication of CNTs/polymer composite

2.3.3.1 Solution Mixing

Solution mixing is the most common method for the fabrication of CNTs/polymer nanocomposites because it is amenable to small sample sizes¹⁰⁷. Typically, solution blending involves several major steps: dispersion of CNTs in a suitable solvent by mechanical mixing, magnetic agitation or ultrasonication. Notably, as mentioned in section 2.3.1, ultrasonication is the best choice, because only ultrasonication is capable of breaking the CNTs cluster. Simultaneously, the solvent can also dissolve polymer

resins. Subsequently, the dispersed CNTs suspension is mixed with polymer matrix at room or elevated temperatures. The nanocomposite is finally acquired by precipitating or casting the mixture.¹⁰⁸ This method is usually adopted to prepare composite films. One should note that if evaporating the solvent at high temperature for a long while, the CNTs tend to re-agglomerate. Therefore, the experimental consideration is not limited to the compatibility of the solvent with CNTs, but also the boiling point is also vital to avoid re-agglomeration.

2.3.3.2 Melt Blending

Another common approach to fabricate CNTs/polymer composite is melt blending. This method is mainly appropriate for thermoplastic polymers, such as polypropylene¹⁰⁹ and polystyrene¹¹⁰. One of the main advantages of this method is that no solvent is needed to disperse CNTs. In other words, no step is required to evaporate solvent¹¹¹. Accordingly, it diminishes the chance for CNTs to agglomerate again. Specialized equipment is required like extruder, which is introduced in section 2.3.1.4, to generate a high shear force to disperse CNTs at a high temperature. Melt blending is frequently used to produce CNTs/polymer composite on a large scale. However, this technique is generally considered less effective to disperse CNTs in polymers¹¹².

2.3.3.3 In Situ Polymerisation

In situ polymerisation is always employed to fabricate CNTs composite with a thermosetting polymer as a matrix. It is efficient to realise uniform dispersion of CNTs in the polymer. This method is similar to the solution mixing¹¹³. In this method, CNTs are mixed with monomers, either in the presence or absence of a solvent. In addition, these monomers are polymerised via addition or condensation reactions with a hardener

or curing agent. One of the major advantages of this method is that covalent bonding can be formed between the CNTs and polymer matrix, resulting in much improved mechanical properties of composites through strong interfacial bonds¹¹⁴. PDMS-based nanocomposite fabricated with in situ polymerisation methods is popular in recent studies with applications in stretchable electronics^{115, 116}.

2.3.3.4 Other Methods

Besides these common techniques to fabricate CNTs/polymer nanocomposite, there are some new methods developed in recent years, including latex technology¹¹⁷, spinning of coagulant¹⁰⁹, layer-by-layer deposition¹⁷ and pulverization¹¹⁸. It is worth noting that as nanocomposite materials are an emerging field, many studies are being conducted to devise new processing methods that can produce nanocomposites with unique structures and properties for specialty end applications⁴⁹.

2.3.4 Electrical Properties of Carbon Nanotubes-based Composite

As is well-known, owing to the superior electrical property of CNTs, polymer/CNTs composites have great potential for electronic applications, like wearable devices, photovoltaic cells, electronic skins, etc^{15, 119, 120}. In this section, the electrical property of CNTs/polymer composite are reviewed, including its principle of electrical conductivity as well as the influence factors.

Generally, when filling some conductivity particles into insulating polymers, the percolation network in the polymer matrix will be established by fillers so that the insulating polymer is converted to electrically conductive polymer composite. Thanks to the curvilinear shape of CNTs, it helps CNTs to readily build a percolating network in the polymer matrix. In this context, along with the content of CNTs increasing, the variation

of the electrical conductivity of the composite can be divided into three stages¹²¹. As displayed in Figure 2-6a, initially, when the content of CNTs is very little, there is few contacting CNTs in the polymer. Obviously, it is impossible for CNTs to build a whole conductive path so that the electrical conductivity remains close to that of the neat polymer. Adding more CNTs, a couple of complete conductive paths may appear in the polymer matrix, leading to the remarkable improvement of the electrical conductivity as shown in Figure 2-6b. In this second stage, the electrical conductivity rises following a percolation power law so that the content of CNTs in this stage is called percolation threshold^{122, 123}. Subsequently, more CNTs added to produce more complete conductive paths in the polymer as shown in Figure 2-6c. At this stage, the electrical conductivity will go up gradually with the addition of CNTs. It should be noted that due to the presence of van der Waals force between adjacent CNTs, CNTs tend to entangle with each other, forming agglomeration, as shown in Figure 2-6d.

Furthermore, the electrical conductivity of the CNTs/polymer composite is determined by three factors: the network structure of CNTs, the intrinsic electrical conductivity of CNTs and the contact resistance of CNTs. The one factor influencing the network structure of CNTs is the distribution and dispersion state of CNTs in the polymer matrix. Generally speaking, the composite with uniform dispersion of CNTs possesses more excellent electrical conductivity than that with ordinary or poor dispersion state of CNTs. In parallel, uniform dispersion of CNTs helps the composite with a low concentration of CNTs to exhibit better electrical conductivity. On the other hand, the shape of CNTs also has an impact on network structure, like the diameter of CNTs, length, collinearity and so forth.

Besides, the electrical conductivity of the CNTs-based composites also partially relies on the intrinsic electrical conductivity of CNTs. As described in the section 2.2.1, the chirality of CNTs determines whether the CNTs is conductor or semiconductor⁴⁸. Also, it is common that defects of CNTs will be generated during the period of

dispersing CNTs in the polymer. Additionally, as introduced in section 2.3.2, functionalization of CNTs causes an apparent decrease in their electrical conductivity due to the damage on the structure of CNTs or the barrier established by surfactants between CNTs.

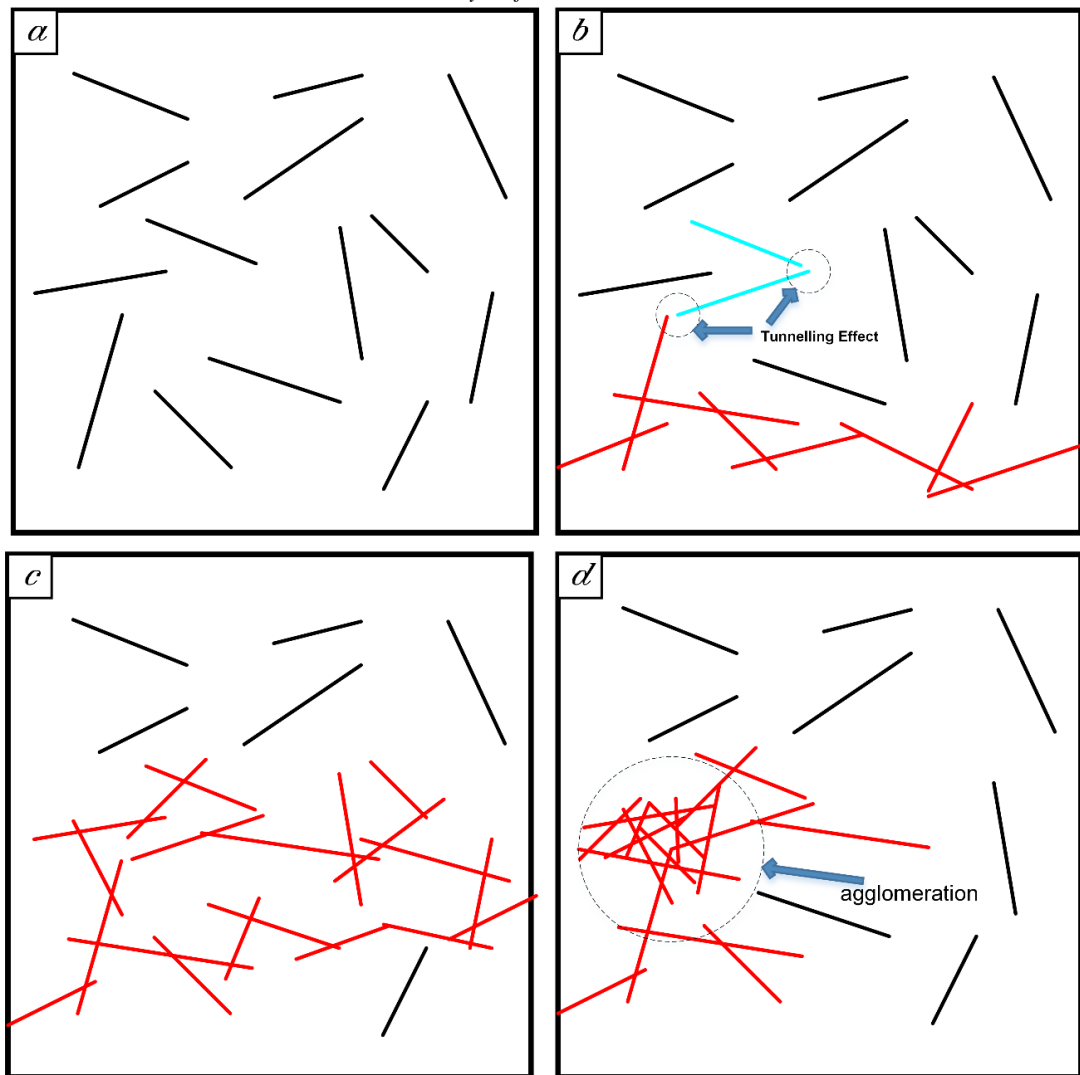


Figure 2-6 The formation process of percolation paths in conductive composites based on CNTs/polymer

The contact resistance of CNTs is another factor influencing the overall electrical conductivity of the CNTs/polymer composite. The contacting CNTs do not have authentic touch with each other. Due to the van der Waals force, once the adjacent CNTs mutually approach too tightly, the van der Waals attraction force will convert into repellent force, making the CNTs separated with the so-called van der Waals distance. It is further found that CNTs sidewalls would be deformed due to the function of van der Waals force as shown in Figure 2-7^{124, 125}. Also, the bonding between the fillers and polymer matrix is not ideally perfect. The weak interface can also diminish the contact resistance¹²⁶. Despite

the degradation of electrical conductivity by interfacial effect, electron hopping from one CNT to another contributes to the improvement of the electron conductivity. This phenomenon that electrons can directly pass through insulating polymer from one CNT to an adjacent one, is called with the quantum mechanical electron tunneling effect¹²⁷.

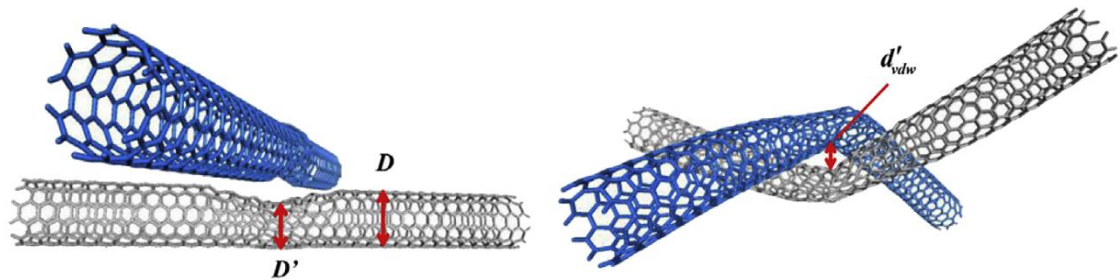


Figure 2-7 Schematic of deformable CNT model with mild deformation and severe deformation¹²⁸.

2.4 Stretchable Strain Sensor

2.4.1 Transduction Mechanism for Sensing

The principle of strain sensor is to convert external mechanical stimuli into electrical signals. The accuracy of monitoring thus depends on the efficiency and precision of transduction mechanism. In general, the stretchable sensor could be categorised to piezoresistive-type, capacitive-type and piezoelectric-type. Despite the existence of other types of sensors, including Raman shift, triboelectricity and Fiber Bragg Grating, there are limited studies on these, due to the demand for sophisticated measurement equipment and high investment. To the contrary, the primary three types of sensors need relatively simple read-out equipment and are promising to produce on a large scale. Thus, this review will focus on the introduction of the three primary types of sensors.

2.4.1.1 Piezoresistive-Type

Piezoresistive sensors usually transduce the strain into a variation of resistance so that they can be monitored by an electrical read-out system. There are two approaches to detect the resistance variation according to the strain variation. On the one hand, the resistance variation can be recorded based on the reconstruction of the conductive paths in the conductive composite. Typically, this type of piezoresistive sensors is made of high elastic polymer embedded with conductive fillers. There are common conductive fillers, like carbon nanotubes (CNTs)¹²⁹, carbon fibres¹¹⁷, graphene¹⁰, silver nanowire¹³⁰ and so on^{23, 131}. Among them, CNTs are extensively embedded into various polymers due to their superior mechanical and electrical properties^{77, 116}.

On the other hand, changes in the contacting resistance between conductive materials could be an indicator for the strain variation. Amjadi et al. fabricated a highly stretchable and sensitive sensor based on the AgNW network elastomer composite. Also, they made its gauge factor tunable ranging from 2 to 14, and kept stretchability up to 70%, both of which are considerably better than those of conventional sensors. Moreover, it was demonstrated that the gloves with strain sensors they made could be utilised to detect the fingers motion²². Later, Amjadi et al. presented a super-stretchable sensor based on CNTs/Ecoflex composite. Noticeably, it is found that the sensor could incredibly sustain a strain as large as 500%. Naturally, it can be mounted on any parts of the human body to monitor the human motion compliantly³⁷. Recently, Li and his co-workers, developed a strain sensor with high stretchability (up to 30%) and sensitivity (gauge factor beyond 47) using graphene foam and PDMS composite. Furthermore, it can be implemented to monitor the human motions with long-term stability¹³². In addition, Park et al. wrapped wool yarns with graphene and PDMS layer by layer. This sensor not only exhibited high

stretchability (up to 150%) and sensitivity but also could be woven in the clothes and gloves to detect various human motions compliantly, including finger or elbow bending, swallowing and breathing¹⁰. Yao et al. developed a pressure sensor based on the graphene-polyurethane sponge with fractured microstructure design. This structure endows high sensitivity of monitoring pressure to the device. Meanwhile, it was demonstrated it could still export repeatable and reproducible signals after a large number of cycles⁶.

Besides, some studies preferred to coat a conductive diaphragm on the stretchable polymer substrate¹³³. Wang et al. adhered a layer of graphene woven fabrics on the PDMS to form a stretchable sensor. The sensors possessed outstanding features, ultra-light, excellent sensitivity, superior physical robustness, facile fabrication method and compliance with human skin deformation¹³⁴. Yan fabricated graphene-nanocellulose nanopaper and attached it on the PDMS substrate. It improved the low stretchability (6% for nanopapers only) owing to the PDMS, and possessed a higher sensitivity compared with CNTs or AgNW film.

Different to the common type of sensors which is based on the variation of contacting resistance, Pang developed a flexible sensor which can detect different types of pressure, including shear, torsion and normal pressure. This device is composed of two interlocked arrays of Pt-coated polymeric nanofibers which are adhesive to the thin PDMS layer. When different mechanical stimuli were applied, the electrical resistance would be different due to the different contacting area of nanofibers⁴. Park and his co-workers also proposed a tactile-direction-sensitive sensor based on interlocked microstructures. The unique geometry of interlocked microdome enables the differentiation of various mechanical stimuli because the structure exhibited different levels of deformation

depending on the direction of applied forces¹³⁵. Hence, it also can be employed to detect the resistance induced by a lateral stretch, besides various types of pressuring detection.

2.4.1.2 Capacitive-Type

The capacitive-type sensor is composed of a pair of stretchable electrodes and a high elastic dielectric layer in the middle. Once external mechanical stimuli changes the distance between two electrodes, the capacitance would vary accordingly¹³⁶. The capacitance can be illustrated as follows: $C = \epsilon A/d$, where ϵ is the dielectric constant, and A and d are the area and distance between the two electrodes, respectively. These sensors possess higher stability and precision for detecting applied force, compared with piezoresistive-type sensors¹³⁷. Cohen et al. invented a capacitive strain sensor with a simple sandwich structure for detection of tensile deformation¹³⁸. A pair of electrodes were made of the SWCNTs-based composite, while PDMS was selected as the dielectric layer, due to the high Poisson's Ratio. Although this sensor could guarantee stability, linear response after thousands of stretches, the gauge factor was not optimal (0.99) compared with others. Cheng et al. developed a sensor with floating electrodes for tactile detecting. Once it was compressed, one electrode made of the gold layer coated on the PDMS would move closer to the permanent electrode, resulting in the rise of the capacitance⁷.

2.4.1.3 Piezoelectric-Type

Piezoelectricity means the generation of electrical charges in some materials with a non-centrally symmetric crystal structure under mechanical force. Thus the polarisation charges would be created, called dipole moments^{139, 140}. This phenomenon is widely used to transduce mechanical stresses into electrical signals via piezoelectric materials. In

parallel, to exploit the flexibility of the piezoelectric pressure sensors, some research groups have attempted several routes, including the construction of thin films of piezoelectric inorganics on flexible substrates¹⁴¹, and the use of piezoelectric polymers or inorganics/polymer composites¹⁴².

Wang et al. presented a pressure sensor array with oriented ZnO nanowires as the active component, which was highly sensitive to map the pressure distribution in the high spatial resolution¹⁴³. This is because when the ZnO nanowires are compressed, the strain inside the nanowire is much larger than that in the GaN film because of the low coverage of nanowires on the substrate surface, so a piezopotential is created in the nanowire. Besides, piezoelectricity materials are also employed in MOSFETs as the dielectric of the capacitor. Rogers et al., as one example, used lead zirconate titanate as the dielectric¹⁴⁴. When the transistor is pressed, the potential of the capacitance between electrodes subsequently increased, resulting in a growth of the current I_{DS} . Thereby, these devices have potential in accurate measurements of subtle effects of motion on the surface of the skin, ranging from blood pressure pulse waves in near-surface arteries to vibrations on the throat associated with speech.

2.4.2 Performance of Stretchable Strain Sensor

The feasibility of the commercial employment of sensors depends on its various performance, including the stretchability, sensitivity which is represented by gauge factor, linearity, hysteresis, durability, recovery time and so on. The following section will compare the performances of stretchable strain sensors in the literature.

2.4.2.1 Stretchability

Stretchability is an essential factor for wearable sensors. It does not mean the stretchable length to break, but the range where other performances still can maintain excellent actually. That is to say, in this stretchable range, the sensitivity can be guaranteed favourable and response to strain keeps linear. Meanwhile, it has acceptable durability, short recovery time and low hysteresis. The maximum stretchability of sensors to break is 1500%, which is reported by Fan¹⁴⁵. However, the effective stretchability falls to 400%, which can exhibit substantial repeatability and stability for monitoring strains yet. In parallel, Cai et al. presented a capacitive-type sensor based on CNTs/PDMS, which also possessed high stretchability (300%). It can maintain excellent linearity to strain, superior stability as well as durability, due to the capacitive principle. However, the sensitivity is relatively low ($GF=0.97$) compared with the piezoresistive-type sensors. Noticeably, no matter what type of the sensor is, the composite composed of an elastomer and 1D nanomaterial could exhibit higher stretchability. The sensors reported by Li et al. which was made of graphene foam and PDMS had a high sensitivity up to 98.66, though the stretchability was merely 30%, just meeting the requirement of wearable device¹³². Naturally, the 3D structure of graphene foam deteriorates the stretchability, while the sensitivity and linearity were improved. Compared to the 3D or two-dimensional nanomaterial, 1D nanomaterials have higher aspect ratios. Thus they are prone to form networks in the polymer so that their composites can sustain fairly strong mechanical deformation theoretically.

2.4.2.2 Sensitivity

Sensitivity is always represented by the slope of the relative variation of the electrical signals, like resistance and capacitance, against the applied strain. Gauge Factor (GF) is

employed to express the sensitivity, described by $GF = \frac{\Delta R}{R_0} / \epsilon$, for piezoresistive-type, or $GF = \frac{\Delta C}{C_0} / \epsilon$ for capacitive-type. Generally, the conventional sensors based on metal-foil have sensitivity in the range of 2-5, whereas the sensors composed of semiconductor have GFs of 100 or more²¹. As to the stretchable sensors based on polymer composite, the value of GF depends on the nanostructure of the composite, sensing mechanism as well as nanomaterial. Generally, piezoresistive-type sensors tend to possess higher sensitivity compared with capacitive-type ones. The piezoresistive-type sensors composed of AgNW/PDMS made by Amjadi et al. could have the value of GF up to 14, guaranteeing the enough stretchability (70%), whereas the capacitive sensor fabricated by Yao et al, which was made of two layers of AgNW/PDMS as electrodes and Ecoflex as the dielectric layer, had the lower value of GF (0.7). Notably, the linearity to strain for capacitive-type was better than piezoresistive-type.

As for the piezoresistive-type sensors, GFs usually depends on the structure of percolation network constructed by conductive fillers existing in the polymer. It can be explained by the fact that once it was deformed, the junctions between fillers would disconnect, causing the resistance to quickly rise and exhibiting higher GFs. The structure of the network is influenced by the fillers, including dispersion state, concentration and shapes. Generally, fillers with high aspect are preferred to be employed, due to the convenience of constructing the network. Li et al. adopted graphene foam which has 3D figures as fillers to construct network. Thus the sensors were endowed with rather excellent sensitivity in the range of (47.71-98.66)¹³². In contrast, the sensitivities for one-dimensional fillers, like AgNW, CNTs, are usually around 20. Nevertheless, graphene foam deteriorates the stretchability of the composite. Except the simple sensor solely made of the polymer composite, the strategy of optimizing structure of the sensor is adopted by researchers

widely. To enhance the linearity of the sensor, Roh and his co-workers sandwiched the SWCNTs layer with two conductive layers composed of PU-PEDOT:PSS, resulting in an improvement of conductivity and the stability¹¹⁹. Although the GF was reduced from around 80 for the sensor made of SWCNT layer to 10 approximately, it was enough to monitor some apparent motions. Moreover, the linearity to strain was considerably improved in practical applications.

For the capacitive-type sensor, even though they can perform with excellent stability and response speed, the sensitivity ($GF < 1$, seeing the Table 2-3) is relatively low due to theoretical limitations. For instance, AgNW network based stretchable strain sensors with Ecoflex dielectric layers showed GFs of 0.7³⁵.

2.4.2.3 Durability

Table 2-3 Summary of performance results of stretchable strain sensors reported in recent literature

Reference	Type of Sensor	Material	Gauge Factor	Stretchability	Linearity
37	Piezoresistive	CNTs-Ecoflex	1.75	300%	linear
11	Capacitive	CNTs-PDMS	0.97	300%	linear
132	Piezoresistive	GF-PDMS	47.71-98.66	30%	linear
138	Capacitive	SWCNT-PDMS	0.99	100%	linear
119	Piezoresistive	SWCNT-PU-PEDOT:PSS	8.7-62.3	100%	nonlinear
145	Piezoresistive	CNTs-TPU	1-5	400%	nonlinear
146	Piezoresistive	CNS-Ecoflex	4.3-18.4	45%	three linear regions
16	Piezoresistive	CNTs/ETC-PTHF	10-76	50%	nonlinear

22	Piezoresistive	AgNW-PDMS	2-14	70%	linear
35	Capacitive	AgNW-Ecoflex	0.7	50%	linear
147	Piezoresistive	Aligned-Graphene-CNTs/PDMS	2-20000	100%	nonlinear

Durability means whether stretchable sensors can still perform well after long-term and repeated stretching/releasing cycles. Durability is rather vital if stretchable sensors are commercialized. At present, the performance of stretchable composite-based sensors always shows degradation after long-term use. This is because not only would network structure of conductive fillers inevitably deform, but also the polymer or fillers could not sustain a large amount of deformation in the long term. Therefore, studies concentrate on the enhancement of interfacial bonding between fillers and matrix and dispersion of fillers to avoid fracture under an intensive stretch. In parallel, the intrinsic properties of polymer matrix and fillers are important as well^{31, 148}.

2.4.2.4 Hysteresis

Hysteresis is a critical exponent for stretchable strain sensors, which means the deviation between the electrical signal during the period of strain increasing and releasing. Large hysteresis behavior results in inaccurate sensing performance upon dynamic loading^{121, 149}. Generally, resistive-type sensors exhibit worse hysteresis performance compared with other types of sensors due to their sensing mechanism. There are two factors causing the hysteresis phenomenon: the viscoelastic nature of polymers and the interaction between nanomaterial fillers and polymers^{145, 150}. In retrospect, severe hysteresis would be observed when the polymer composite was being subjected to a fairly large strain. For instance, the AgNWs-PDMS nanocomposite sensors fabricated by Amjadi et al. exhibit negligible hysteresis until strains up to 40%.²² In addition, the interaction between nanomaterial fillers and polymers is another cause. If the interfacial binding between

fillers and polymer matrix were strong, the composite would exhibit excellent mechanical property, thus with favorable sensing performance^{151, 152}. On the contrary, weak interfacial adhesion between fillers and polymers tends to result in sliding of fillers inside the polymer matrix upon high stretching while fillers cannot quickly go back to their original positions after the release of strain, leading to high hysteresis behaviour¹³¹. However, if the interfacial binding was too strong, it would also induce buckling and fracture of the nanomaterial at the releasing cycle.

2.4.2.5 Response time

Response time means how quickly the strain sensor responds to the strain variation. Response delay inevitably exists in all strain sensors based on polymers because of the viscoelastic nature of polymer¹⁵³. Therefore, the resistive-type sensor generally shows larger response time than other types of sensor. For instance, the stretchable resistive-type strain sensor based on CNTs/Ecoflex exhibited a response time of 332 ms due to the ultra-softness of the Ecoflex elastomer, providing lower force for the rapid reconstruction of the CNT percolating network³⁷. However, Zhu et al. invented a capacitive-type strain sensor based on AgNWs and CNTs which possessed response time of only 100ms³⁵.

2.4.3 Applications

There are a variety of potential applications for stretchable sensors based on CNTs/polymer nanocomposite. On the one hand, highly stretchable sensors can be utilised to detect and monitor human behaviors, like body motions, heartbeat, respiration and so forth^{41, 154}. They can be implanted into warble devices and clothing, or directly laminated on the human skin. On the other hand, stretchable sensors are an indispensable part in the manufacture of soft-bodied robots and beneficial to the development of

electronic skin. In spite of the fact that simple stretchable sensors merely based on CNTs/polymer nanocomposites usually can exhibit excellent performance, the improvement of the structure of the sensor can endow them not only excellent performance but also various functions^{3, 155}. Here, some outstanding designs of stretchable sensors are reviewed, which will help to develop novels sensors in our research.

Roh et al. described a novel sandwich-like stacked piezoresistive nanohybrid film of SWCNTs and a conductive elastomeric composite of polyurethane (PU)-poly(3,4-ethylene dioxythiophene) polystyrene sulfonate (PEDOT:PSS)¹¹⁹. It is noticeable that the resistance change is caused mainly by the detachment between SWCNTs and PEDOT:PSS, not usually the separation of CNTs, increasing strain responsivity. Also, due to this sandwich-like structure as shown in Figure 2-8, the sensor not only possessed high stability, with little change of intrinsic properties after experiencing 1000 cyclic stretching tests under strains of 20% to 30% but also provided high sensitivity under little strain, thus capable of detecting facial expressions.

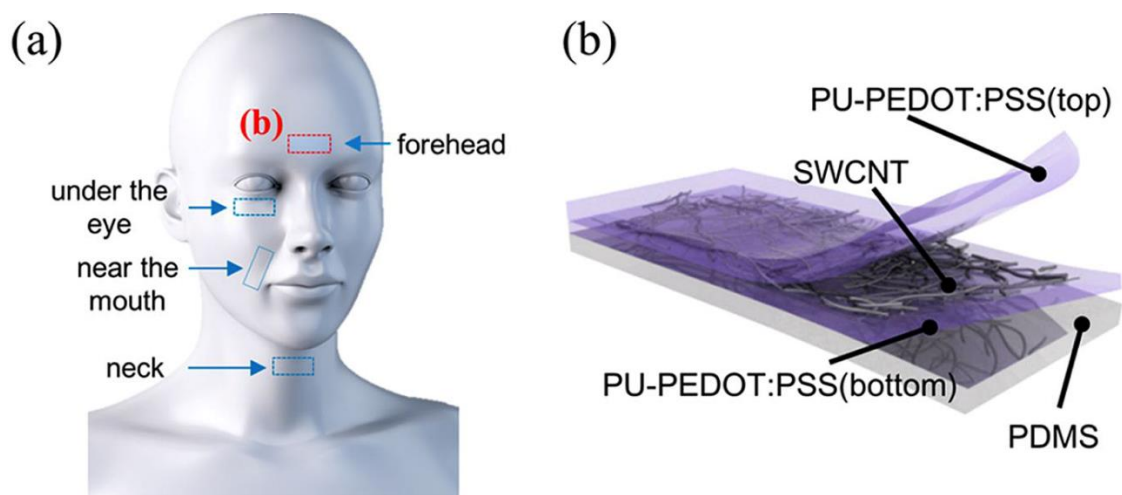


Figure 2-8 (a) Schematic illustration of stretchable transparent ultrasensitive strain sensors attached to face to sense skin strains induced by muscle movements during expression of emotions and daily activities. (b) Schematic illustration of the cross-

section of the strain sensor consisting of the three-layer stacked nanohybrid structure of PU-PEDOT:PSS/SWCNT/PU-PEDOT:PSS on a PDMS substrate¹¹⁹.

To implant the stretchable sensors into the wearable devices or clothing, Robert and his co-workers directly sprayed CNTs/polymer composite onto a PET woven textile layer by layer. Furthermore, to improve the CNTs dispersion state and composite adhesion on the PET woven textile, polymers were selected after calculation of their χ Flory–Huggins parameters to evaluate their interactions with the PET and CNTs¹⁷. Although it successfully combined CNTs/polymer composites with woven textile, the stretchability (break length 27%) is not comparable with other stretchable sensors. However, this method provided a practical approach to integrate CNTs/polymer composites with woven textile, making great strides on smart clothing equipment.

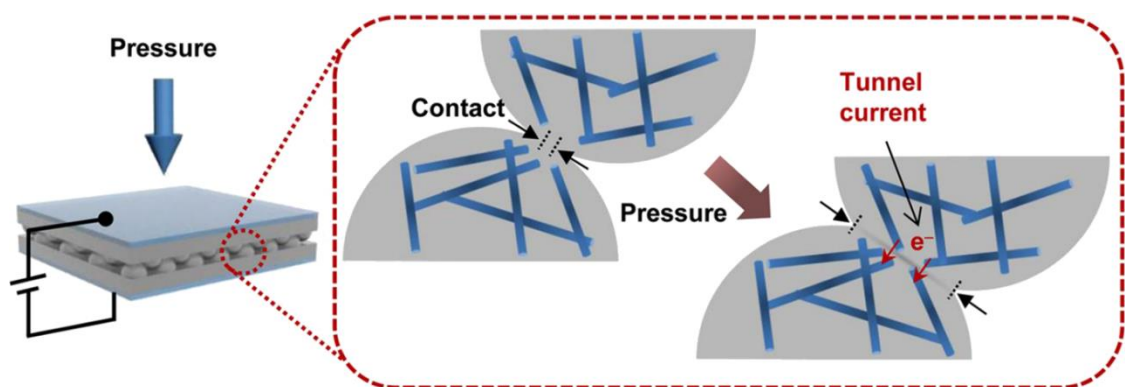


Figure 2-9 Schematic showing the working principle of the electronic skin. The external pressure concentrates stress at the contact spots, deforming the microdomes, which in turn causes an increase in the contact area and the tunneling currents¹⁵⁶.

Park et al. designed a flexible sensor based on the CNTs/PDMS composite with interlocked microdome arrays as shown in Figure 2-9. The pressure could be detected by the contact resistance between the microdomes which was dominated by giant tunneling piezoresistance. Thanks to the structure design, it endowed the sensor with high sensitivity and rapid response time, with minimal dependence on temperature variation. Besides, it was demonstrated that the sensor could be utilised to sensitively monitor minor human motions, like breathing flows and voice vibrations, showing their great potential

implementation in wearable human-health monitoring systems¹⁵⁶. Furthermore, A multi-functional sensor with rosette shape was devised by Kong et al., which can detect the direction of the principal strains¹⁵⁷. The sensor was composed of PDMS and carbon black. Although the sensitivity of this composite is not as superior as that made of CNTs or graphene, some of its advantages are still appreciated, like experimental stability, and response linearity. Also, the practical rosette structure gives it multifunction to have a great potential in diverse practical fields.

2.4 Summary

In this chapter, the CNT is introduced in terms of its structure and property, which is useful for us to choose the suitable type of CNT to synthesis the CNTs/polymer composite. In light of the price and electrical conductivity, MWCNTs with armchair structure is the ideal candidate. Then, the details regarding the fabrication of CNTs/polymer composite are described. In the manufacturing process, dispersion of CNTs in the polymer matrix is primary issue for CNTs application in the various fields due to the intrinsic nano-structure of CNTs. Some common dispersion methods are introduced and compared, finding that the ultrasonication route is suitable considering the current experimental facility, experimental convenience and the dispersion consequence. Also, the interaction between CNTs and polymer matrix is also of importance to the mechanical and electrical properties. There are two kinds of functionalization method (covalent and noncovalent). After comparing these approaches, despite the enhancement on the interaction between phases in the composite, the deterioration on the properties of the CNTs/polymer seems to be hardly avoided. Meanwhile, the diverse fabrication methods of CNTs/polymer are illustrated. Considering the fact that ultrasonication method is selected and PDMS is selected as the polymer matrix, the in situ polymerisation method is the most appropriate.

Due to the importance of electrical conductivity of the composite to the stretchable sensor, the principle of the electrical conductivity is reviewed. There are three factors affecting the electrical performance of the composite: the network structure of CNTs in the polymer matrix, the intrinsic electrical resistance of CNTs and the interfacial resistance between CNTs and polymer matrix. The previous theory of electrical conductivity paved the way for the subsequent simulation study on piezoresistivity of CNTs/polymer composite.

After that, three types of transduction mechanisms for strain sensors are described in detail. In light of the advantages of resistive-type strain sensors, like high stretchability and high sensitivity, it is considerably appropriate for the wearable devices employed to detect human motions. There are several fundamental evaluation indices for examining the performance of stretchable sensors. They include stretchability, sensitivity and durability, hysteresis and response time. Also, the various designs of stretchable strain sensors based on CNTs/polymer composites are described. They have improved the performance of the sensor or endowed multi-functions to the sensors through devising effective structures for the sensors. After a series of relevant review, it lays a solid foundation on the further investigation on stretchable sensors, in terms of the sensor design, composites fabrication, the principle of electrical conductivity, and the sensor performance characterisation.

Chapter 3 Computational Analysis of Electrical Properties

3.1 Introduction

As described above, the stretchable sensor is planned to be primarily made of CNTs/PDMS composite. Although the curvilinear shape of CNTs is helpful to build a three-dimensional (3D) network in the polymer, it inevitably raises the uncertainty of quality of the CNTs network. Also, due to the diversity of CNTs, CNTs/polymer composites would present a variety of piezoresistivity characteristics. Based on the previous literature, the Gauge Factor (GF) ranges from 0.74 to 50 with different types of CNTs¹²¹. Hence, before fabricating CNTs/PDMS composite, to find the factors that influence the piezoresistivity of these composite is essential. Simulation and modeling is a crucial and practical approach to deal with this issue. Even though recently many numerical and theoretical studies aimed at understanding the principle of electrical characteristics, there are few studies comprehensively investigating the piezoresistivity and threshold of conductivity through a realistic composite model^{158, 159}. Furthermore, to determine the percolation threshold, the empirical percolation method and power law are currently the typical ways to analyze the electrical conductivity and piezoresistivity^{160, 161}. To some extent, it is not sufficient to exhibit a clear view of the electrical conductivity variation along with the increasing of the conductive filler concentration. In particular, the critical percolation threshold is not a definite value, but a range of values. Furthermore, in the range of values, the electrical conductivity varies quite significantly. This problem was neglected by pioneering work. Hence, the range of percolation threshold should be further investigated.

Amini et al. merely proposed the concentration close to the percolation threshold that would give the composite a higher sensitivity but did not specify whether the value should be more than the percolation threshold or not¹⁶². Hu et al. have developed a 3D CNTs/polymer model to analyze their electrical behavior, while they did not further investigate piezoresistivity¹⁶³. They only pointed out the sensitivity which primarily depends on the tunneling resistance and the ratio of the tunneling resistance to total resistance^{164, 165}. For the highly stretchable polymer, the properties of the polymer play an essential role in deciding on the piezoresistivity¹⁶⁶⁻¹⁶⁸. Wang and Ye defined a value called the average junction gap variation to describe the piezoresistivity and obtained an optimizing principle for CNTs/polymer composites¹⁶⁶. Nevertheless, the principle still needs to be verified, because they obtained it through a static model, not a dynamic model. Therefore, a comprehensive theoretical study through a dynamic model to systemically find the key parameters influencing piezoresistivity is necessary.

In light of the demand of the following experiment and insufficiency of previous studies, this chapter makes an elaborate study on the mechanism and principle of CNTs/polymer composites through building a randomly dynamic 3D model. At first, after calculation of a set of numerical simulations, the critical percolation threshold range for piezoresistivity behavior is found and defined. Subsequently, parameters influencing the piezoresistivity were considered, for example, aspect ratio (AR), the electrical conductivity of CNTs and concentration, alignment of CNTs and Poisson's Ratio (PR) of the polymer.

3.2 Modelling and Simulation

3.2.1 Building the Model

To investigate the electrical properties of CNTs/Polymer composite theoretically, a 3D composite model incorporating CNTs is required to be randomly generated and basic assumptions are defined as follows:

Due to the insulation of polymers, the composite can be regarded as an equivalent conductive resistor network connected by CNTs.

In the model, a single CNT is treated as a soft-core cylinder and can be penetrated or overlapped by other CNTs.

It is assumed that the CNT is straight for accelerating computation and also its AR not very large (from 50 to 200). Despite the curvilinearity of CNTs, the factors influencing the electrical properties would not be changed.

The CNT is defined by the length L , diameter D and electrical conductivity of CNTs σ_{CNT} , with the AR being $AR=L/D$, as shown in Figure 3-1a. The length and diameter can be randomly generated subject to Gaussian Distribution. As the model has a limited boundary, some CNTs penetrating through boundary surface should be cut down. Noticeably, the AR is an approximate value, but it has little influence on precision of simulation.

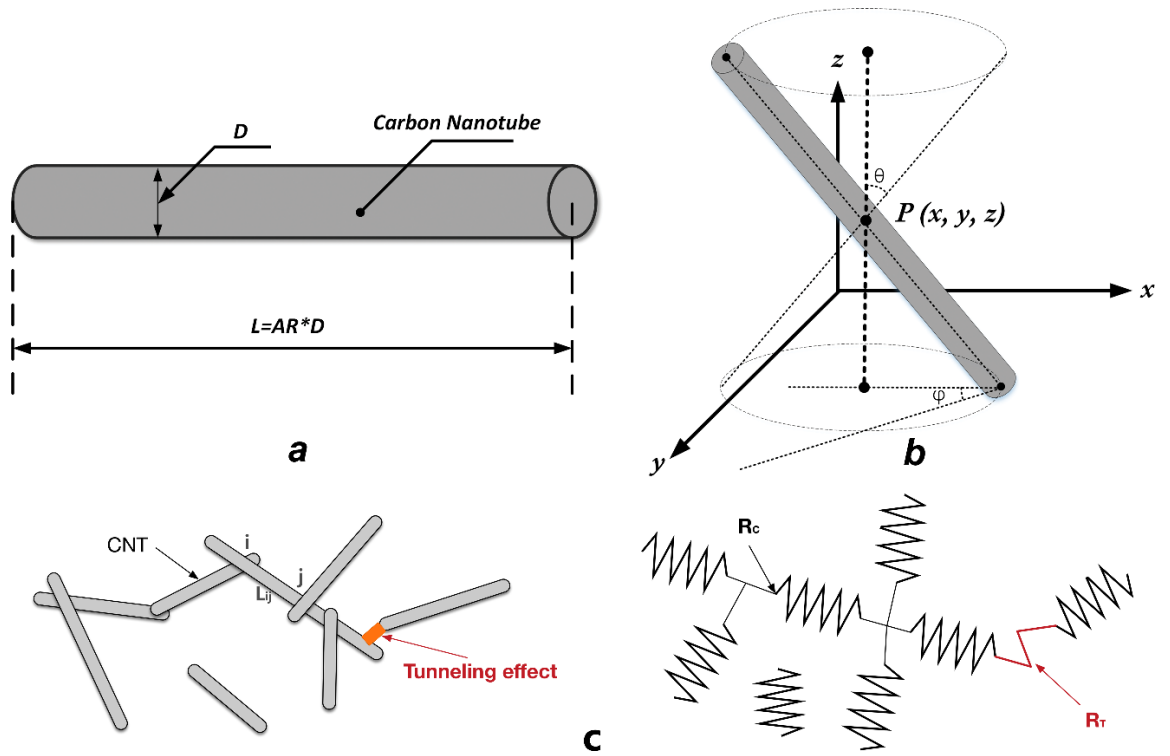


Figure 3-1 (a) Parameters of a 3D CNT, (b) Definition of location and orientation of a CNT and (c) the schematic of an electrical conductive CNTs network and tunneling effect in the resistor network.

To randomly generate CNTs, the position of a CNT is created by generating a midpoint $P(x, y, z)$, while the orientation of a CNT can be defined using azimuthal angle φ and polar angle θ , as depicted in Figure 3-1b. These parameters of CNTs could be calculated using¹⁶⁶

$$x = l_x * rand \quad 3-1$$

$$y = l_y * rand \quad 3-2$$

$$z = l_z * rand \quad 3-3$$

$$\theta = \pi * \frac{(1-2*rand)}{2*ori} \quad 3-4$$

$$\varphi = 2\pi * rand \quad 3-5$$

where l_x, l_y, l_z , are the side lengths of the unit cell, and $rand$ is a randomly generated value ranging from 0 to 1. In fact, the unit cell is set as a cube so that l_x, l_y, l_z are equal to each other. With the aim to reduce the occasion of the simulation, a dimension coefficient associated with the unit cell is created to describe the relationship between the length of

side and the average value of CNT length L . $l_m = C_v * l_0$, whereas the l_m is the side length of the cube model so $l_x=l_y=l_z=l_m$. C_v is the dimension coefficient and l_0 is the mean of the CNT. Notably, l_0 is set as 1. We managed to set the coefficient ranging from 2 to 5. When the coefficient is 2, the results may be generated with considerable discrepancy. As for the coefficient of 5 or larger, the following calculation like electrical conductivity evaluation and piezoresistivity, would spend more time. Hence, we set the coefficient as the 3 or 4. ori is the coefficient for the maximum polar angle of a CNT. Here the default setting of ori is 1. Subsequently, the coordinates of two endpoints can be expressed as follows:

$$x_e = x \pm \frac{l}{2} * \sin\theta * \cos\varphi \quad 3-6$$

$$y_e = y \pm \frac{l}{2} * \sin\theta * \sin\varphi \quad 3-7$$

$$z_e = z \pm \frac{l}{2} * \cos\theta \quad 3-8$$

where x_e, y_e, z_e are the coordinates of two endpoints, l is the length of the CNT. According to this, thousands of CNTs can be generated randomly in the unit cell. All the simulations are carried on by MATLAB and the MATLAB codes are shown in Appendix 8.

3.2.2 Resistance Calculation

To obtain the total resistance of the unit cell model, different types of resistance should be sorted out and calculated. There are two kinds of resistance, the contact resistance between CNTs and the inherent CNTs resistance, as depicted in Figure 3-1c. Actually, CNTs hardly touch each other in practice due to the existence of van der Waals force, instead, contacting CNTs would happen to be deformed^{128, 169}. Imperfect interface condition between adjacent CNTs and polymer matrix leads to increasing electrical resistance¹⁶⁸. Also, the interface conductivity can be enhanced by electrical tunneling

effect so that the interfacial resistance should be evaluated theoretically through combining contact resistance with tunneling resistance^{168, 170}. As shown in Figure 3-1c, R_t represents the tunneling resistance and the contact resistance is denoted by R_c . However, Alborz et al¹⁶² and Hu et al¹⁶³ insisted on assuming that the CNTs could be assumed to penetrate with each other with perfect interface. Hence, the interfacial resistance was only considered as the tunneling resistance without consideration of contacting resistance in their simulations. In light of the computational cost, this work assumes that CNTs could perfectly penetrate with each other without contact resistance. Therefore, in the unit cell, if the distance d , between the centerlines of CNTs, is smaller than the diameter of CNT, the contact resistance can be neglected, whereas the contact resistance is regarded as tunneling resistance, when d is larger than D and shorter than the critical tunneling distance. The tunneling resistance R_t as the primary contact resistance is calculated by¹⁷¹:

$$R_T = \frac{V}{AJ} = \frac{P^2 h}{Ae^2 \sqrt{2m\lambda}} \exp\left(\frac{4\pi h}{h} \sqrt{2m\lambda}\right) \quad 3-9$$

where J is the tunneling current density and V is the electrical potential difference with A being the cross-sectional area of the tunnel. P is Planck's constant, e and m is the charge quantum and mass of an electron, respectively. h is the minimal distance between the surfaces of two adjacent CNTs. It can be obtained by $d-D$. It needs to be noted that the cut-off distance for tunneling effect is set to be 1.8 nm according to previous work¹²⁷. λ is the barrier height of the polymer matrix (around 0.5-2.5 eV) and 1.5 eV was selected here¹⁶⁵.

The different network structures of CNTs induce different inherent resistance. As shown in Figure 3-1c, the active conductive segments are merely the connected paths, which also connect the end electrodes of the unit cell. Besides, the conductive section of a CNT L_{ij}

is the length between contacting junctions i and j as depicted in Figure 3-1c. Therefore, the resistance and the electrical conductivity of the active conductive segment of a CNT can be calculated by:

$$R_{ij} = \frac{4L_{ij}}{\sigma_{CNT}\pi D^2}, C_{ij} = \frac{1}{R_{ij}} \quad 3-10$$

where L_{ij} is the distance between two contacting points i and j . R_{ij} , C_{ij} are the resistance and conductivity of the effective conductive segment of a CNT, respectively.

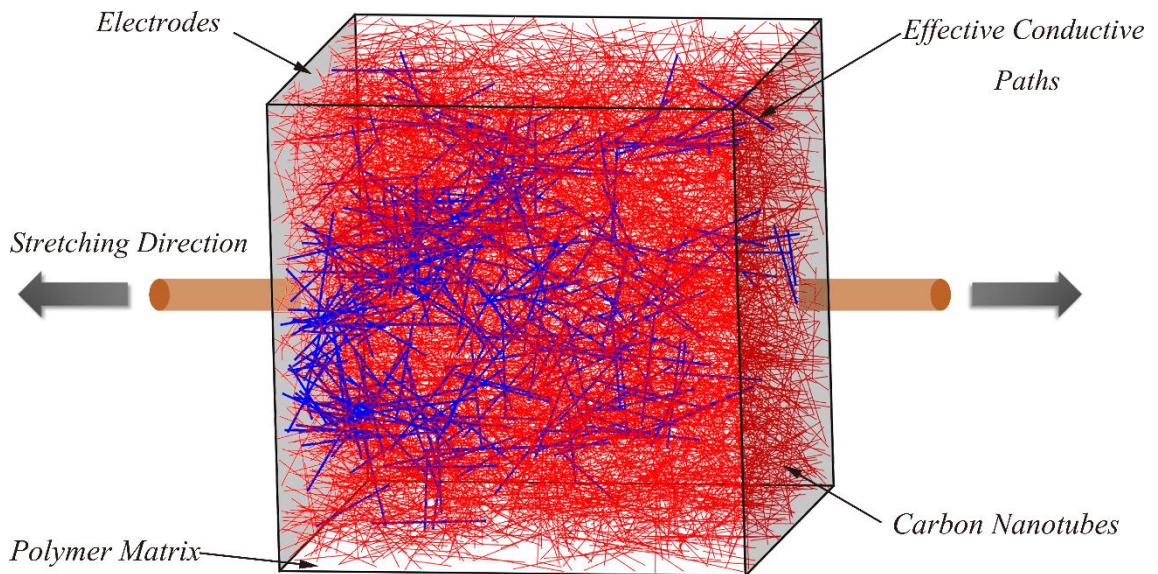


Figure 3-2 A 3D representative cube model with conductive paths depicted using blue color and bold line.

The next step is to find the active conductive network in the unit cell along the voltage direction. In this work, all the contacting junctions are firstly marked, then clusters which do not connect to the end surfaces applied on voltages should be deleted. Notably, to accelerate the computation, the unit cell is divided into small regions so that only CNTs in the same region need to verify whether it is contacted. After that, some redundant paths of CNTs should be removed¹⁶². As indicated in Figure 3-2, the bolded and blue lines are percolating CNTs, thin and red lines are CNTs without electrical current. Based on the

concise resistor network under an applied voltage and Kirchhoff's Current Law, the total electrical current at every node can be written out as follows:

$$I_i = \sum_j^{N_i} C_{ij}(V_i - V_j) \quad 3-11$$

Here N_i is the total number of nodes near the node i , and V_i and V_j are the electrical potentials of points i and j . The potential of nodes situated on the positive and negative electrodes are assumed to be 200 and 0, respectively. Hence the linear sparse matrix is listed and estimated using the Biconjugate gradients (BICG) method¹⁷². After the total electrical current I is acquired, the macroscopic electrical resistance of the model R_m can be estimated by Ohm's law. Then its electrical conductivity can be calculated based on the formula $C_m = \frac{1}{R_m * l_m}$, where C_m is the electrical conductivity of the model.

3.2.3 Piezoresistivity Simulation

As for the piezoresistivity, it is assumed that the polymer is highly stretchable, so the positions and orientations of CNTs would have an apparent change. Here, the widely accepted re-orientation model simulation is adopted to study the response of CNTs under applied strain^{162, 166, 173, 174}. This model simplifies the strain variation without consideration of the local strain around CNTs. That is to say, the movement of CNTs would not be influenced by polymer matrix. This is because the Young's Modulus of the CNT is far bigger than the polymer matrix so that the polymer's body is considered to absorb all of the applied stress and strain in nanotubes is neglected¹⁶². Even though there are other complicated models built to simulate the strain variation regarding the CNTs/polymer composite, they mainly concentrated on the mechanical properties instead of electrical properties¹⁷⁵⁻¹⁷⁷. For instance, Shokrieh et al.²⁶ used Newton-Raphson iterative method to analysis the non-linear behavior of the van der Waals force in order

to simulate the CNTs movement when the model was stretched. Mohammadpour et al.²⁸ also built a nonlinear representative volume element of composite to predict its mechanical behavior. In this model CNTs are thought as a non-deformable and their deformation is neglected, since the Young's Modulus of the polymer (i.e. PDMS is only 1MPa at most) is much smaller than that of CNTs (around 1GPa). After stretched in a uniaxial direction of X-axis seen in Figure 3-2, the new position and orientation of a CNT can be expressed as¹⁶⁶

$$\begin{Bmatrix} x' \\ y' \\ z' \end{Bmatrix} = \begin{bmatrix} 1 - \nu * \varepsilon & 0 & 0 \\ 0 & 1 - \nu * \varepsilon & 0 \\ 0 & 0 & 1 + \varepsilon \end{bmatrix} \begin{Bmatrix} x \\ y \\ z \end{Bmatrix} \quad 3-12$$

$$\theta' = \tan^{-1} \left(\frac{1 - \varepsilon * \nu}{1 + \varepsilon} * \tan \theta \right) \quad 3-13$$

$$\varphi' = \begin{cases} \tan^{-1} \left(\frac{1 - \varepsilon * \nu}{1 + \varepsilon} \tan \varphi \right), & 0 < \varphi < \frac{\pi}{2} \\ \tan^{-1} \left(\frac{1 - \varepsilon * \nu}{1 + \varepsilon} \tan \varphi \right) + \pi, & \frac{\pi}{2} < \varphi < \frac{3\pi}{2} \\ \tan^{-1} \left(\frac{1 - \varepsilon * \nu}{1 + \varepsilon} \tan \varphi \right) + \frac{3\pi}{2}, & \frac{3\pi}{2} < \varphi < 2\pi \end{cases} \quad 3-14$$

where x', y', z' are the new coordinates of the midpoint of a CNT after a strain ε is applied, while θ' and φ' are the updated angle. ν stands for the PR of the composite. The coordinates of two end points can be calculated based on from Eq. 3-6 to Eq. 3-8.

The stretched unit cell model of the composite is then updated, so the new network of the resistor is formed as well. Repeating the above-mentioned procedure, the electrical resistance and conductivity will be re-evaluated. For better observing the piezoresistivity, the GF is introduced which is defined as follows:

$$GF = \frac{\Delta R / R_0}{\varepsilon} \quad 3-15$$

Here, R_0 is the initial resistance and ΔR is the difference between the value of resistance after being stretched and the initial value. All the computation is implemented by the MATLAB and the code is listed in the Appendix 8.

3.3 Static Electrical Behavior Analysis

To better determine the dominant factors that influence the static electrical properties and piezoresistivity of composite, it is assumed that CNTs dispersed evenly in the polymer without agglomeration. Several common factors are taken into consideration here, including CNTs concentration, AR of CNTs, the electrical conductivity of CNTs, PR of the composite as well as the direction of CNTs.

Previously researchers regarded the percolation threshold as the best concentration to make sensors considering that sensors were only capable of experiencing small strain¹⁷⁸. However, this is not suitable for the current highly stretchable sensor. This is attributed to the fact that it has no conductivity after drastically stretching due to damage to the CNTs' network.

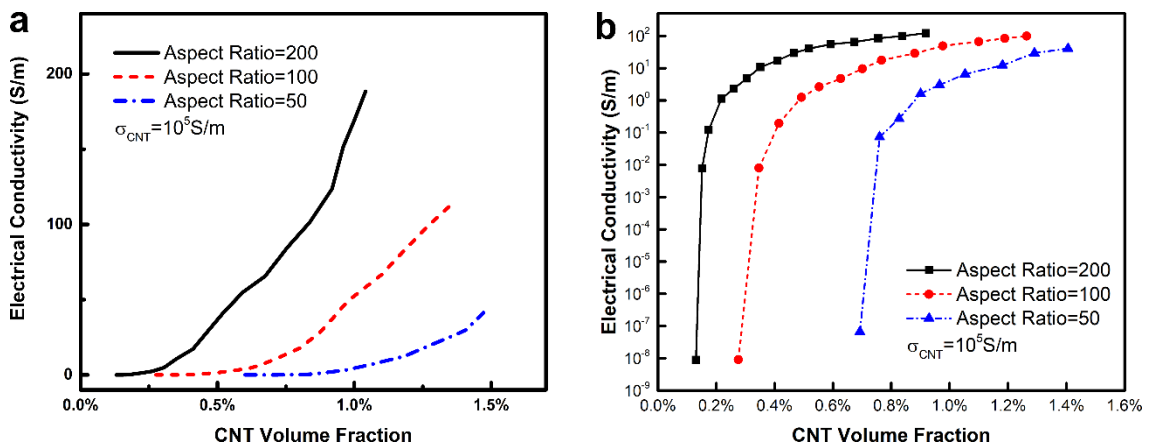


Figure 3-3 The relationship between CNT Volume Fraction and electrical conductivity of the composite with different aspect ratios using linear scale (a) and logarithmic scale (b).

3.3.1 Influence of CNT Volume Fraction

After 100 simulations, the maximum likelihood estimator (MLE) of the electrical conductivity was obtained through Poisson distribution, and the correlation between MLE of electrical conductivity and CNT volume fraction (CVF) was plotted. As shown in Figure 3-3a, the electrical conductivity experiences an exponential rise before the CVF of 1.8%. If the AR of CNTs becomes larger, the slope of the curve of conductivity against CVF will be enlarged. Meanwhile, the starting percolation threshold would be rather different. Along with AR decreasing, the larger CVF is needed to construct the conductive network in the unit cell. It can be clearly seen in the Figure 3-3b that the starting percolation threshold for AR 200 is just around 0.2% of CVF, whereas it is required to be 0.4% and 0.7% for AR 100 and 50, respectively, assuming that 10^{-7} S/m is the threshold value to be conductive. After threshold, the conductivity should vary following the power law

$$\sigma = \sigma_{CNT}(f - f_c)^t \quad 3-16$$

where σ , σ_{CNT} and f are the electrical conductivity of composite, the intrinsic conductivity of CNTs and the CNT volume fraction, respectively. f_c is the percolation threshold, and t is the critical exponent. The variation process of electrical conductivity in Figure 3-3b exhibits agreement with this formula.

To further validate the model, the Bruggeman effective medium theory for electrical conductivity of the electronic composite is employed for contrast¹⁷⁹⁻¹⁸¹. Based on this theory, an equation is given as follows:

$$9(1 - f) \frac{K_m - K}{2K_m + K} + f \left[\frac{K_c - K}{K + L_x(K_c - K)} \right] = 0 \quad 3-17$$

Where f denotes the CVF while K is the electrical conductivity of the composite. K_c and K_m are the electrical conductivities of the CNTs and the polymer matrix respectively. Here K_c is set as 10^5 S/m and K_m is assigned with 10^{-13} S/m. L_x is the depolarization factor depending on the AR of CNTs which can be expressed as

$$L_x = \frac{1}{2(AR^2-1)^{3/2}} \left[AR \ln \frac{AR+\sqrt{AR^2-1}}{AR-\sqrt{AR^2-1}} - 2\sqrt{AR^2-1} \right] \quad 3-18$$

L_x is equal to 0.0004299 and 0.0001248 for AR 100 and 200 respectively. The projection generated by our model is then compared with the Bruggeman theoretical estimation from Eq. 3-17 as depicted in Figure 3-4a. With regards to both CNTs with AR 100 and 200, the projection produced by this paper shows a moderate agreement with the Bruggeman theoretical estimation.

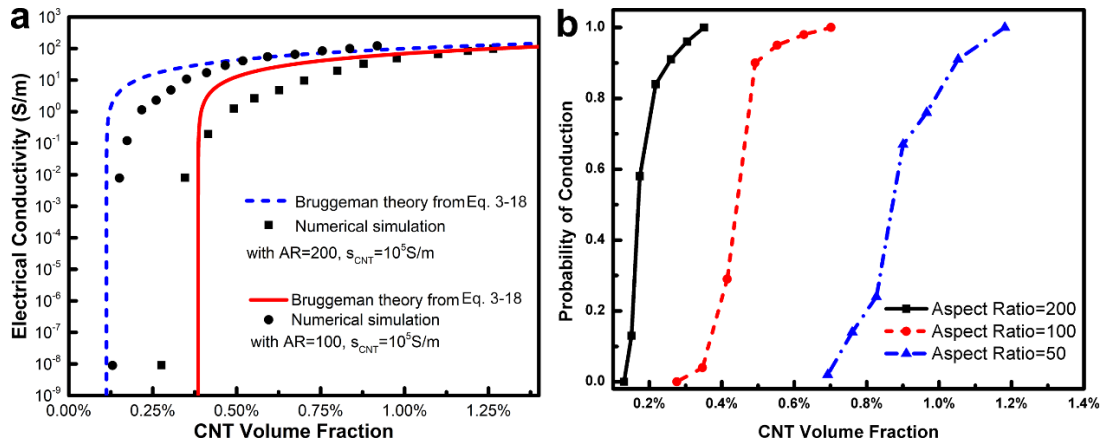


Figure 3-4 (a) The comparison between the Bruggeman theoretical estimation³⁰⁻³² and the evaluation of electrical conductivity of the composite in this paper and (b) The relationship between the probability of conduction and the CNT Volume Fraction for composites models with different aspect ratios.

In the 100 simulations, some results show no electrical conductivity around percolation threshold. Notably, the criterion to judge whether the composite model is electrically conductive or not is set as the electrical conductivity of 10^{-6} S/m. As is well-known, the electrical conductivity of 10^{-8} S/m is the threshold for material transition from insulator to semiconductor. Therefore, we amplified two magnitudes of this value to guarantee that

these results can be definitely envisioned as semiconductor or conductor. On one hand, this is attributed to the fact that the model is not large enough. On the other hand, due to the network is randomly formed, it cannot be guaranteed that the conductive paths appear every time. Hence the probability of conductivity was taken into account along with the variation of CVF. The likelihood of conductivity means that the probability to produce the conductive paths of CNTs in the composite model. As depicted in Figure 3-4b, it can be seen that when the CVF for AR 200 reaches around 0.3%, the probability of conduction is 100%, whereas the CVF for AR 100 and 50 are 0.6% and 1.2%, respectively. It means that the composite model must be conductive after this value, provided that CNTs are dispersed evenly and randomly. Thus it can be called the ending percolation. The CVF between these two values is defined as percolation threshold range (PTR) in this work. Notably, the PTR is wider for AR 50 than the other two. It can be explained that CNTs are difficult to touch with other CNTs at the same CVF when the AR is lower. Thus, even if CVF was considerably large, the model still probably shows no conductive. As a result, if the AR of CNTs is larger, lower CVF is needed and the probability of conductivity is improved. However, it is much more difficult to disperse CNTs without agglomeration using CNTs with large AR, due to the effect of van der Waals force.

Except for the CVF, the intrinsic electrical conductivity of CNTs and the orientation of CNTs would influence the electrical conductivity of composite as well. It can be seen in Figure 3-5a that the electrical conductivity of composite can be enhanced as the electrical conductivity of CNTs grows. However, the variation process does not change because the connected paths have no change in the model. As to the orientation of CNTs, only the polar angle was taken into consideration, which is controlled by the parameter Ori mentioned above. The azimuthal angle has little effect on the electrical conductivity along the z-axis direction so that it is generated ranging from 0 to 2π .

3.3.2 Influence of CNTs Polar Angles

To investigate the relationship between the polar angle and electrical conductivity, the maximum polar angle is introduced. Along with the growth of maximum polar angle, the electrical conductivity turns better, as indicated in Figure 3-5b. When the maximum angle is 15° , that is to say, CNTs are nearly parallel with each other, it is difficult to have junctions so that connected paths would hardly be formed. The number of conductive CNTs will also increase as the maximum polar angle become larger (red dash line in Figure 3-5b). It means that the electrical conductivity would be improved if the extent of alignment of CNTs is worse, which would give more chances to CNTs contacting with each other. It also can explain why the resistance of stretchable composites would go up after stretching to some extent, due to the orientation of CNTs turning consistent.

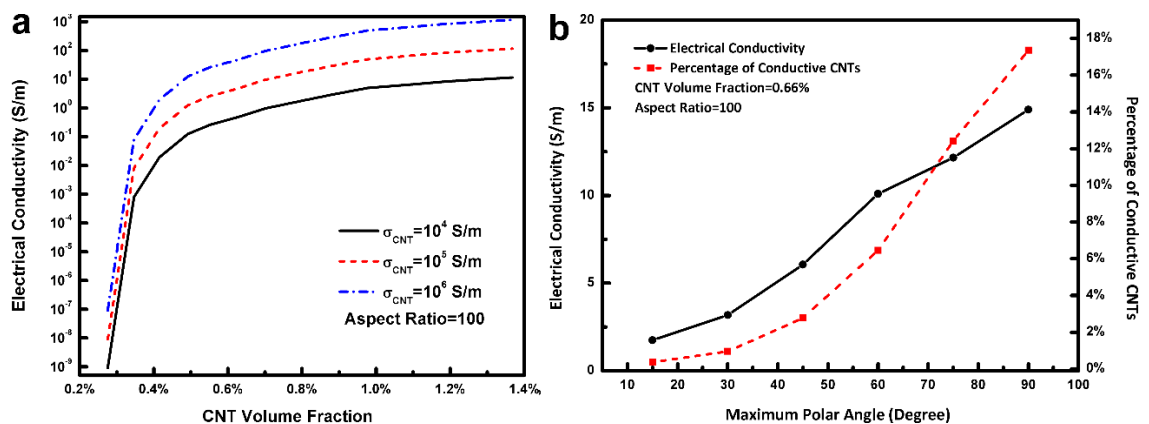


Figure 3-5 Influence of the electrical conductivity of CNTs on the electrical conductivity of composites and (b) the relationships between the maximum polar angle and the electrical conductivity of the composite as well as the percentage of connected CNTs.

3.4 Piezoresistivity Analysis

Piezoresistivity is more complicated to analyze, compared with the static electrical behavior. It does not only relate to the properties of CNTs but also involves mechanical properties of the polymer matrix.

3.4.1 Effect of CVF on Piezoresistivity

As is well-known, CVF plays an important role in influencing the piezoresistivity. Hence, the CVF is firstly studied through simulation. Assuming that PR of the composite is 0.25, and the AR of CNTs is 100, the relationship between tensile strain and resistance change (the difference between initial resistance and current to initial resistance) can be described as shown in Figure 3-6a. Three different CVFs (i.e., 0.6%, 0.7%, and 0.8%) are selected for comparison, which are slightly bigger than ending percolation threshold. Worthy of mentioning is that in spite of the influence of CVF on PR, the PR for the models with different CVFs are similar¹⁸². The resistance of the composite increases while the model is being continuously stretched. It is observed that the GF of the model with CVF 0.6% is the largest among them (the slope of the function between stain and resistance change depicted in Figure 3-6a) while that of CVF 0.8% is the least. This is because it has a high probability for CNTs to contact with each other with larger CVF. This means that when the material was stretched, more junctions and conductive paths are left behind. In addition, once the unit model is uniformly stretched, due to the influence of the composite PR, the CVF will change. Therefore, when the tension strain is applied, not only the resistance change will occur but also the CVF will vary as well. The CVF variation under applied tension strain is depicted in Figure 3-6b. It can be clearly seen that all of models with different CVFs exhibit the downward trend, which indirectly reflects the decreasing probability of mutual contacting of CNTs.

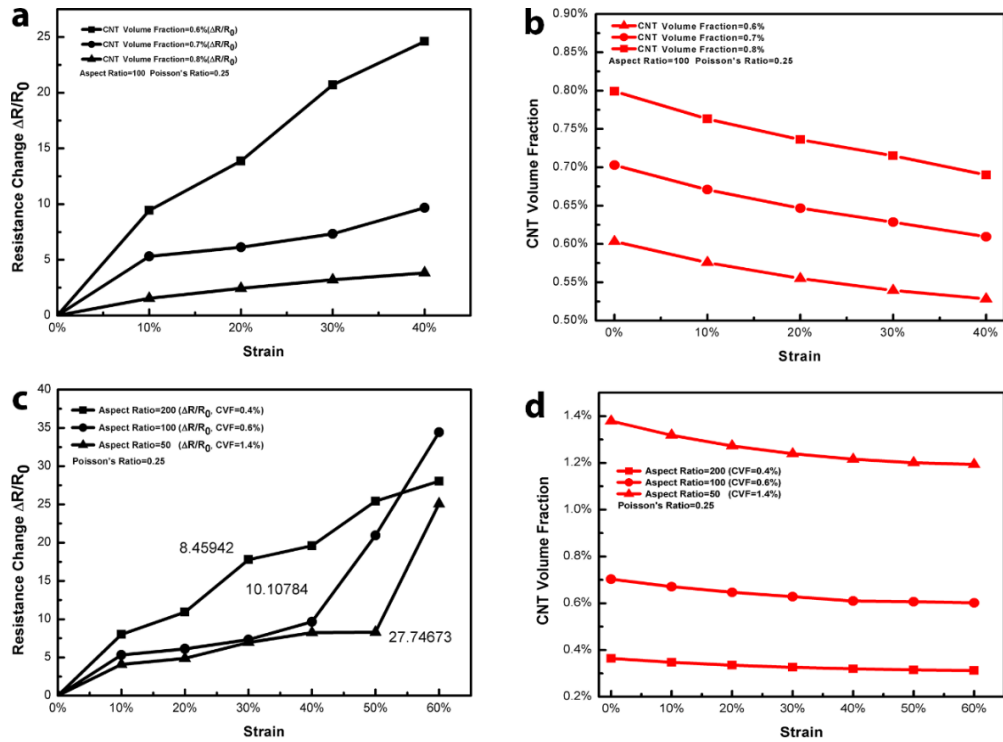


Figure 3-6 The relationship between strain and resistance change for composites models (a) with different CNT Volume Fractions and (c) with different aspect ratios as well as CNT Volume Fractions. The correlation between CNT Volume Fraction variation and strain for composites models (b) with different CNT Volume Fractions and (d) with different aspect ratios as well as CNT Volume Fractions.

3.4.2 Effect of AR on Piezoresistivity

As for the AR of CNTs, it shows little significance to compare the piezoresistivity for models with similar CVFs and different ARs. Hence, the models whose CVFs are slightly larger than ending percolation threshold are more suitable to be selected for comparison (0.4% for AR 200, 0.6% for AR 100, 1.4% for AR 50). Notably, if the CVF is selected in the PTR, the electrical conductivity would become zero within small strain due to the lack of sufficient conductive paths in the model. Meanwhile, the electrical conductivity is similar for AR 100 and AR 200, whereas the model of AR 50 has 27.74673 S/m. As shown in Figure 3-6c which described the relative change in resistance as a function of strain variation, it can be seen that the GF for AR 200 is the largest before the strain is 0.4. After strain goes over 0.4, the GF for AR 100 suddenly increases, overpassing that of AR 200, while the GF for AR 50 also surges after strain 0.5. This can be explained by

the fact that the conductive paths have a significant decline in the model at that time, resulting in a considerable rise of the resistance. In parallel, with the rise of strain, the CVF also experiences decline as displayed in Figure 3-6d. Interestingly, the downward trend is slower for the model composed of CNTs with smaller AR. For the highly stretchable sensor, stretchability and stability are as essential as sensitivity. Obviously, CNTs with large AR are the better choice to be candidates material for the stretchable sensor. Although intrinsic electrical conductivity of CNTs influences the electrical conductivity of composite, the conductive paths in the composite have no relationship with it. Naturally, the inherent electrical conductivity of CNTs has little influence on the piezoresistivity.

The reason why the electrical conductivity of composite decreases when it is stretched is attributed to the CNTs aligning gradually during the stretching process. As depicted in Figure 3-7, at the initial phase, CNTs have different polar angles distributing evenly from 0° to 90° . However, when it is stretched continuously, the number of CNTs with small polar angles increases gradually, on the contrary, the quantity of CNTs with large polar angles has an apparent decline. It means that the orientation of CNTs becomes parallel to the stretching direction. As mentioned in section 3.1, if the extent of alignment of CNTs along the stretching direction is higher, the electrical conductivity will go down. This is why the resistivity of the composite will grow when it suffers intense stretch.

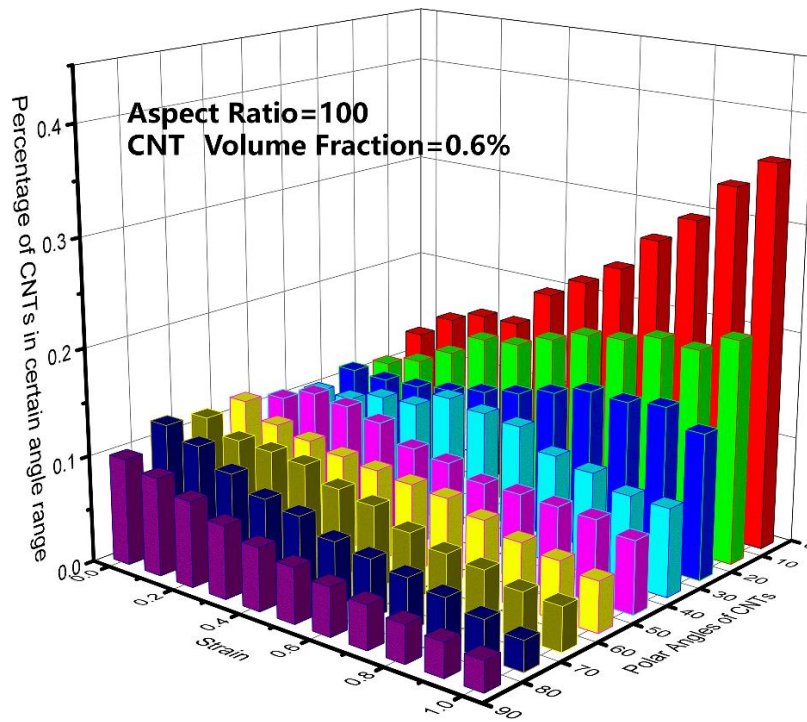


Figure 3-7 The variation of the distribution state of polar angles of CNTs along with strain increasing.

3.4.3 Effect of PR of Matrix on Piezoresistivity

The property of CNTs plays a vital role in determining the piezoresistivity, though the mechanical properties of the polymer matrix also have a significant influence on it. CNTs have a bigger Young's Modulus than that of high stretchable polymers (like PDMS), so the Young's Modulus of polymers plays a negligible part in the piezoresistivity of composite. Nevertheless, with regard to PR, the different deformation on the transverse surface under axial stretching would result in different resistance variation. Here, we compared CNTs with different PRs (0.25, 0.3 and 0.35) and the same CVF. The CVF variation and the resistance change were plotted along with the increase of tensile strain. It can be found that in Figure 3-8 that the resistance of CNTs with PR 0.25 keeps going up, while the other two happen to fluctuate after 50% strain. It can be explained that their CVFs do not go down but rise after 50%, so it gives more opportunities for CNTs to contact each other. On the contrary, CVF for PR 0.25 maintains going down until there

are no conductive paths found. Notably, the resistance for PR 0.3 and 0.35 grow again. This is attributed to the alignment of CNTs in spite of the increase of CVF. Besides, the GF will rise when the PR is smaller. Consequently, if the PR is lower, the piezoresistivity will be enhanced. For better understanding, We have added the contact CNTs percentage variation to describe it. As shown in the Figure 8.1 in Appendix, when the aspect ration of CNTs is 100 and the CVF is 0.7%, it can be clearly found that once the model is stretched, the contact CNTs percentage diminishes. Also, with the increase of Poisson's ratio, the drop rate of the contact CNTs percentage becomes slow.

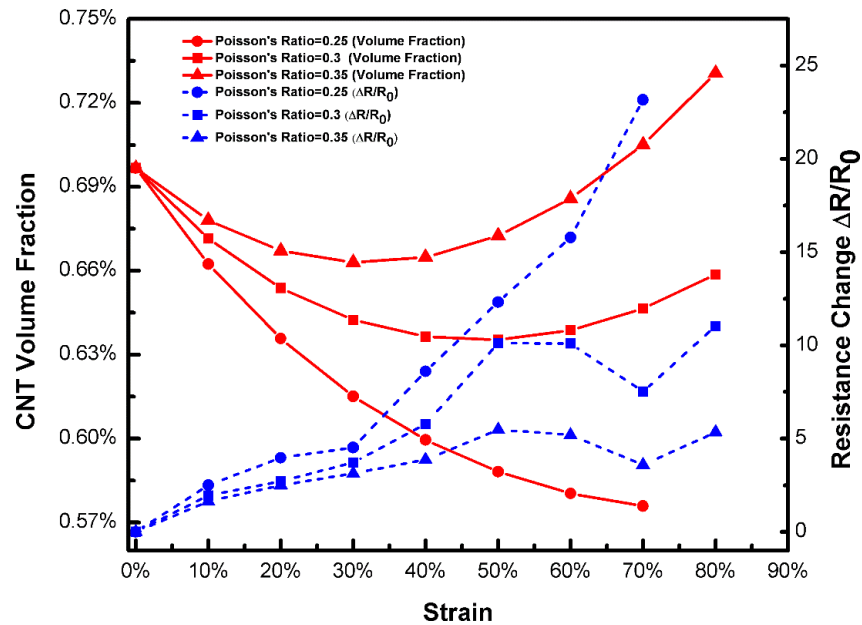


Figure 3-8 The resistance changes and the CNT Volume Fraction variation along with strain growing for composites models with different Poisson's Ratios.

3.5 Conclusion

The mechanism of the electrical behavior of highly stretchable CNTs/polymer composite was analyzed through this dynamic 3D model. It is shown that the electrical conductivity of the composite is dependent on the structure of CNTs network in the polymer. Meanwhile, the concept of percolation threshold range (PTR) is proposed, instead of the

fixed value of percolation threshold in previous literature. The PTR is determined by the AR of CNTs and orientation of CNTs primarily provided that CNTs dispersed evenly without agglomeration. The electrical conductivity of CNTs cannot affect PTR but determine the electrical conductivity of the composite. For the stretchable sensors, the CVF which is slightly bigger than the ending percolation threshold is a better option for fabricating piezoresistive sensors. As for the piezoresistivity, once the CVF is beyond PTR, the GF will reduce as the CVF increase. Also, higher AR of CNTs will not only make GF better but also will be favorable to keep GF stable. PR of composite plays an important part in influencing piezoresistivity. With lower PR, GF will be better. Furthermore, if PR is large, the GF will fluctuate once the strain is large. To conclude, CNTs with larger AR, CVF slightly higher than PTR and lower PR of the composite are positive to improve the piezoresistivity and stability of the highly stretchable sensor. Thus, in the following experimental section, we will fabricate the stretchable sensor based on CNTs/PDMS composite following this optimizing principle.

Chapter 4 Preparation of the MWCNTs/PDMS Composite

4.1 Introduction

As reported in previous literature, polymer nanocomposites embedded with carbon nanotubes (CNTs) exhibits superior piezoresistivity and good stretchability so as to have the potential to be the core material of the stretchable sensor^{30, 183}. At first, the type of the CNTs should be determined. There are two types of CNTs: single-wall carbon nanotubes (SWCNTs) and multi-wall carbon nanotubes (MWCNTs). While the SWCNTs possess more outstanding electrical properties in comparison with MWCNTs, the high price and more difficulty to deal with the issue of agglomeration makes them not as economic as MWCNTs. Therefore, the MWCNTs are employed for this work.

In terms of the fabrication of the CNTs/polymer composite, the primary and common issue is how to make CNTs homogeneously dispersing in polymer matrix. The good dispersion of CNTs in the polymer matrix not only can help to construct uniform network structure, but also strengthen the interface bonding between CNTs and polymer matrix. For instance, the stretchable sensor that Wang et al. proposed based on CNTs/elastomeric triisocyanate-cross-linked polytetrahydrofuran composite, possessed a higher gauge factor (up to 90)¹⁶. However, due to the agglomeration and mediocre dispersion of CNTs leads to deterioration of the stretchability and electrical conductivity¹⁸⁴. The reason why CNTs are apt to form clusters lies in the strong van der Waals force existing among adjacent CNTs. The big van der Waals force is related to the high aspect ratio of CNTs. Therefore, dispersing CNTs homogeneously and reducing entanglement of CNTs in solvents or polymers matrices is fairly difficult compared with other ordinary fillers at present^{128, 185}.

There are typical CNTs dispersion methods developed in previous studies, such as ultrasonication, ball milling, stir and extrusion, functionalization of CNTs and so on¹⁸⁶⁻¹⁸⁸. As introduced in section 2.3.1, ultrasonication seems to be the most effective and convenient method in the laboratory, in spite of the fact that ultrasonication for a long time would induce the generation of the defects on CNTs surface^{61, 189}. Traditionally, the ultrasonication method always disperses CNTs in polymer matrix with the assistance of solvents. Consequently, after ultrasonication the remaining solvent has to be evaporated. It is this evaporating stage that may lead to the phenomenon that adjacent CNTs aggregate again in the polymer matrix. It can be attributed to the fact that the molecular motions are strengthened by high temperature. Also, due to the shape of CNTs, once CNTs entangle with each other, it is hard to detach them because of the van der Waals force^{29, 31, 190}.

In this context, the solvent is the crucial part so that it should be cautiously selected. This is not only because the solvent influences the dispersion state of CNTs in the suspension, but also would be left behind in the CNTs/polymer mixture after ultrasonication. Therefore, if the solvent has a low boiling point and good compatibility with the CNTs, perhaps it is helpful to shorten the evaporation period and lower the evaporation temperature, thus enabling CNTs dispersing in the polymer matrix homogeneously.

This chapter focuses on how to disperse MWCNTs uniformly in the PDMS matrix. Three solvents with different boiling points are employed to fabricate the MWCNTs/PDMS composite. The influence of boiling point of the solvent on dispersion state of MWCNTs will be investigated. Three types of solvents are pentane, isopropanol alcohol (IPA) and toluene, all of which can make MWCNTs disperse well in them for a long term. The MWCNTs/ polydimethylsiloxane (PDMS) nanocomposites films are fabricated using different solvents^{149, 157, 191, 192}. Then mechanical and electrical characteristics of the

nanocomposites are measured and studied. The dispersion and distribution state of MWCNTs in PDMS matrix are morphologically observed by the field emission scanning electronic microscope (FESEM).

4.2 Experimental Investigation

4.2.1 Materials

In order to investigate the influence of the solvent on the mechanical and electrical performance of the nanocomposite, the highly stretchable polymer (PDMS) is employed. The matrix PDMS was supplied by the Dow Corning Company (Auckland, New Zealand). MWCNTs were purchased from the Graphene Supermarket. According to the supplier's specification, the length of MWCNTs ranges from 10 to 15 μm , while the average diameter is around 60 nm and the purity of MWCNTs is greater than 94%. Toluene, pentane, IPA are all bought from Sigma Aldrich. Pentane has the 35 °C of boiling point, while the boiling points of IPA and toluene are 75 °C and 120 °C respectively.

4.2.2 Selection of CNTs Concentration

To begin, the CNTs concentration needs to be determined for better observation of the influence brought by the solvent. As is all known, it is difficult to disperse MWCNTs if the MWCNTs concentration is relatively high. After all, the low boiling point of the solvent just saves the evaporation time and reduces the evaporation temperature to retard the re-agglomeration. It is unable to fundamentally overcome the intrinsic defect of MWCNTs. With the aim of observing the influence of the boiling point of the solvent, the MWCNTS concentration should not be rather high. In addition, according to the previous literature, when the MWCNTs concentration lies in the percolation threshold, range the electrical conductivity of the MWCNTs composite will be significantly

influenced by the MWCNTs network structure, compared with those with higher MWCNTs concentration¹⁶³. It can be explained by the fact that higher MWCNTs concentration than percolation threshold would undoubtedly enhance the probability of forming a continuous MWCNTs conductive network in the matrix. In this context, the influence of MWCNTs dispersion state on the electrical conductivity would diminish¹⁵⁹. In parallel, if the concentration is lower than the percolation threshold, electrical conductivity could not be measured. Hence, for purpose of investigation on the effect of solvent on the properties of the composites, percolation threshold would bring the most distinctive comparison results. We fabricated three kinds of MWCNTs/PDMS composite with MWCNTs mass fraction of 3%, 5% and 7% using pentane as a solvent. It was found that the electrical resistance of the composite with 3% MWCNTs cannot be detected by a multimeter, and the electrical resistance of the composites with MWCNTs of 5% and 7% were measured and achieved as shown in Table 4-1. There are three sets of electrical resistance data for MWCNTs/PDMS composites with 5% and 7% MWCNTs respectively. It is clearly seen that the mean value of the resistance for the 5% MWCNTs composite is 572.39 k Ω , bigger than that of the composite with 7% MWCNTs (14.43 k Ω). According to the early interpretation, 5% concentration of MWCNTs is fairly close to the percolation threshold range. Therefore, the composite filled with 5% MWCNTs is suitable to be adopted for investigation of the influence of the solvent.

Table 4-1 The resistance of four samples in each type of MWCNTs/PDMS composite with different mass fraction of MWCNTs (5% and 7%) as well as the average value of every four samples.

MWCNTs Concentration	Resistance Group A	Resistance Group B	Resistance Group C	Resistance Group D	Average Value
5%	472.53 k Ω	263.18 k Ω	1028.64 k Ω	525.19 k Ω	572.39 k Ω
7%	12.06 k Ω	18.75 k Ω	20.36 k Ω	6.54 k Ω	14.43 k Ω

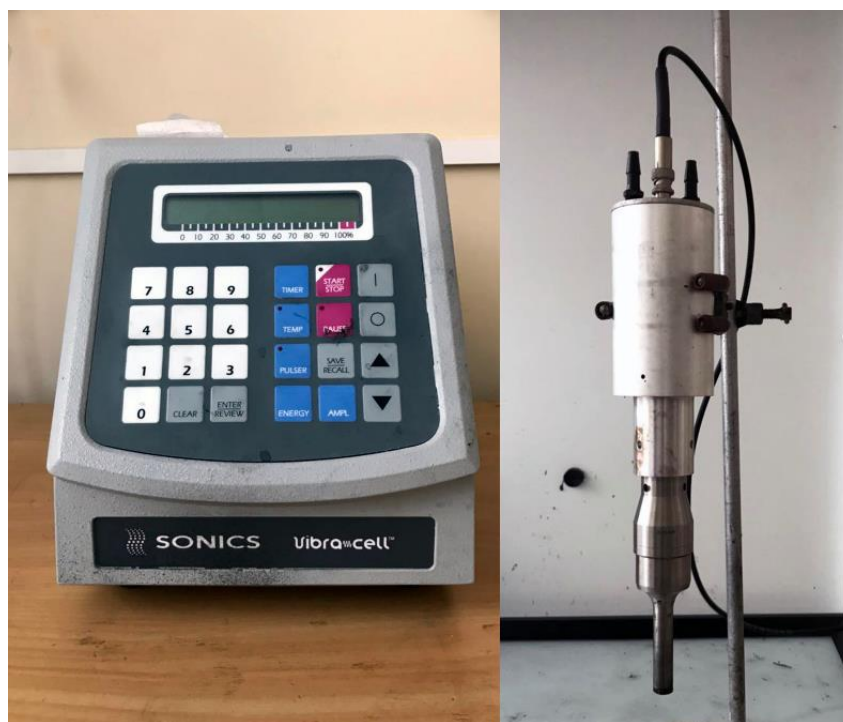


Figure 4-1 The horn ultrasonication device.

4.2.3 Preparation of CNTs/PDMS Nanocomposites

At first, MWCNTs were added into the three different solvents (pentane, IPA, and toluene) respectively and then dispersed by horn ultrasonication for 30 minutes. The horn ultrasonication device is shown in Figure 4-1. The amplitude of the ultrasonication is set as 30%. Due to the large heat quantity, the mixture solution should be put into the cold water to retard the evaporation of the solvents. At the same time, PDMS prepolymer was dissolved in corresponding solvents under magnetic stirring for 30 minutes. Next, MWCNTs suspensions were blended with respective PDMS solutions and the obtained mixtures were continued to be ultrasonicated for another 1 hour. After adding curing agents, the suspensions were heated at a proper temperature to evaporate solvents.

Afterward, the remaining mixture was uniformly coated onto a glass plate using a blade and then put into the vacuum oven to degas. This step should be carried out repeatedly until there is almost no bubble on the surface of the mixture membrane as a result of the

high viscosity of the mixture which is induced by the intensive network of MWCNTs in the PDMS matrix. It is helpful to make CNTs have better connection mutually. The membrane was sequentially heated at 80 °C for 2 hours. Finally, the glass plate with the membrane was taken out from the oven and the final membrane was peeled off from the glass plate. The schematic fabrication procedure is depicted in Figure 4-2. Notably, the composite film is rectangular and its dimension is 60 × 10 × 0.8 mm.

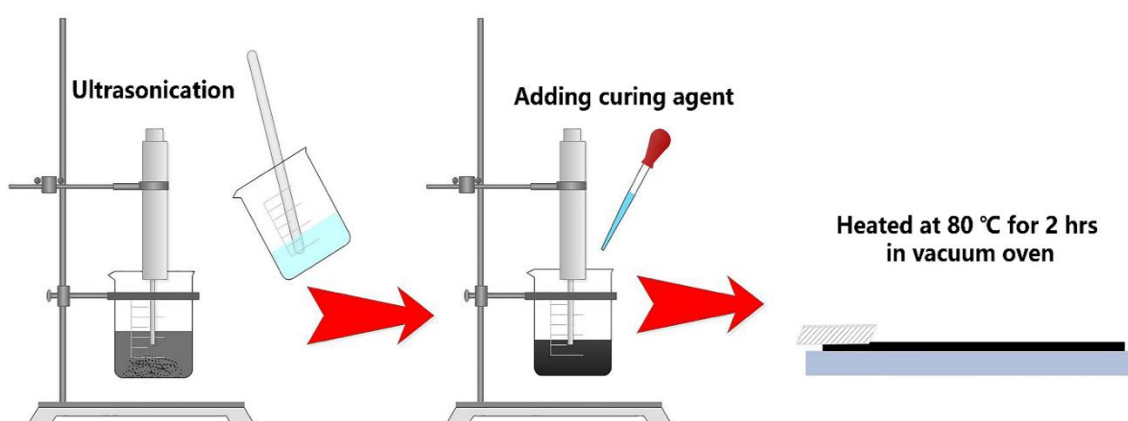


Figure 4-2 The schematic of the MWCNTs/PDMS nanocomposite film fabrication.

4.2.4 Characterization of the Nanocomposites

The as-prepared CNTs/PDMS composite film was cut from the top surface to the bottom surface. Next, the cross-sectional microstructure of CNTs/PDMS composite film was taken for observation by the field emission scanning electron microscope (FESEM, Hitachi SU-70 as shown in Figure 4-3) operating at 5 kV. Notably, the samples of nanocomposite films were coated with Pt prior to FESEM measurement. The mechanical properties of the nanocomposite were studied by the tensile test using the Hounsfield machine. The electrical conductivity of the nanocomposite film was measured by the multimeter called UNI-T UT803. The copper wires are attached on two ends of the sample by silver paste.

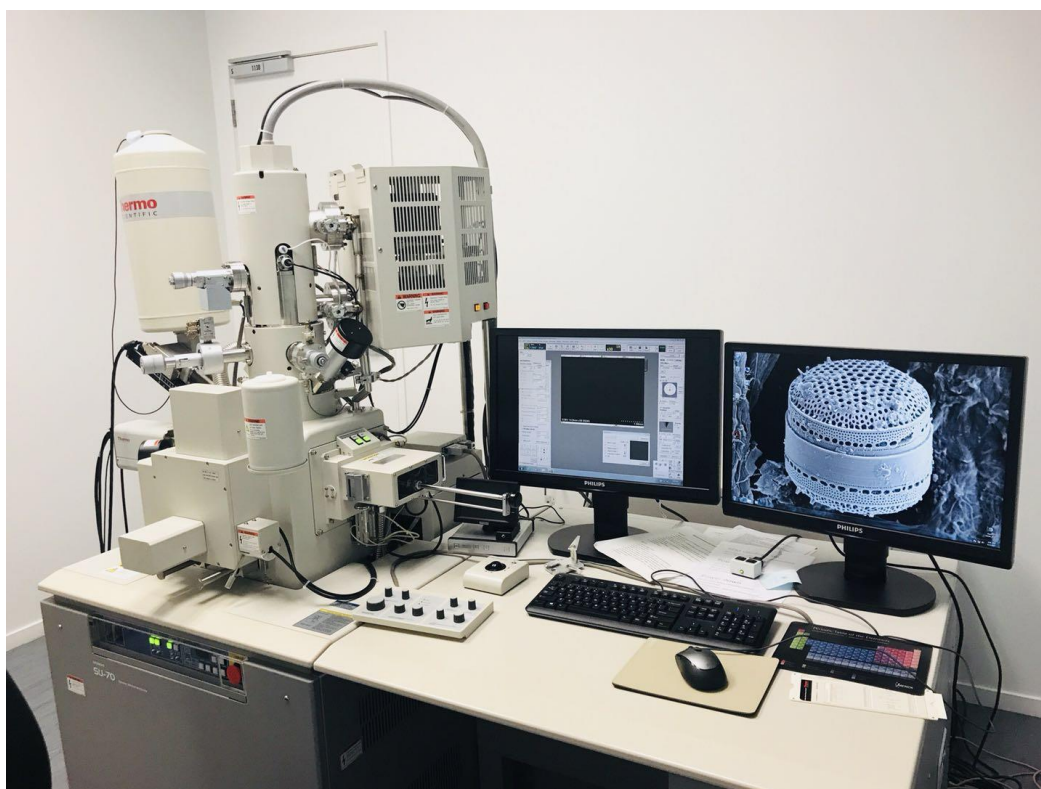


Figure 4-3 The field emission scanning electron microscope (Hitachi SU-70)

4.3 Characterization Results

4.3.1 Morphology

First of all, the microstructure of the cross-section of CNTs/PDMS nanocomposites were observed through FESEM. There are three FESEM images of microstructures of nanocomposites which are prepared using different solvents respectively. It can be found that CNTs are dispersed homogeneously in the matrix with little agglomeration (the white lines and dots depicted in Figure 4-4a) when MWCNTs/PDMS mixture is ultrasonicated using pentane as a solvent. In contrast, there are several obvious MWCNTs small clusters appearing in the PDMS matrix, which are circled by red line as shown in Figure 4-4b, when IPA was used as the solvent, whereas there is a bigger cluster which can be found in the microstructure of the nanocomposite handled by solvent toluene as marked in the Figure 4-4c. This reveals that the fabrication method that adopts the solvent with a low

boiling point can promote MWCNTs maintaining the uniform dispersion state in the matrix after ultrasonication, thus achieving the nanocomposite film with good dispersion of MWCNTs. This can be attributed to the fact that the remained solvent can evaporate quickly at a lower temperature when the solvent with a lower boiling point is employed. Hence, it is possible to avoid re-agglomeration of MWCNTs during the evaporation period due to the mitigation of the molecular motion^{49, 79}.

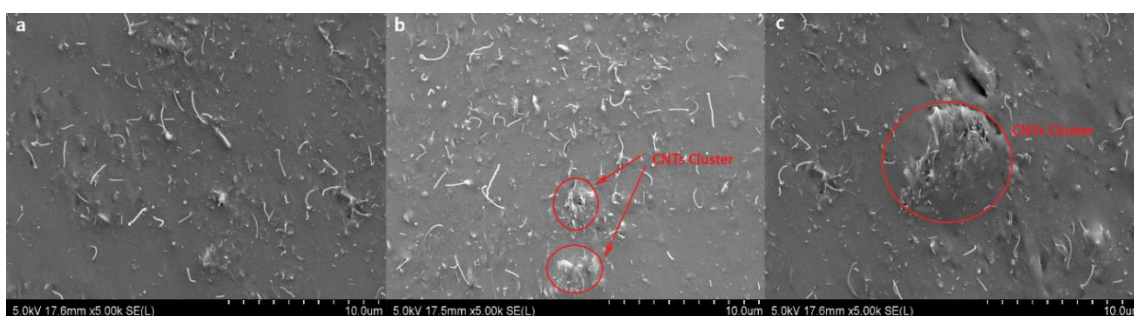


Figure 4-4 FESEM images of CNTs/PDMS nanocomposites prepared using different solvents: (a) pentane (b) IPA (c) toluene.

4.3.2 Mechanical Properties

Tensile tests were implemented on all the nanocomposite films which were prepared using different solvents. There are 4 samples for each composite group. It can be seen clearly that the tensile modulus of all the nanocomposites are enhanced compared with neat PDMS film (seeing Figure 4-5a). Besides, the nanocomposite film which is fabricated using pentane as the solvent gives the boost of the tensile modulus (around 1.4Mpa). The nanocomposite fabricated using Toluene has the highest Tensile Modulus (up to 2.1Mpa), while that fabricated using IPA shows roughly 2Mpa. This can be explained by the fact that the agglomeration of MWCNTs which can be viewed as large fillers would hinder PDMS matrix molecular chain sliding and traps PDMS in the void of the clusters of MWCNTs as well^{77, 92}. From this result, the as-prepared

MWCNTs/PDMS composite film handled by the solvent with lower boiling point exhibits lower Tensile Modulus, close to that of the neat PDMS.

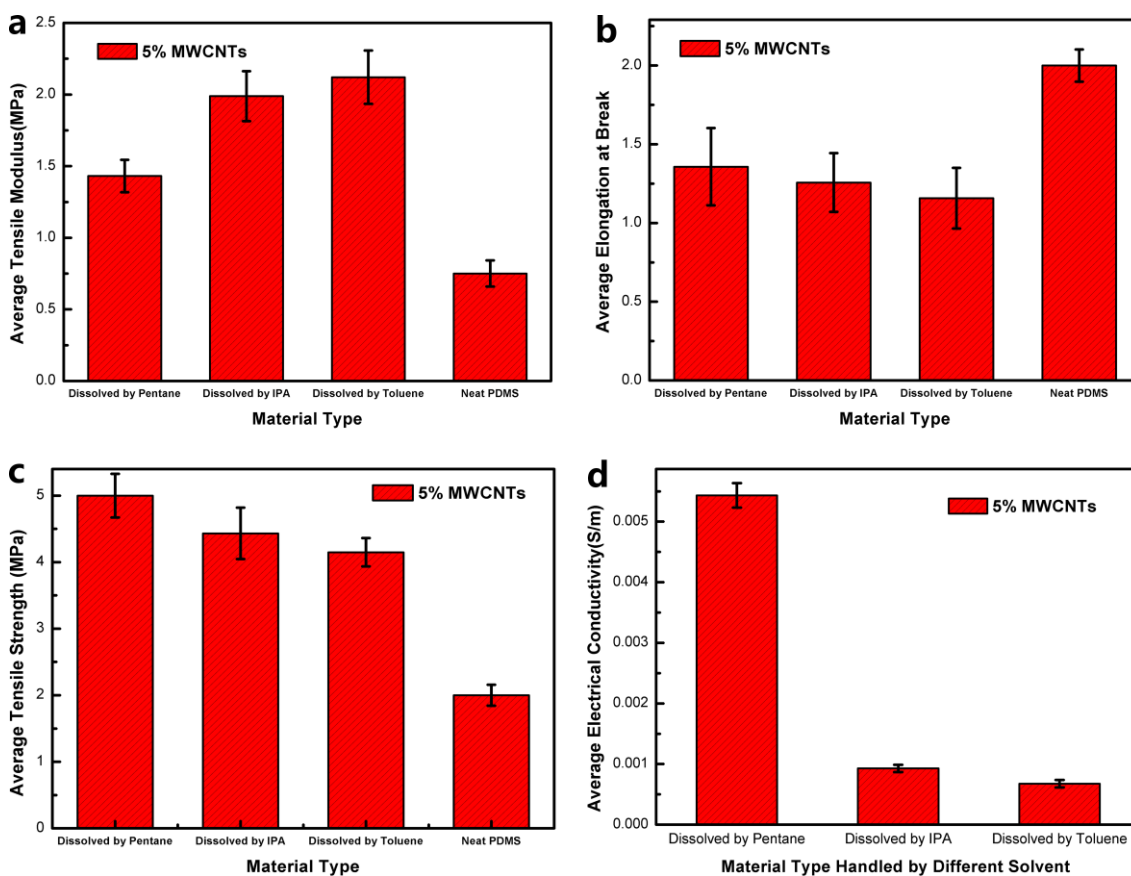


Figure 4-5 The average mechanical properties of the 5% CNTs/PDMS nanocomposite films prepared with different solvents and the neat PDMS film ((a) The tensile modulus, (b) elongations at break and (c) tensile strengths), and (d) The electrical conductivity of the CNTs/PDMS nanocomposite films incorporating 5% CNTs handled by different solvents.

However, the elongations at break for the composites films show the opposite phenomenon as depicted in Figure 4-5b. It is obvious that the nanocomposite film which is prepared using pentane as solvent exhibits the highest stretchability ($\approx 140\%$), whereas that handled by toluene can be stretched at the lowest elongation ($\approx 120\%$). Notably, The neat PDMS films could be stretched up to 200%, which is fairly larger than those of the nanocomposites films. This can be attributed to the fact that the interfacial bonding between MWCNTs clusters and their surrounding PDMS matrix are too weak to withstand the tensile loading, thus leading to their breakage⁵⁵. That is to say, the

agglomerates of MWCNTs facilitate generation and propagation of cracks in the PDMS matrix when it is pulled up drastically^{78, 189}. Also, for MWCNTs, the outer shells of the MWCNTs would slip because of the weak van der Waals force existing between individual graphene shells of the MWCNTs, when the nanocomposite is stretched¹⁹³. The solvent with lower boiling point improves stretchability of the nanocomposite film, maintaining the inherent high stretchability of the PDMS resin.

Furthermore, the tensile strengths of nanocomposite films are improved as well when the dispersion state of MWCNTs in the PDMS matrix is improved. As shown in Figure 4-5c, the tensile strength of neat PDMS film is less than other three nanocomposites based on 5% MWCNTs, which can be rationalized by the same reason as the result of tensile modulus. Nevertheless, the nanocomposite film handled by pentane exhibits the highest tensile strength (5MPa), whereas those prepared using solvent IPA and toluene shows the tensile strength of 4.4MPa and 4.1MPa respectively. It can also be ascribed to the fact that poor dispersion state tends to generate and propagate cracks easily so that the nanocomposite with the bad dispersion state of MWCNTs cannot sustain applied loading remarkably¹⁹⁴. Therefore, when the nanocomposite film is prepared using the solvent with a low boiling point, its tensile strength will be improved.

4.3.3 Electrical Properties

The electrical conductivities of all the nanocomposites that are prepared with different solvents are measured as shown in Figure 4-5d. It can be found that the composite film prepared with pentane predictably possess the best electrical conductivity (≈ 0.0055 S/m). In contrast, the nanocomposite film handled by IPA has an electrical conductivity of 0.001 S/m approximately, while the electrical conductivity of that fabricated using toluene as the solvent is around 0.0008 S/m. The electrical conductivity of the nanocomposite based

on MWCNTs/PDMS does not completely depend on the dispersion state of MWCNTs in the matrix but is related to the conductive network of MWCNTs and tunneling resistance among MWCNTs^{28, 165}. However, the homogenous dispersion state of MWCNTs is helpful to construct the conductive network in the matrix with more percolation paths¹⁹⁵. Hence, the nanocomposite film handled by solvent with low boiling can make the film more conductive electrically.

4.4 Conclusion

This chapter investigates how the boiling points of solvents influence the mechanical and electrical properties of MWCNTs/PDMS nanocomposite when the ultrasonication is employed as the dispersion approach. It is found that MWCNTs are dispersed homogeneously in the PDMS matrix when the solvent has a low boiling point due to the low temperature to evaporate. Besides, the nanocomposite film handled by the solvent with a low boiling point possesses more excellent stretchability than those handled by the solvent with a higher boiling point. In addition, with the improvement of dispersion state of MWCNTs in the matrix, the electrical conductivity of the MWCNTs/PDMS nanocomposite can be enhanced. To conclude, the stretchability and electrical performance of MWCNTs/PDMS nanocomposite are improved remarkably when a solvent with a low boiling point is utilized to fabricate the nanocomposite by the ultrasonication dispersion approach. It is beneficial for the following fabrication of the stretchable sensor based on the MWCNTs/PDMS composites.

Chapter 5 Fabrication and Characterization of the Stretchable Sensor based on the MWCNTs/CNTs Composite

5.1 Introduction

As reviewed in chapter 2, stretchable sensors based on electrically conductive polymer composites have attracted a great deal of attention due to their excellent compliance for human motion and sensitivity, compared to conventional sensors based on metal foils or semiconductors^{19, 38, 196}. Obviously, conventional sensors cannot undergo larger strain ($\gg 5\%$) and present a bad mechanical compliance with human motions. Thus stretchable polymer composites exhibit enormous potential to be employed for making electronic skin¹⁹⁷⁻¹⁹⁹, human motion detectors^{35, 200}, soft robotics^{43, 201}, smart textiles^{10, 202} and so forth²⁰³⁻²⁰⁵.

As described in chapter 4, the MWCNTs/PDMS composite film has been fabricated and the dispersion state of CNTs has been guaranteed to be homogenous as much as possible. After that, the stretchable sensor based on the MWCNTs/PDMS composite should be devised for the practical application. In terms of the stretchable sensors, the design is required to not only have excellent mechanical compliance to the human motions, but also maintain or improve the performance of the pure MWCNTs/PDMS composite, including high stretchability, good sensitivity, hysteresis and so forth^{37, 145, 206}. In other words, stretchable sensor should be ensured to be remarkable in all aspects of the sensing properties. However, at present a large number of invented stretchable sensors cannot exhibit excellent overall performance. For instance, Robert et al. invented the sensor made

of the PC-CNT nanocomposite¹⁷. Though it exhibited good sensitivity (GF up to 100), the hysteresis and stretchability are relatively poor.

In this study, based on the as-fabricated MWCNTs/PDMS composite as described in chapter 4, a stretchable sensor with sandwich-like structure is devised (MWCNTs/PDMS nanocomposite which is wrapped in the two PDMS layers). The as-prepared strain sensor not only provides adequate stretchability and great sensitivity but also possesses very fast response time, good durability and low hysteresis. Furthermore, the sensor is managed to be employed to detect human motion. When they are mounted on the wrist or finger, they can monitor the motions promptly and accurately. With remarkable overall properties, the stretchable sensor based on the MWCNTs/PDMS composite will have a considerable potential to in field of wearable electronics device in future.

Table 5-1 The amounts of MWCNTs, liquid PDMS, curing agent and solvent PDMS used in the experiment.

Weight Ratio of MWCNTs	Weight of MWCNTS	Pentane for solving MWCNTs	Pentane for solving PDMS	Liquid PDMS	Curing Agent
5%	0.25 g	50 ml	40 ml	4.20 g	0.45 g
7%	0.35 g	70 ml	40 ml	4.10 g	0.45 g
9%	0.45 g	90 ml	40 ml	4.00 g	0.45 g

5.2 Experimental Investigation

5.2.1 Materials

Multi-walled Carbon nanotubes (MWCNTs) were purchased from Graphene Supermarket. The diameter of MWCNTs ranges from 50-85 nm, and their lengths lie in the range from 10 to 15 μm . The pentane was supplied by Sigma Aldrich, while the PDMS and its curing agent were bought from Dow Corning Company (Sylgard 184). Noticeably, the experimental specific data are listed in Table 5-1. Considering the loss of MWCNTs which are probably adhesive to the beaker, the actual added liquid PDMS is

less than the theoretical amount. In addition, the ratio of liquid PDMS and curing agent is 10:1 theoretically, but for better curing of the mixture, slightly more curing agent is added.

5.2.2 Selection of the Concentration of MWCNTs

The fabrication method has been illustrated in section 4.2, so here just the choice of MWCNTs mass fraction will be described in order to find out the most suitable concentration of MWCNTs for stretchable sensors. In this work, we prepared 5%, 7%, and 9% MWCNTs/PDMS mixture suspensions respectively.

Table 5-2 The electrical resistance of four samples in each type of MWCNTs/PDMS membranes with different concentrations of MWCNTs (5%, 7%, and 9%) as well as the average values and standard deviation of every four samples.

MWCNTs Concentration	Resistance Group A	Resistance Group B	Resistance Group C	Resistance Group D	Average Value	Standard Deviation
5%	472.53 k Ω	263.18 k Ω	1028.64 k Ω	525.19 k Ω	572.39 k Ω	324.54
7%	12.06 k Ω	18.75 k Ω	6.54 k Ω	20.36 k Ω	14.43 k Ω	6.37
9%	0.341 k Ω	0.209 k Ω	0.175 k Ω	0.264 k Ω	0.247 k Ω	0.0725

According to the contrast of sensing performance, the composite with 7% of MWCNTs is most suitable. At first, their electrical conductivities expressed by the electrical resistance were compared as shown in Table 5-2. 5% MWCNTs composite membrane exhibits poor and unstable electrical conductivity, electrical resistance ranging from 263.18 to 1028.64 k Ω , whereas the resistance of 7% fluctuates from 6.54 to 20.36 k Ω . 9% of MWCNTs nanocomposite has the most stable and excellent electrical resistance (0.175 to 0.341 k Ω). It can also be seen clearly that the standard deviations of electrical resistance

for composites with different MWCNTs concentrations produce a reduction along with the increase of the MWCNTs concentration, revealing the unstable resistance of the composites with low MWCNT concentration. The reason why the composite with lower concentration of MWCNTs exhibits unstable and poor electrical conductivity is related to the fact that it has less probability to construct conductive network^{158, 166}. In the context, without an adequate quantity of CNTs to construct conductive paths, it is mainly dependent on the network structure. Conversely, once there is a sufficient quantity of CNTs, the network structure will not play an important role. Furthermore, with more additions of CNTs, the electrical conductivity of the composite will not increase as quickly as it did initially.

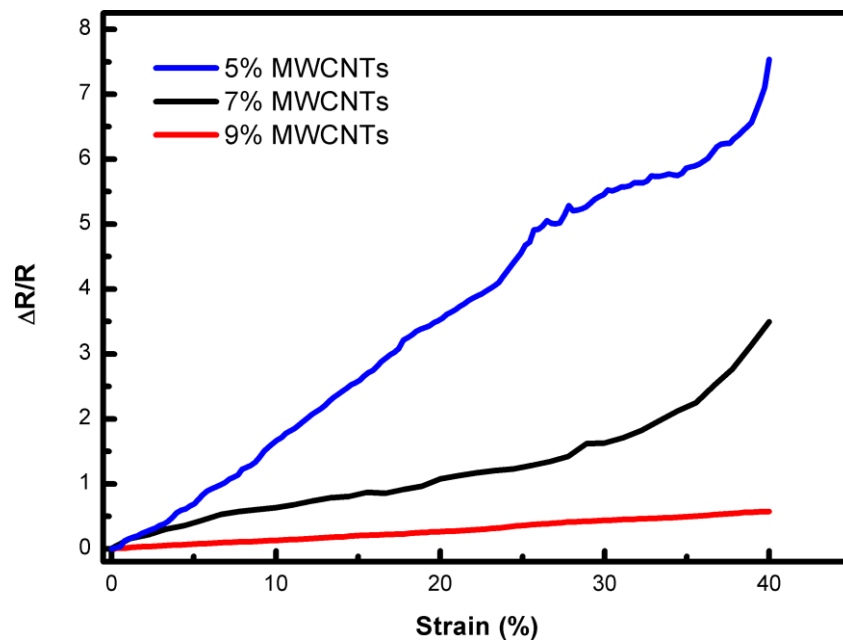


Figure 5-1 The average resistance variation of MWCNTs composite with different concentration of MWCNTs upon stretching

The sensitivity of the composites with different MWCNTS concentrations are investigated as depicted in Figure 5-1. It shows that the relative change in resistance of all the composites with different MWCNTs concentrations experiences rising when subjected to stretching, which can be ascribed to the reconstruction of the percolation

network. In fact, both the formation and separation can act at the same time over the course of stretching, which might be the reason why the relative change in resistance would increase in an oscillating pattern²⁰⁷. Additionally, when adjacent CNTs begin to separate, the tunneling resistance between them will increase, consequently resulting in raising the total resistance^{178, 208}. Among the three composites, the one containing 5% MWCNTs has the best gauge factor (GF), approximately equal to 15. However, the relationship of relative change in resistance versus strain is not close to linearity and experienced drastic wavelike rise after strain 25%. This is because a large number of the connected paths of CNTs start to break. Although a few of them recombine simultaneously, the effect of breaking is more significant. The composite with 7% MWCNTs has an approximately linear curve of the relative change in resistance against the applied strain (GF ranging from 5 to 9), while the GF of 9% MWCNTs is relatively small ($GF \approx 1$). The denser network constructed by MWCNTs leads to generating more conductive paths, avoiding drastic increases of resistance under stretching. While stretched, the electrical conductivity will not significantly decrease as long as the effective conductive paths are maintained by sufficient quantity of MWCNTs²⁰⁹. Although the sensitivity turns relatively mediocre, the sensor responds to the strain variation with outstanding linearity for the whole process (from 0% to 40%). From above, it can be found that the sensitivity of 9% MWCNTs composite sensor is not as high, and the curve of relative change in resistance versus the applied strain for 5% of MWCNTs is not linear enough. Hence, the composite incorporating 7% MWCNTs is the most suitable, which relatively has the most stable electrical conductivity, favorable sensitivity, excellent linearity and good stretchability. In addition, the microstructure of the MWCNTs/PDMS with 7% MWCNTs is observed by the SEM image to examine the dispersion state of

MWCNTs as shown in Figure 5-2c. It indicates that MWCNTs are dispersed evenly with little agglomeration so that the existence of conductive network is verified.

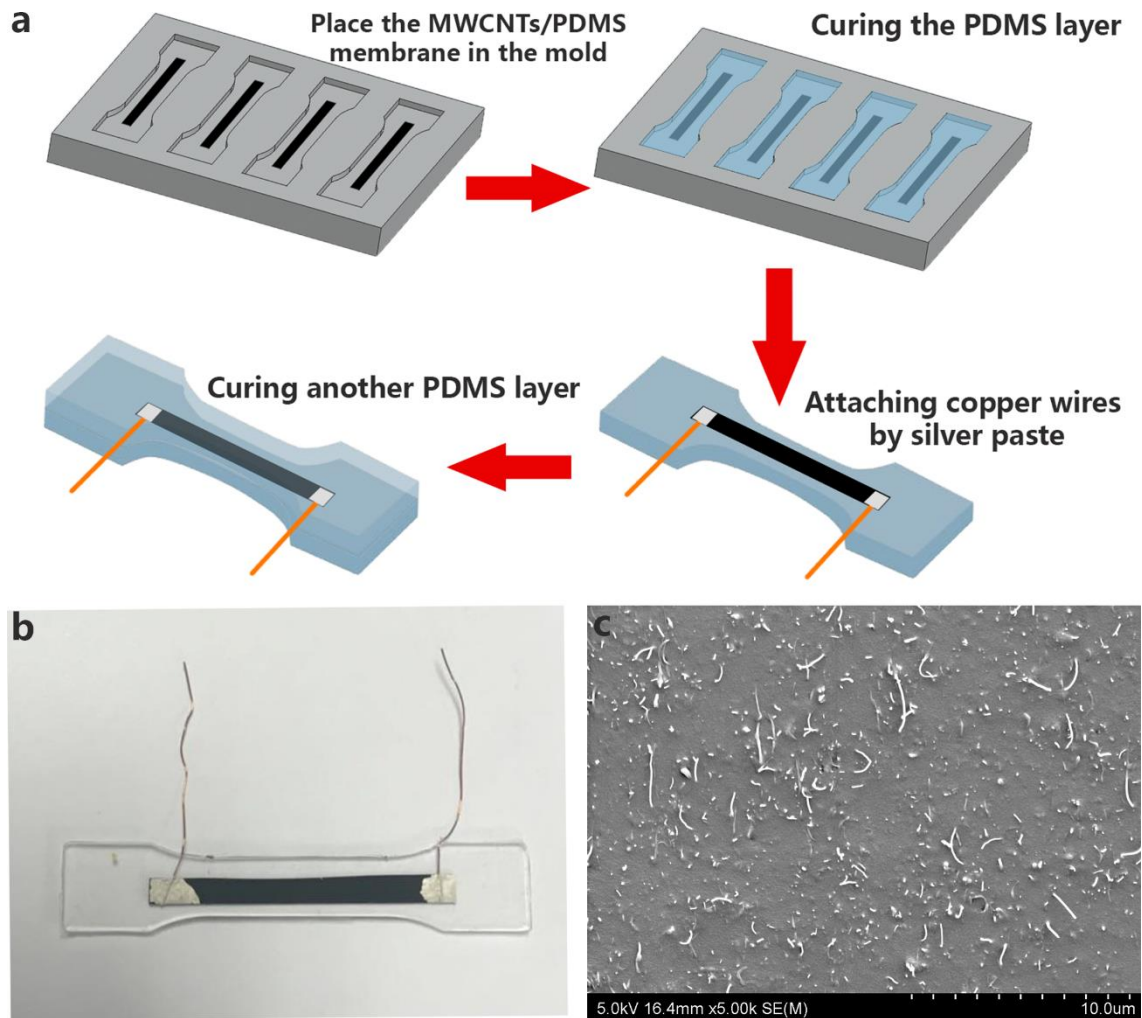


Figure 5-2 (a) Fabrication procedure of the strain sensor based on MWCNTs/PDMS composite with sandwich-like structure. (b) Photographs of the as-prepared sandwich-like strain sensor connected with copper wires. (c) The SEM image of the cross-section of the MWCNTs/PDMS composite.

5.2.3 Sensor Fabrication

Figure 5-2a depicts the procedure of making the stretchable sensor at length. The MWCNTs/PDMS membrane was cut into some sections with rectangle shapes. After placing them into the alumina mold, the mixture of PDMS prepolymer and curing agent were cast into the mold and covered the membrane. This was followed by curing at 80 °C for 2 hours. After that, the PDMS layer adhesive with the MWCNTs/PDMS layer was

peeled off from the mold due to the penetration of the liquid PDMS into the composite. Then, two copper wires were attached onto the two ends of the MWCNTs/PDMS membrane by silver paste. At last, another layer of liquid PDMS was cured on the top of the MWCNTs/PDMS layer to form a sandwich-like structure as displayed in Figure 5-2b. Thus, there are three layers in total. Top and bottom layers are PDMS whose thickness is 1mm, while the middle layer is the MWCNTs/PDMS composite layer whose thickness is 0.8 mm. Notably, due to the penetration of liquid PDMS, the top layer of PDMS can firmly combine with the other two layers. Moreover, the adhesive force between these layers induced by the penetration of PDMS is big enough to guarantee these layers can be stretched together with a large strain²¹⁰. Based on the tension test (Figure 4-5a), the Young's modulus of the MWCNTs/PDMS composite is bigger than that of the pure PDMS. Thus, the adhesive force between these layers will give a shear force to the MWCNTs/PDMS layer in order to make it stretched as long as the outer PDMS layer. Once the strain gets beyond a certain value, the adhesive force cannot sustain sufficient shear force to make the composite layer stretched and the composite layer will detach from the outer PDMS layer^{166, 210}. Due to the encapsulation of PDMS, the sensor can be directly mounted on the skins without wrinkling and plastic deformation to the middle nanocomposite membrane. The length of the conductive section of the sensor (the section between two silver pastes) is around 35mm. The stretched length and original length are measured as illustrated in Figure 5-3.

5.2.4 Sensors Characterization

The microstructure of MWCNTs/PDMS composite was observed using Scanning Electron Microscope (SEM, Hitachi SU-70). The electrical conductivity and piezoresistivity of sensors were measured using a UNI-T UT803 multimeter by a standard

two-probe method. The tension test was conducted using TA.XT plus microforce analyzer to study the hysteresis, durability, sensitivity and so on. It is worth noting that the clamps of the analyzer should clamp the two ends of the sample and cover the silver paste section to avoid the tension of silver paste as shown Figure 5-3.

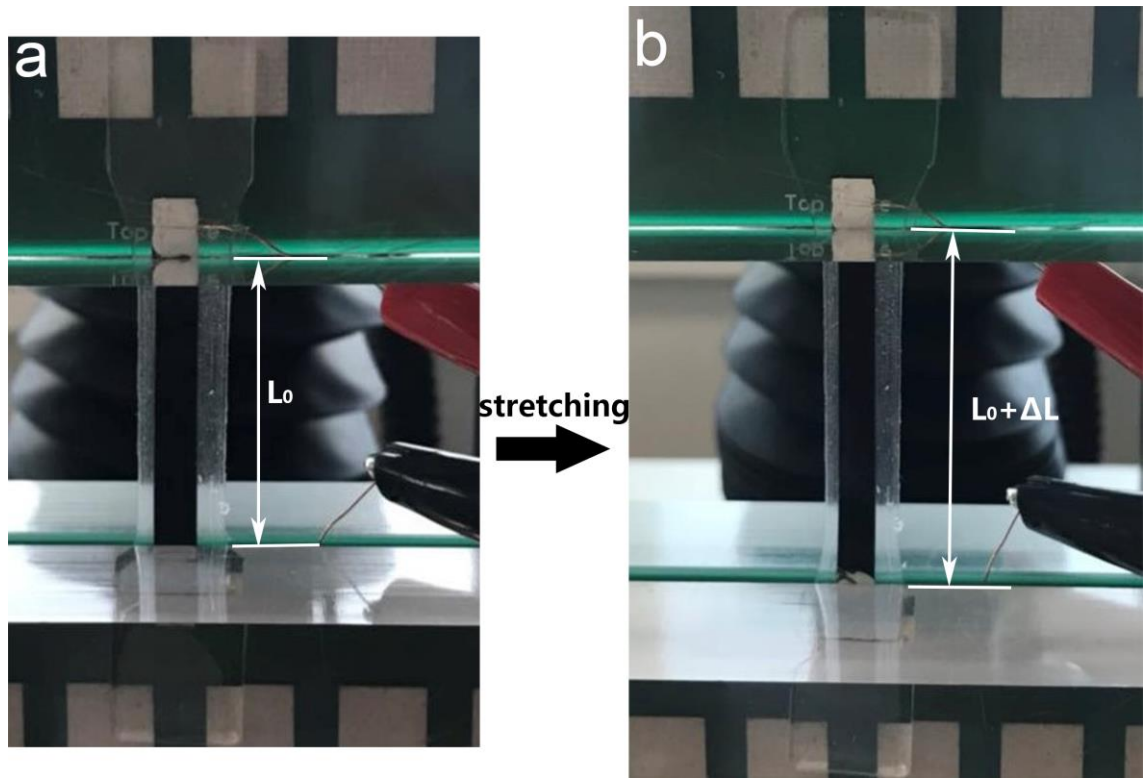


Figure 5-3 The sample are measured under the initial state (a) and stretched state (b) in the tensile test

5.3 Sensitivity and Hysteresis

As section 5.2.2 explained, the sensor with 7% MWCNTs exhibited high sensitivity with GF ranging from 5 to 9. Next, the 7% MWCNTs sensor undergoes stretching/relaxing cycle to observe the hysteresis performance. Different strains are applied (10%, 20%, and 40%) and the tension speed is set as 0.5mm/sec. The dependence of relative change in resistance and strain history is displayed in Figure 5-4a. No matter what the applied strain is, the slope of the curve of relative change in resistance against the applied strain is almost equal, which indicates that the sensor has excellent stability and linear response to

the mechanical stimuli. That is to say, the gauge factor of the sensor ranges from 5 to 9 upon stretching within strain 40%. The CNTs-based sensor made by Wang et al. possessed unstable gauge factor, which varied from 10 to 50 under strain 40%¹⁶. Besides, the graphene-based strain sensor fabricated by Park et al. only exhibited a gauge factor of around 1. Hence, this sensor has excellent sensitivity¹⁰. Furthermore, the relative change in resistance diminishes promptly and timely when the sensor starts to be released. While the sensor is being released, the trace of relative resistance variation is close and similar to that under stretching. In other words, there exists little hysteresis in this process. Here, to better know the hysteresis performance, it is quantified by a formula Eq. 5-1:

$$\gamma_H = \frac{\Delta H_{max}}{Y} \times 100\% \quad 5-1$$

Where the γ_H is the hysteresis error index, while ΔH_{max} is the maximum difference between the $\Delta R/R_0$ in the stretching and releasing cycle and Y denote the maximum full scale $\Delta R/R_0$, respectively. The hysteresis error index for 20% strain is 30.4%, whereas that for 10% strain is 16.8% and for 40% strain is 9.3%. Although the hysteresis for 20% strain is larger than the other two, the error still can be tolerable. For example, the carbon black/PDMS composite sensor fabricated by Kong et al. exhibited hysteresis error around 25% upon stretching of 10% strain¹⁵⁷. Amjadi et al. made a stretchable sensor composed of silver nanowire-elastomer nanocomposite which presented hysteresis error 30% roughly subjected to 10% strain stretching²². It is perhaps attributed to the fact that the network of CNTs would reconfigure differently in each stretching. Therefore, the hysteresis error only can be guaranteed to be under an accepted limit.

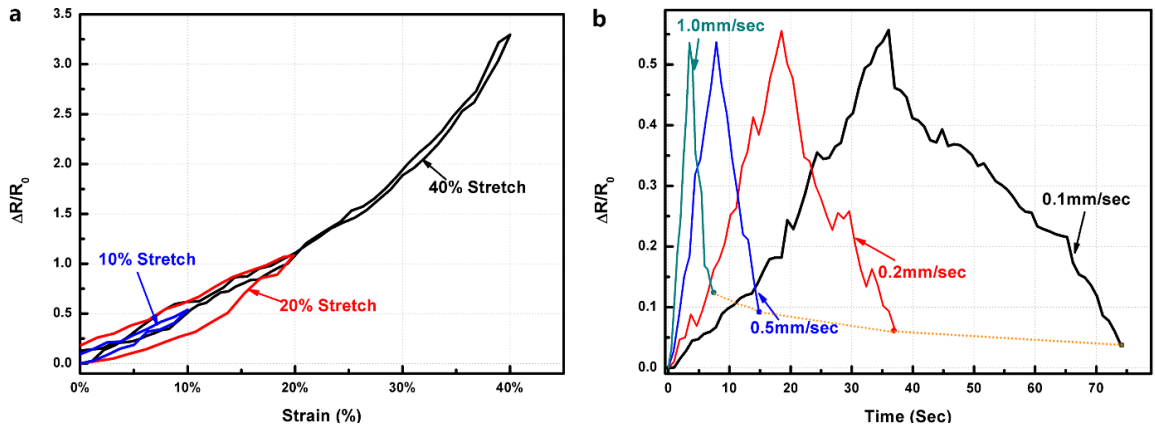


Figure 5-4 (a) the curve of relative change in resistance against the applied strain upon stretching in different strain for the sandwich-like sensor. (b) the correlation between the relative variation in resistance versus time subjected stretching of 10% strain at different tension speed.

In addition, considering that the tension speed is one of the main influential parameters on the piezoresistivity performance, herein the piezoresistive behavior of the sensor is studied at different tension speeds. The sensor is stretched up to 10% strain at different tensile speeds as illustrated in Figure 5-4b. It can be seen that not only the sensitivity remains stable, but also the curve of relative resistance change versus time maintains its linearity. In other words, the strain gauge exhibits a strain-rate independent piezoresistive response in terms of sensitivity and linearity. However, the response time is different when subject to stretching/releasing with different tensile speeds.

As shown in Figure 5-5, when the tension speed is 0.5mm/sec and 1mm/sec, the electrical resistance response will produce a slight delay, which could be observed through comparing the peaks of $\Delta R/R_0$ -Time curve and Strain-Time curve. Nevertheless, when the sample was stretched at a rate of 0.1mm/sec or 0.2mm/sec, the delay can be neglected. It might be attributed to the error caused by the resolution limit of the multimeter, or it is probably induced by the hysteresis of the PDMS^{211, 212}. Furthermore, quicker tensile speed would lead to a bigger difference between initial and ending resistance, which can be explained by the fact that the CNTs cannot go back to the balanced state promptly in

the PDMS matrix due to the presence of friction between the CNTs and PDMS^{213, 214}. That is to say, quick tensile speed does not offer sufficient time to make internal structure reaching balanced and stable status. To be specific, as the sensor is stretched the MWCNTs network structure reshapes at the same time, so the neighboring MWCNTs need time to reach the equilibrium state mutually again through the van der Waals interactions between them and the interactions between CNTs and PDMS^{31, 116, 146}.

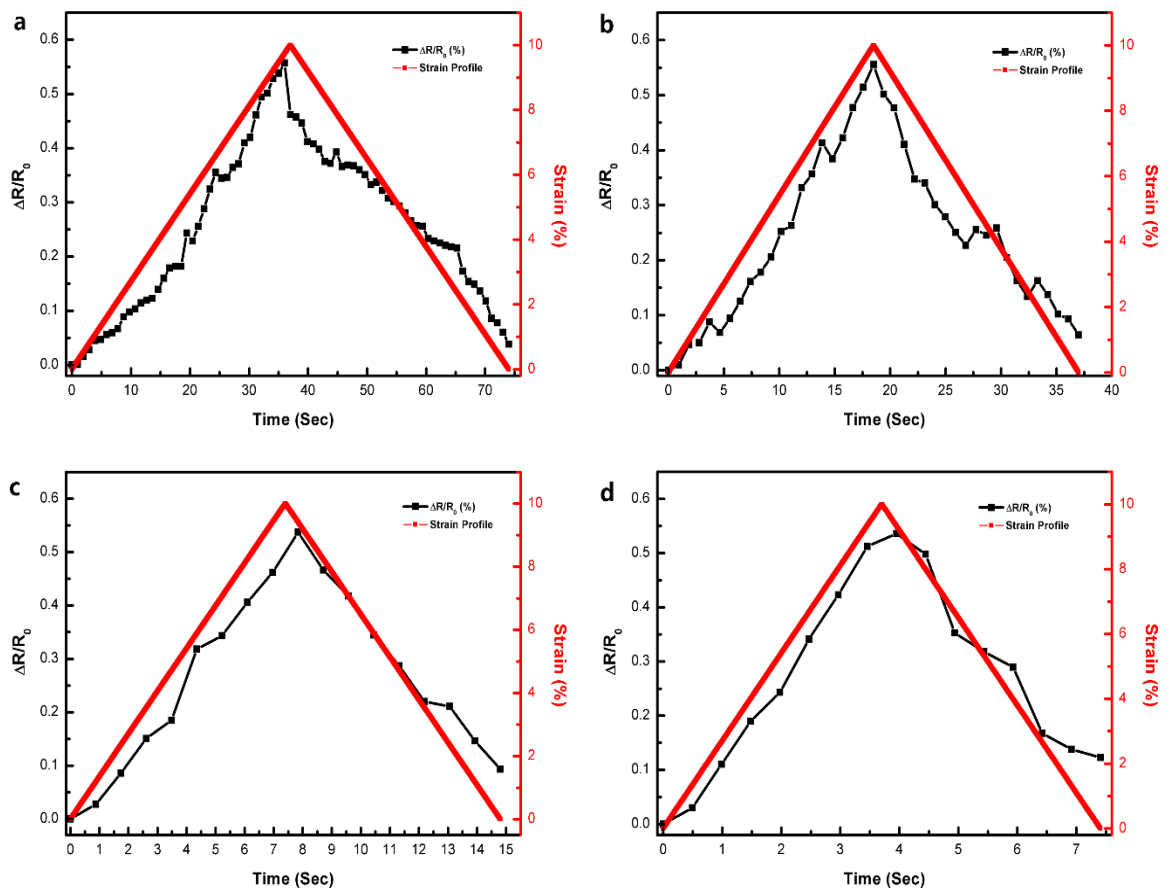


Figure 5-5 the relative change in resistance and the applied strain as a function of time at different tension rates 0.1mm/sec (A), 0.2mm/sec (B), 0.5mm/sec (C), 1mm/sec (D).

5.4 Response Time

Figure 5-6a exhibits the dynamic relative resistance change response of the sensor incorporating 7% MWCNTs to the strain variation (0-10%) under stretching/relaxing cycles at a tension rate of 1mm/sec. As indicated in the figure, the profile of the change in resistance has greatly overlapped the strain profile, manifesting that the sensor has

prompt response speed. Although the resistance after the cycle of stretching/releasing cannot go back to the initial value at once, the difference is tiny enough to neglect. In addition, the GF still reaches around 2. In contrast, the sensor is also applied on stretching and releasing with 0-20% strain at the same tension speed as illustrated in Figure 5-6b. As expected, the profile of the relative change in resistance almost precisely followed the strain variation, in spite of one remarkable phenomenon that the resistance after the first cycle of stretching/releasing cannot go back to the initial value. However, in the following cycles, not only the value of the relative change in resistance in each valley varies marginally less than 1%, but also its curve against time shows stable wave variation. This phenomenon is mainly caused by the frictions between the CNTs and PDMS²¹³. Due to the high tension strain and CNTs slippage, CNTs percolation network in the PDMS matrix upon releasing is unable to recover to the stable and balanced structure fully and promptly. Hence after the first cycle, the values of relative change in resistance in the valleys are bigger than the initial value and then stay similar. Besides, in the 10% strain stretching/releasing cycle, the resistance after every cycle can recover to the initial value approximately because the relatively small strain does not lead to the delay time of recovery. In any case, when the sensor is subjected to sequential stretching/relaxing cycles with 10% or 20% strain, it still shows a desirable consistency between resistance change and strain variation.

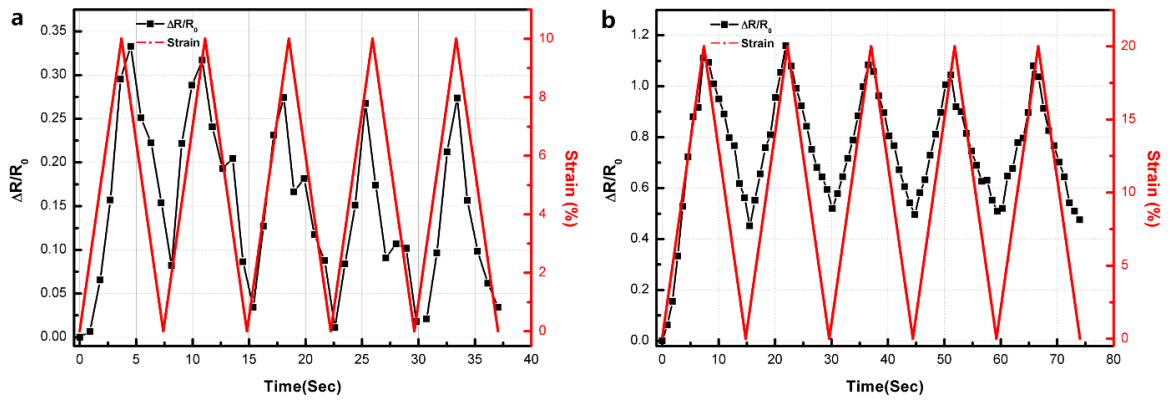


Figure 5-6 Resistance Response of the strain sensor to the cycle of stretching/releasing with 0%-10% strain variation (a) and 0-20% strain variation (b).

5.5 Durability

The durability which is an important indicator for the strain sensor represents the endurance to the long-term stretching/releasing cycles with excellent mechanical and electrical performance simultaneously. As depicted in Figure 5-7a, the strain sensor was stretched and relaxed circularly 1000 times with 10% strain at the tension speed of 1mm/sec. The bulk electrical resistance of the sensor experiences a quick drop at the initial phase, then it slightly diminishes. To the best of our knowledge, two competitive processes that are destruction and formation of conductive paths works during the stretching of composites¹¹⁶. In the region where CNTs are dispersed evenly, the conductive paths would be destroyed remarkably under stretching process. As to the region of CNTs clusters, due to the sufficient aggregation of MWCNTs, conductive channels of CNTs would not be destroyed. Instead, the clusters of MWCNTs may be separated apart gradually when the sensor is repeatedly stretched and released, resulting in the formation of more conductive paths in the MWCNTS agglomeration regions^{119, 149}. This demonstrates that the initial resistance after each cycle decreases. Moreover, with the progressive separation of CNTs agglomeration, the downtrend of resistance slows down and the resistance will approach one stable value. Besides, the CNTs would become

aligned in stretching direction after a series of stretching/releasing²¹⁵. As a consequence, this may help to improve the electrical conductivity along the stretching direction, but the sensitivity may be deteriorated^{164, 216}. Furthermore, after a large number of stretching/releasing, the sensor still exhibits the stable sensitivity and quick response time when subjected to strain variation, which can be seen in the detailed view of the red circle part (Figure 5-7b).

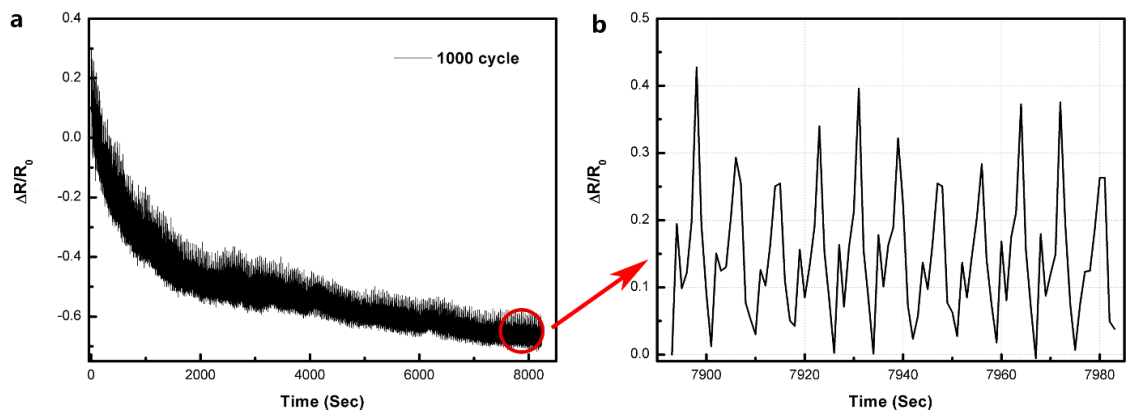
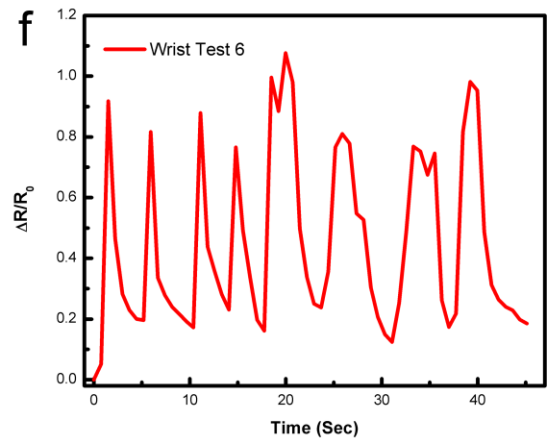
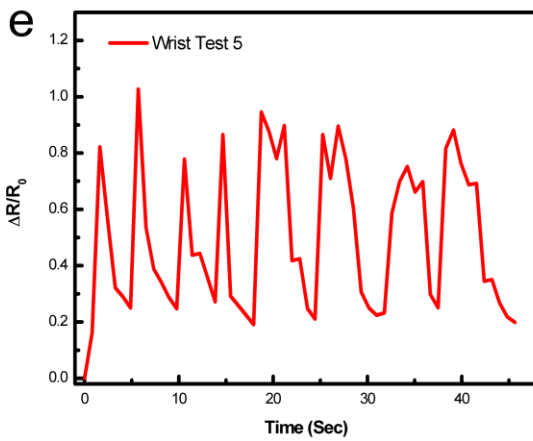
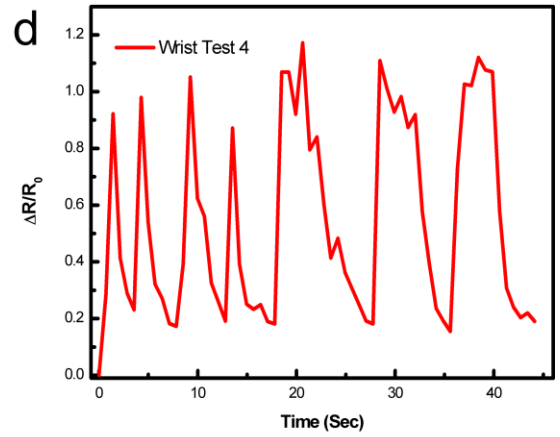
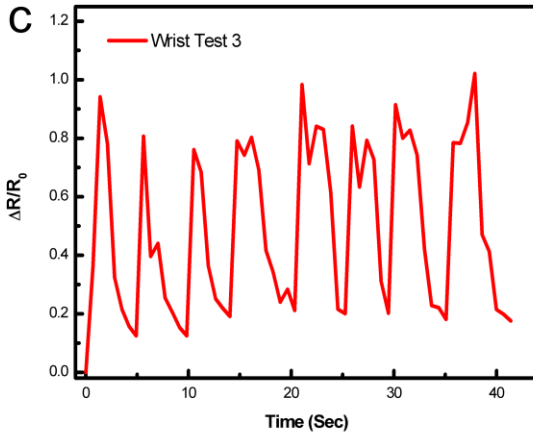
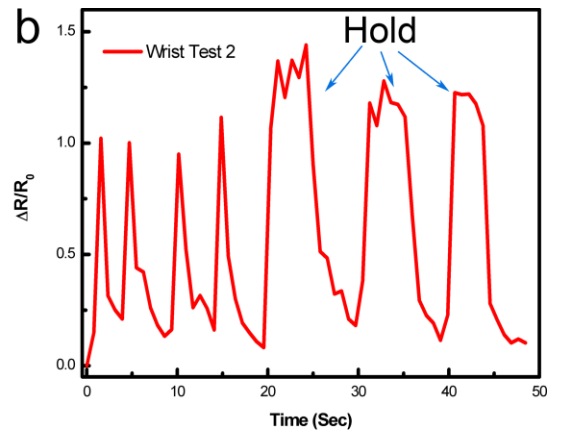
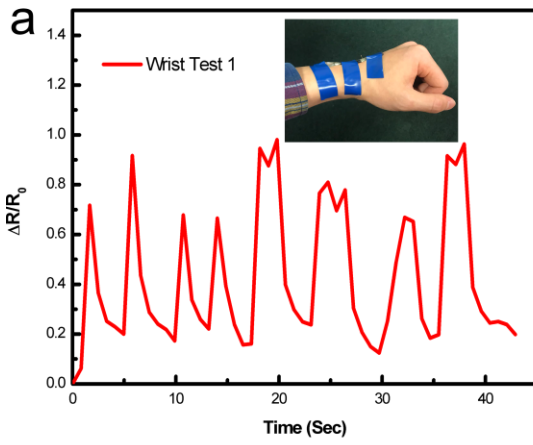


Figure 5-7 (a) the long-term relative variation in resistance of the strain sensor when subjected to the 1000 cycles of stretching/releasing (from 0% to 10% strain). (b) the relative change in resistance of the strain sensor magnified from the red circle part in (a).

After a series of characterization, the sensor proves that it has a desirable overall performance. It not only exhibits favorable sensitivity, low hysteresis, and quick response but also can adapt to different tension speeds and guarantee sufficient longevity. Lastly, the as-prepared strain sensor was employment for detecting the human motions to observe whether it can be eligible for these tasks or not.

5.6 Human Motions Detection

The as-fabricated sensors are also put into practical use in IBTec, Auckland, New Zealand. The deformation of the majority of human motions, such as wrist and finger bending, typically would not give rise to strain exceeding 40%¹³. Figure 5-8 shows the relative change in resistance when subjected to wrist bending.



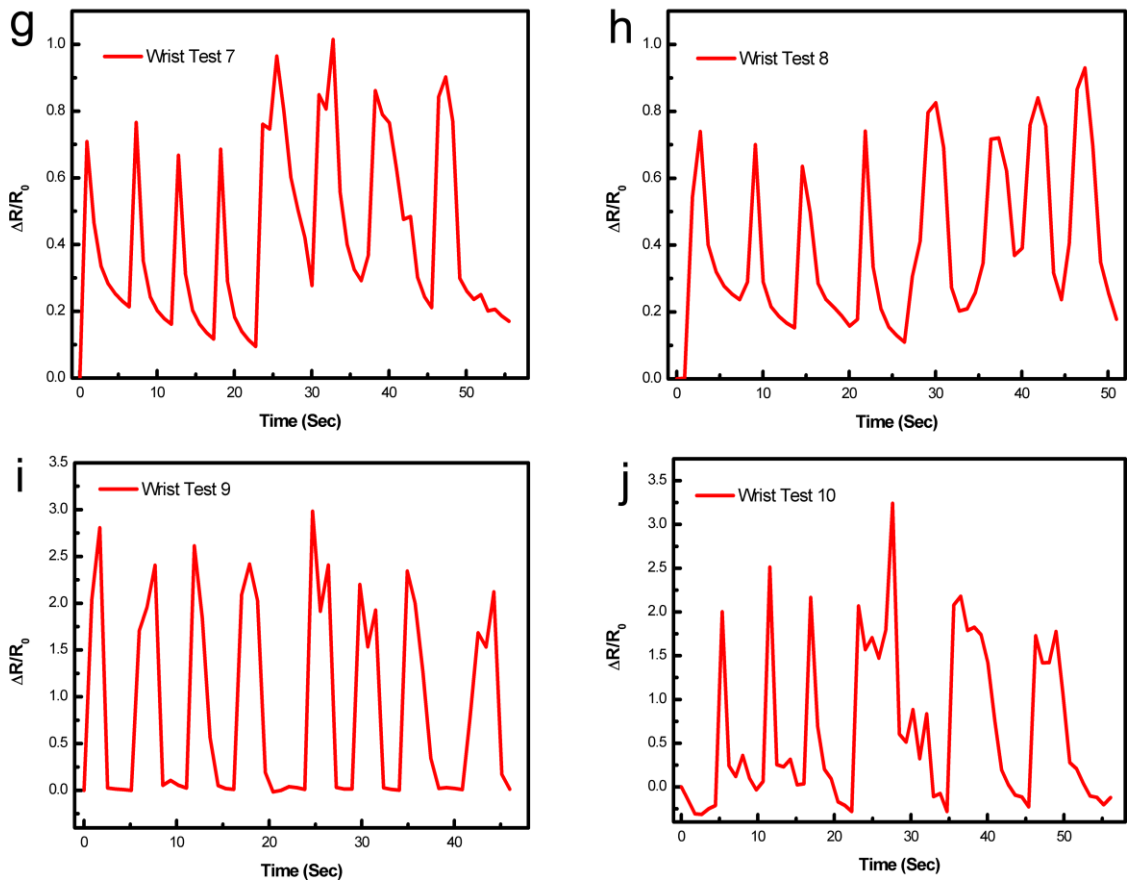
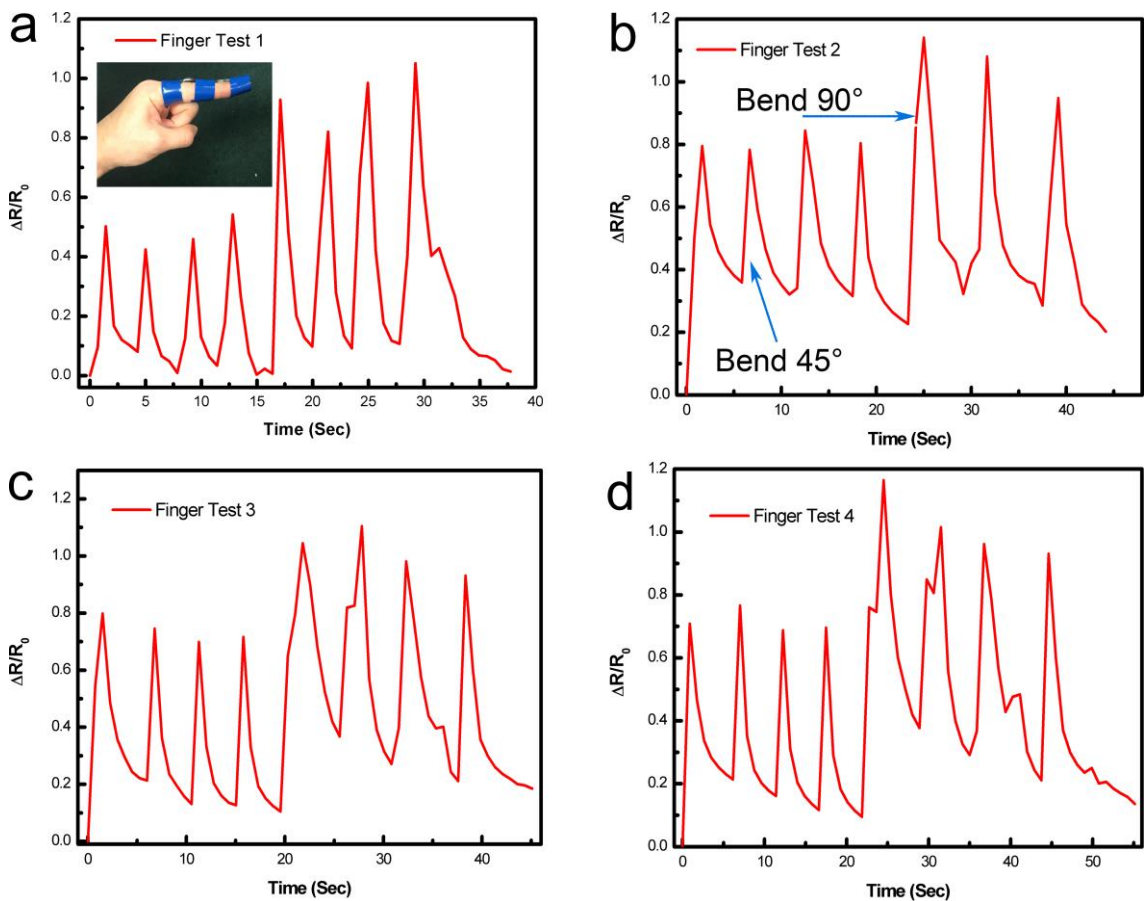


Figure 5-8. (a) to (j) the curves of relative change in resistance versus time for the strain sensor when subjected to wrist bending from ten volunteers.

As shown in Figure 5-8a, the sensor is mounted on the wrist skin with insulating tape. There are ten volunteers who participated in this human motions test. It can be found from Figure 5-8a to 5-8j that the maximum values of relative variation in resistance lie in the range from 0.7 to 3. The participants were asked to hold the wrist bending for seconds. It can be clearly seen in Figure 5-8 that the relative variation in resistance remained a high stable value for a while when participants kept wrist bending state. This phenomenon provided evidence that the sensor possesses high sensitivity and prompt response speed.

Besides, the finger bending was detected by two different motions, bending/relaxing with an angle around 45 degrees and bending/relaxing with a 90-degree angle. The sensor was attached on the finger with insulating tape as displayed in Figure 5-9a. Similarly, ten

volunteers participated in this test of bending finger. The data of resistance change following fingers bending were recorded and exhibited in Figure 5-9a to 5-9j. It can be found that the relative change in resistance fluctuated in the range from 0.4 to 0.7 when finger bending angles were around 45 degrees. In contrast, when fingers bending with an angle of 90 degrees, it shows a higher value of the relative change in resistance, twice or more than that of bending fingers with 45 degrees. This demonstrates that this sensor can be applied to monitor human motions with different deformation extent. Also, according to the results of the practical test, it provides evidence that the sensor possesses high sensitivity and prompt response speed.



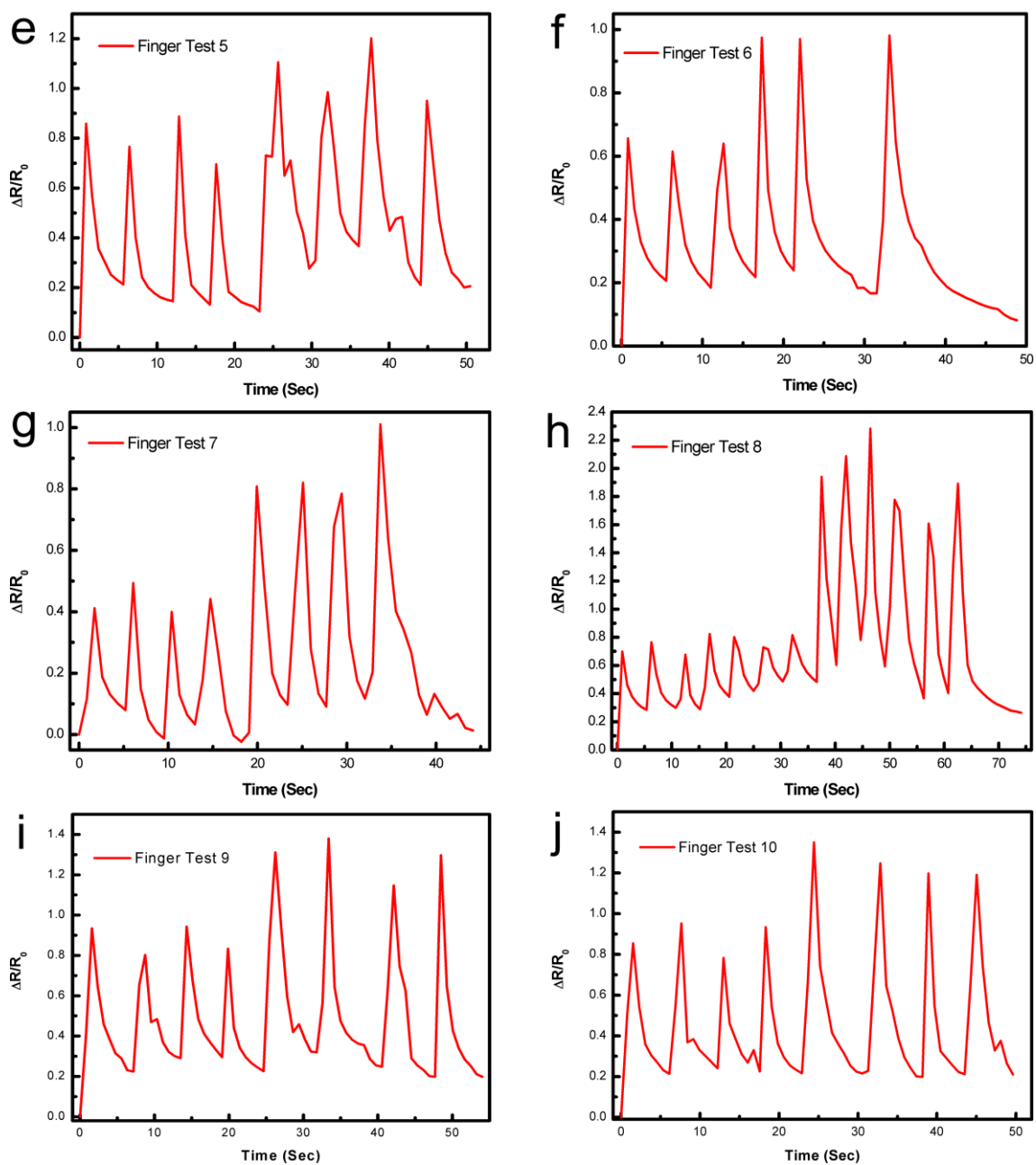


Figure 5-9 (a) to (j) the curves of relative change in resistance versus time for the strain sensor when subjected to finger bending from ten volunteers.

5.7 Conclusion

In this chapter, it is described that the stretchable MWCNTs/PDMS composite was manufactured through a facile and effective approach and then encapsulated by PDMS with sandwich-like structure. After comparison and analysis, the composite containing 7% MWCNTs is the most suitable for making the stretchable sensor. Also, it can be seen that

MWCNTs is dispersed fairly uniformly in the PDMS matrix by observing SEM images. The as-prepared strain sensor not only exhibits high stretchability which was able to be stretched as high as 40% of its original length, but also it shows high sensitivity (GF ranging from 5-9). In addition, the sensor can respond immediately and precisely when subjected to a succession of stretching/releasing cycles with low hysteresis. Furthermore, the strain sensor still performs well after 1000 stretching/releasing cycles, demonstrating favorable durability. In the end, the practical employment of the strain is verified by the fact that the sensors can detect wrist bending precisely and promptly as well as the distinguishing between two finger bending motions. Considering these advantages of the strain sensor, it is trustworthy that both the sensor and the composite have potentials to be utilized in various fields, including wearable devices, biomedical detectors and so forth.

Chapter 6 Fabrication and Characterization of the Serpentine

Sensor

6.1 Introduction

Although the stretchable sandwich-like sensor based on rectangular MWCNTs/PDMS composite has exhibited favorable performance, there is still much room for promotion in terms of the linearity of response to strain and hysteresis performance. In addition, it is common that conventional sensors merely based on the conductive polymer composite suffer from some drawbacks. That is, it is hard for these sensors to do well in all aspects of sensing performance. For instance, Tadakaluru et al. fabricated a stretchable strain sensor based on multi-wall CNTs (MWCNTs) and rubber. Although it showed high sensitivity and stretchability, the nonlinear response to strain was still a negative point^{19, 217}.

Besides, for the advanced application, like electronic skin, soft robot and smart textile, the multifunction of stretchable sensors nearly has been the basic requirement. Consequently, the demand for multifunctional sensors increased^{146, 218}. Rahimi developed a stretchable sensor that could differentiate between the longitudinal and transverse strains. The conductive carbon nanomaterials were created and patterned by direct laser-pyrolyzation of a polyimide tape, resulting in highly porous carbon line traces simultaneously¹⁴⁷. Then the patterned carbon nanomaterial was encapsulated in the polydimethylsiloxane (PDMS). Due to the shape of the carbon nanomaterial structure, the sensors would respond with different resistance variations when subjected to longitudinal and transverse strains. Accordingly, here the serpentine sensor is devised and fabricated, managing to resolve and improve these bottlenecks.

In this chapter, the serpentine sensor was fabricated via a facile molding technique similar to the method described in chapter 5. The stretchable sensor is made of MWCNTs/PDMS nanocomposite with a serpentine shape which is encapsulated in the insulating PDMS matrix. The sensor was characterized to observe sensing performance, like hysteresis, sensitivity, response time and linearity. Also, it is found that the sensors can differentiate the strains in longitudinal and transverse directions. Meanwhile, finite element models (FEM) are built to investigate the strain and stress variation of the MWCNTs/PDMS composite with serpentine shapes when subjected to stretching. The as-fabricated sensor here shows great potential for future applications in the field of electronic skins.

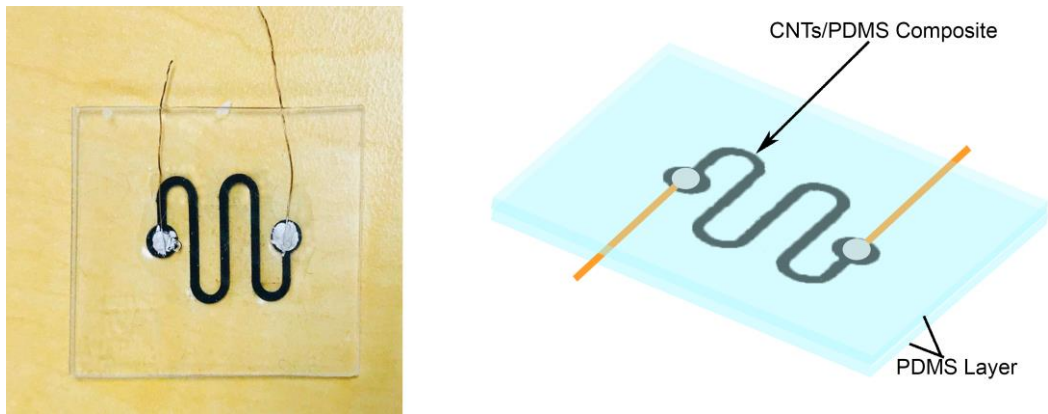


Figure 6-1 (a) Stretchable Sensor with serpentine MWCNTs/PDMS composite encapsulated by PDMS. (b) Schematic illustration of the structure of the stretchable sensor.

6.2 Experimental Investigation

6.2.1 Design of the Sensor

The stretchable serpentine sensor is comprised of three parts. The MWCNTs/PDMS composite with serpentine shape is encapsulated in the PDMS matrix as shown in Figure 6-1. Notably, the serpentine MWCNTs/PDMS composite is manufactured via a molding technique. The dimension data of serpentine shape is described in Figure 6-2. d_l is the length of the linear part designed to be 10 mm and r is the radius of the semi-circle (3

mm), while w is the width of the MWCNTs/PDMS composite, equal to 1 mm. To attach the copper wire onto the serpentine composite using silver paste, the area of two ends of the serpentine composite are enlarged and designed with circular shapes. The thickness of the serpentine shape is 0.8 mm.

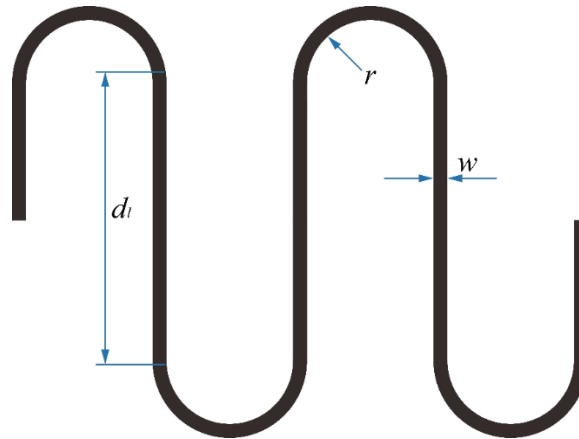


Figure 6-2 The schematic of the serpentine shape design

6.2.2 Materials

MWCNTs were provided by Graphene Supermarket Company. The diameters of MWCNTs range from 50-85 nm and their lengths lie in the scope from 10 to 15 μm . The pentane used as a solvent was supplied by Sigma Aldrich, while the PDMS and its curing agent were purchased from Dow Corning Company (Sylgard 184).

6.2.3 Sensor Fabrication and Characterization

The fabrication procedure of MWCNTs/PDMS suspension has been described in section 4.2. Here the whole process of the serpentine sensor is illustrated. Its procedure schematic is illustrated in Figure 6-3a. Having MWCNTs/PDMS mixture suspension prepared, the mixture was cast into the aluminum mold with serpentine shapes. Next, the bubbles in the mixture should be removed in the vacuum state. After that, the mixture can be cured at 80 $^{\circ}\text{C}$ for 2 hours in a vacuum oven. After curing, the PDMS pre-polymer was poured on

the serpentine composite to form a PDMS layer. After two hours for curing, the PDMS layer adhered to the serpentine MWCNTs/PDMS composite and could be peeled off together from the mold. This is ascribed to the penetration of the liquid PDMS into the composite as shown in Figure 6-3c. The thickness of the PDMS layer is 0.8 mm. Two copper wires were then attached to the two circular ends of the serpentine MWCNTs/PDMS composite by silver paste. Finally, another thin layer of liquid PDMS was cured to encapsulate the MWCNTs/PDMS composite, forming a sandwich-like structure.

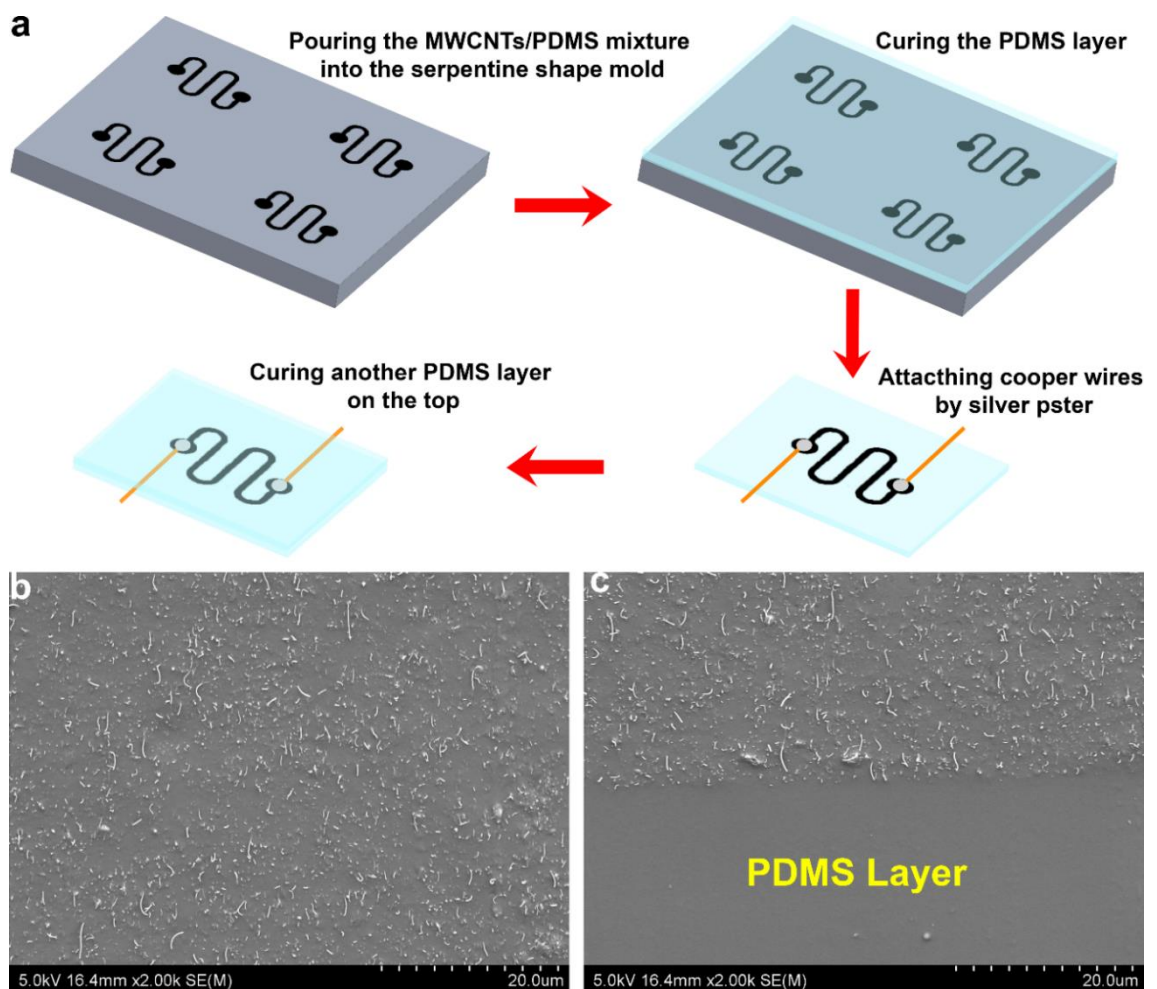


Figure 6-3 (a) Fabrication procedure of the stretchable strain sensor based on serpentine MWCNTs/PDMS composite via molding technique. (b) The SEM image of the cross-section of the serpentine MWCNTs/PDMS composite. (c) The Cross-sectional SEM image of the stretchable sensor in the interaction zone between MWCNTs/PDMS composite layer and the PDMS layer.

Firstly, the microstructure of the serpentine sensor was observed using Scanning Electron Microscope (SEM, Hitachi SU-70). Both the fraction surface of the MWCNTs/PDMS composite and the interface between the MWCNTs/PDMS composite layer and PDMS layer were captured to be analyzed as shown in Figures 6-3b and 6-3c. The electrical conductivity and piezoresistivity of the sensor were measured using a UNI-T UT803 multimeter by a standard two-probe method. The repetitive tension tests were carried out using TA.XT plus microforce analyzer to investigate the performance of sensitivity, response time, hysteresis and so forth.

6.3 Characterization Results

It can be clearly seen in Figure 6-3b that the MWCNTs are homogeneously dispersed in the PDMS matrix without voids. The excellent dispersion state of MWCNTs reflects that the electrically conductive network is well created so that the electrical and mechanical properties of the composite would be strengthened as much as possible. The electrical resistance data for all the serpentine MWCNTs/PDMS composites samples are listed in Table 6-1. Their average value of resistance is 607.3K Ω .

Table 6-1 The initial measured resistance of three serpentine sensors based on the MWCNTs/PDMS composite with 7% MWCNTs as well as the average value of the three sensors.

MWCNTs Concentration	Resistance Group A	Resistance Group B	Resistance Group C	Average Value
7%	615 k Ω	595 k Ω	612 k Ω	607.3 k Ω

In addition, Figure 6-3c exhibits the interface between the PDMS layer and the MWCNTs/PDMS composite layer. The interface is fairly smooth without any obvious detachment. This is ascribed to the penetration of liquid PDMS into the cured

MWCNTs/PDMS composite layer in the manufacturing process. Thus, there is a strong binding between these two layers.

6.3.1 Sensitivity

When the sample is undergoing tensile force in the transverse or longitudinal direction as displayed in Figure 6-4a, due to the special serpentine shape, the resistance variation subject to these two different strains theoretically would be different. As a result, the sensitivities of the stretchable sensor for tension in a different direction would also have a big difference. The sensitivity can be expressed by Gauge Factor (GF) as described in Eq. 3-15. It can be seen in Figure 6-4b that the relative change in resistance against transverse strain responds linearly, while the relative change in resistance subjected to longitudinal stretching exhibits a wavelike rise. Meanwhile, the GF under longitudinal stretching is better than that subjected to transverse tension. In addition, the rectangular CNTs/PDMS composite sample was implemented with a tensile test in chapter 5 (blue dash line in Figure 6-4b). It can be clearly seen that the blue curve of average relative resistance change against strain is nonlinear and the GF (around 5.5 to 6) is fairly larger than those of the serpentine samples subjected to both transverse (red dot line) and longitudinal stretching (black cube line). It can be explained by the fact that the serpentine shape of the sample somewhat alleviates the CNTs/PDMS composite deformation regardless of the stretching direction so that the conductive network of CNTs in the PDMS matrix will be slightly destroyed, resulting in mild resistance increase. Notably, linearity is an important parameter for a stretchable sensor. Nonlinearity of sensors makes the calibration process complex and difficult^{219, 220}. Resistive-type sensors usually exhibit bad linearity, which is viewed as the common drawback²²¹. This serpentine sensor overcomes this drawback to some extent.

Table 6-2 The experimental data of the MWCNTs/PDMS composite and PDMS for the FEM simulation

Material	Young's Modulus	Poisson's Ratio	Density
MWCNTs/PDMS composite	5MPa	0.4	1.1338 g/cm ³
PDMS	2MPa	0.45	0.97 g/cm ³

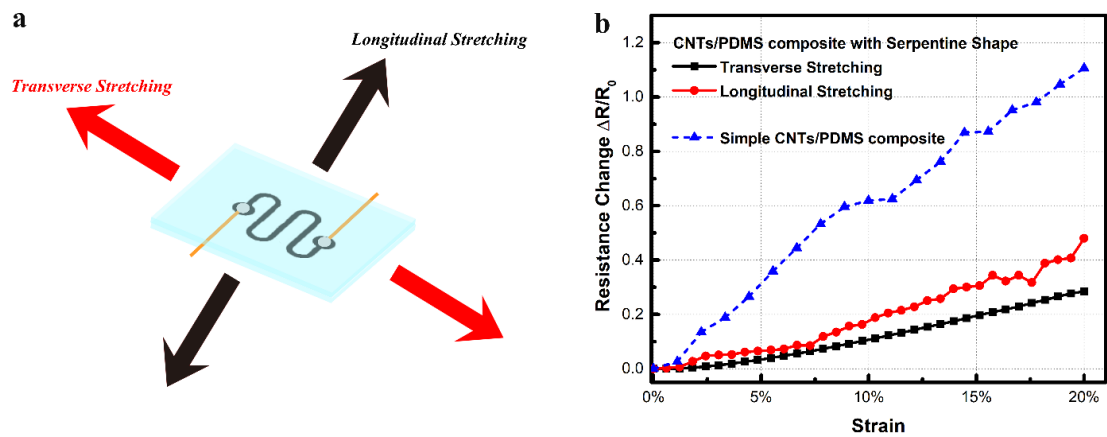


Figure 6-4 (a) The schematic of the stretchable sensor applied with tensile strain along the transverse direction or the longitudinal direction. (b) The curve of average relative change in resistance against the applied tensile strain in transverse and longitudinal direction for the serpentine stretchable sensor as well as the curve for the rectangular stretchable sensor.

Furthermore, the finite element model (FEM) of the serpentine CNTs/PDMS composite was built in order to reveal the underlying physics of deformation. According to the mechanical parameter of materials from our previous studies or other literature (refer to Table 6-2), the FEM was built and the interaction between these two material surfaces was set with tie constraint to ensure that there was no relative motion between them^{222, 223}. In fact, if the sample suffered from severe tension deformation (strain up to 50%), these two surfaces would inevitably experience a slight slide³⁶. However, the FEM here was supposed to be subjected to only 20% strain because the silver paste would start to detach from the CNTs/PDMS composite in an actual tension test. One side of the FEM is fixed and the other side was exposed to tensile force as shown in Figure 6-5a. Thus, the

FEM applied transverse and longitudinal uniform strain of 20% (ϵ_x and ϵ_y) respectively. The results displayed in Figures 6-5c and 6-5d reveal that while the whole model suffered from 20% transverse strain, the serpentine composite does not yield so much strain. As shown in the contour plot (Figure 6-5c), the maximum strain in the arc parts is only up to 8.6%, while the linear parts accommodate approximately 5.7% strain. For the model exposed to 20% longitudinal strain, linear parts yield 10% strain, which is still smaller than the whole strain 20% of the model as shown in Figure 6-5b. The strain variation of the serpentine composite indirectly reflects why the GF of the MWCNTs/CNTs composite with serpentine shape experiences a significant drop compared to that of the rectangular composite.

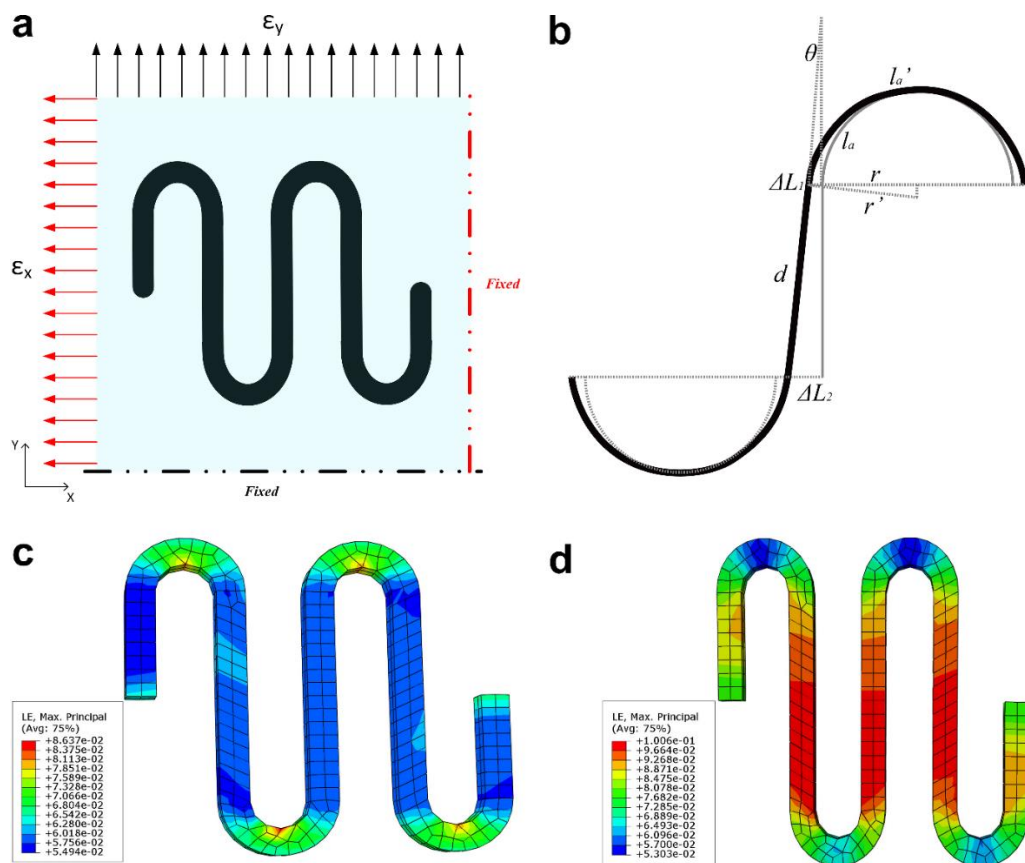


Figure 6-5 (a) The schematic of the FEM model applied with transverse or longitudinal strain. (b) Illustration of the part of serpentine shapes stretched along the transverse direction for analytical calculation. (c) Contour plot of the transverse strain in the MWCNTs/PDMS composite. (d) Contour plot of the longitudinal strain in the MWCNTs/PDMS composite.

To better understand it, a simple analytical model is created to capture this physics as shown in Figure 6-5b. The deformation of the serpentine sensor under transverse stretching consists of structural change and the deformation of the CNTs/PDMS composite. It is firstly assumed that the arc parts were stretched along the transverse direction without rotation due to the actual tension strain not being large (20%). The linear parts would thus be in fact slightly stretched in length assuming that the rotation of the arc parts did not happen. However, thanks to the deformation of arc parts and tiny tension strain applied to the model, the length of the linear part can be viewed as the original length. In addition, based on the FEM in Figure 6-5c, the linear parts yet yield deformation (the average strain is around 5.756%). This deformation can be attributed to the tension in width. Therefore, the deformation of the serpentine structure can be divided into two parts: stretching of the arc length of the arc parts and the tension of the width of the linear parts. Hence, based on the designed serpentine structure, the equation can be written out as Eq. 6-. s_w denotes the width strain (5.756%) and w is the width of the linear parts (1 mm, see Figure 6-2). Also, ΔL_1 and ΔL_2 are the stretched lengths induced by the serpentine structure, while ΔL is the difference between the initial length of the serpentine structure and the stretched length, which is equal to the product of the 20% strain and the initial length of the serpentine structure (17 mm).

$$\Delta L = 4 * (\Delta L_1 + \Delta L_2) + 5 * w * s_w \quad 6-1$$

According to geometrical information in the schematic, some equations can be listed to acquire the deformed geometrical parameters as follows:

$$\Delta L_2 - \Delta L_1 = d_l * \sin\theta_a \quad 6-2$$

$$r' * \cos\theta_a = r + \Delta L_1 \quad 6-3$$

$$r' * \sin\theta_a = r - \Delta L_1 \quad 6-4$$

Where d_l is the length of the linear parts and θ_a is the angle of the stretched arc part. r and r' are the radius of the initial arc part and the stretched arc part, respectively. Notably, r and d_l are known based on the dimensional schematic of the serpentine structure (see Figure 6-2). Accordingly, r' can be figured out, approximately equal to 1.595, while θ approaches 3.41° .

$$l_a = \pi * r \quad 6-5$$

$$l'_a = r' * (\pi - 2 * \theta_a) \quad 6-6$$

$$\Delta l_a = l'_a - l_a \quad 6-7$$

Then the difference between the initial arc length of the arc part l_a and the stretched one l'_a can be acquired by Eq. 6-5, Eq. 6-6, and Eq. 6-7. The resistance of the serpentine structure can be envisioned as the series resistance composed of arc parts and linear parts. Based on our previous studies, the curve of relative change in resistance versus strain for the rectangular MWCNTs/PDMS composite was fitted with the polynomial equation (Eq. 6-10) as shown in Figure 6-6a. Here, this fitted equation is employed to evaluate the relative change in resistance of the serpentine structure through obtained strains using the following equations.

$$L_w = 4 * (d_l + l_a) \quad 6-8$$

$$f_l = \frac{4*d_l}{L_w}, f_a = \frac{4*l_a}{L_w} \quad 6-9$$

$$\Delta R_r = f_l * (a_1 * s_w + a_2 * s_w^2 + a_3 * s_w^3 + a_4 * s_w^4) + f_a * \left(a_1 * \frac{\Delta l_a}{l_a} + a_2 * \left(\frac{\Delta l_a}{l_a} \right)^2 + a_3 * \left(\frac{\Delta l_a}{l_a} \right)^3 + a_4 * \left(\frac{\Delta l_a}{l_a} \right)^4 \right) \quad 6-10$$

Where L_w is the total actual length of the serpentine structure, while f_l and f_a are the proportion of the linear parts and arc parts to the total actual length, respectively. a_1, a_2, a_3 and a_4 are the coefficients of the polynomial equation, which are worked out by the fitting process, and ΔR_r is the relative change in resistance of the serpentine structure. As a result, the relative variation in resistance for the whole serpentine structure has been estimated.

$$GF = \Delta R_r / s$$

6-11

At last, the GF can be calculated analytically by the Eq. 6-11, where s denotes the total strain of the serpentine structure (20%). After calculation, GF is approximately equal to 1.51, in excellent consistency with the measured value of 1.53 as displayed in Figure 6-6b. It should be noticed that the gauge factor (slope of the curve) before strain 3% is obviously less than that after strain 3%. This is mainly because the serpentine structure of the sensor bears the majority of deformation instead of the CNTs/PDMS composites.

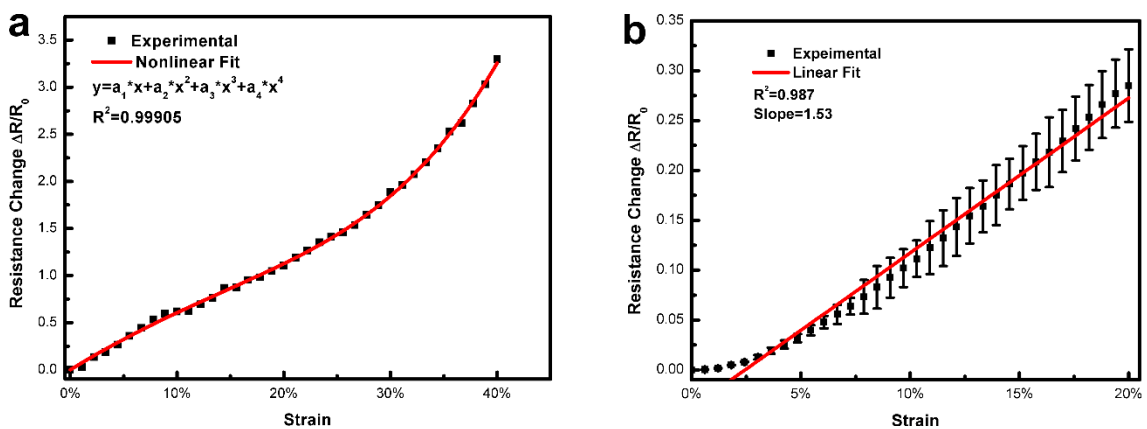


Figure 6-6 (a) The average relative variation in resistance for the sensor based on rectangular MWCNTs/PDMS composite applied with tension deformation as well as its polynomial fitted curve. (b) The average relative variation in resistance for the sensor based on serpentine MWCNTs/PDMS composite applied with transverse tension deformation as well as its linear fitted curve

6.3.2 Response time

Although the resistance responses to the transverse and longitudinal strain are different, the difference may not be obvious to guarantee that it is capable of differentiating any tension strain from a different direction in practical application. Thus, at present, the sensor is mainly viewed as the uniaxial strain sensor. However, the serpentine structure really helps to improve the linearity of the resistance response to tensile strain. Besides the sensing linearity, the response time performance of the sensor subjected to the strain is also taken into consideration.

To investigate the response speed performance of the serpentine sensor, it was repeatedly stretched up to 10% and 20% strain at a tension rate of 0.2 mm/sec, respectively. Figures 6-7a and 6-7b record both relative variation in resistance ($\Delta R/R_0$) and the strain variation of the serpentine sensor when subjected to the tensile strain of 10% and 20%, respectively. It can be found that the profile of the relative variation in resistance has an outstanding synchronization with that of the strain, revealing that the serpentine sensor possesses prompt response speed subjected to strain variation. Compared to the sensor based on rectangular MWCNTs/PDMS composite shown in Figure 5-6, the synchronization of relative change in resistance with the strain for the serpentine sensor is slightly better which can be observed in the synchronization of the valleys between the two curves of resistance change and strain (Figure 6-7). It can be explained by the fact that the MWCNTs/PDMS composite is only exposed to a relatively smaller tension strain due to the serpentine shape. Hence, the influence of the intrinsic hysteresis of the PDMS could be diminished^{213, 214}. With regards to the 20% strain stretching/releasing cycles, the profile of the relative change in resistance still keeps excellent synchronization with the strain variation. Therefore, when the serpentine sensors are subjected to repetitive stretching/releasing cycles with strain up to 20%, it performed better in terms of response speed to the strain variation than the conventional rectangular one.

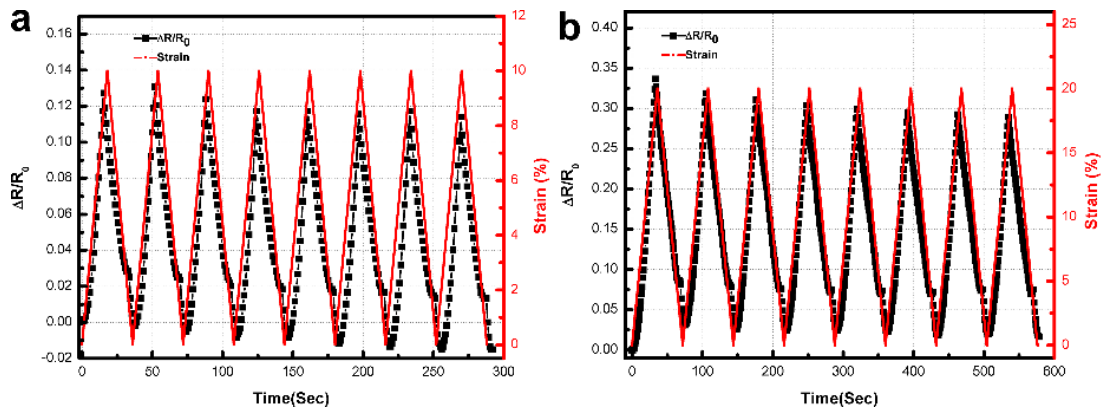


Figure 6-7 The relative change in Resistance of the serpentine sensor subjected to the cycle of stretching/releasing with 0%-10% strain variation (a) and 0%-20% strain variation (b).

6.3.3 Hysteresis

Figure 6-8a presents the hysteresis performance of the serpentine sensor under different applied transverse strains respectively (10% and 20%) with a tension rate of 0.2 mm/sec. As the figure illustrates, the electrical resistance of the serpentine sensor could not fully recover after complete releasing but the gap between the initial and final resistance is not fairly large. To better compare the hysteresis performance, the hysteresis index was worked out by a formula Eq. 5-1 in section 5.3.1. Therefore, when the sensor undergoes 20% and 10% strain respectively, both of hysteresis performances are similar. In general, when subjected to large tension strain, MWCNTs in the PDMS matrix will seriously slide so that more time is needed for the MWCNTs to recover to the initial positions. This is mainly attributed to the friction force between the MWCNTs and PDMS matrix²²⁴. Ideally, without consideration of the friction force, the MWCNTs would slide back to the initial positions smoothly and immediately. However, if the friction force existed, MWCNTs had to spend time overcoming this force, leading to the resistance hysteresis. In addition, fracture and buckling of MWCNTs would be emerged along with the stretching, which is another factor to the resistance hysteresis^{22, 225}. In this result that the hysteresis performances of the sensor subjected to different strains are close, it manifests

that when this sensor subjected to the strain under 20%, fracture extent and slide distance of MWCNTs in the polymer matrix are at the same level of magnitude.

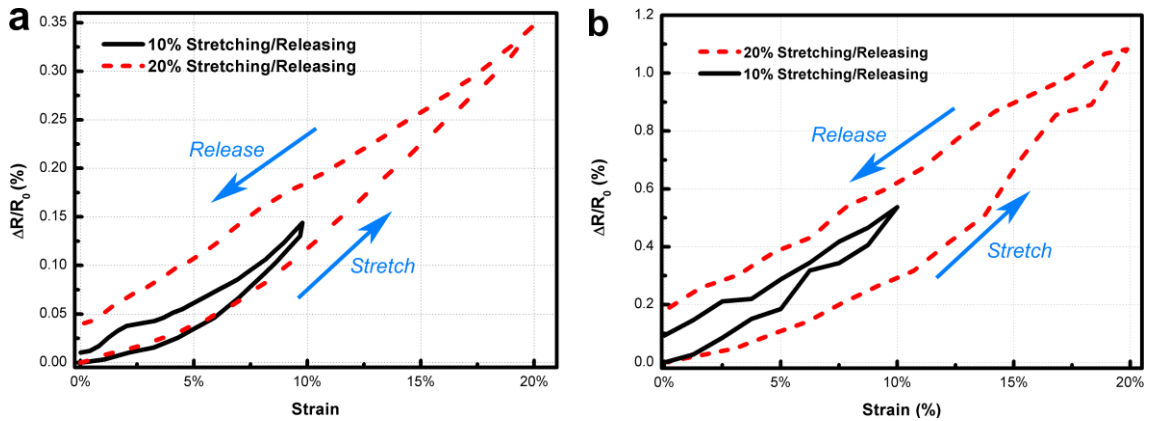


Figure 6-8 (a) The relationships between relative change in resistance and the applied strain when serpentine sensor experiences transverse stretching and releasing with 10% and 20% strain respectively and (b) the dependences between relative variation in resistance and the applied strain when the rectangular one undergoes transverse stretching/releasing cycle with 10% and 20% strain respectively

In contrast to the hysteresis performance of rectangular MWCNTs/PDMS sensor shown in Figure 6-8b, as to the relative change in resistance with strain 10%, the hysteresis index for rectangular one is around 23.3%, worse than the serpentine one (16.8%). In addition, with regards to the strain 20%, the hysteresis index for rectangular one reaches 30.4%, while that for serpentine one is approximately 15.2%. As a result, it can be clearly seen that the hysteresis performance of the serpentine sensor is improved compared to the conventional rectangular one. It can be attributed to the function of the serpentine structure. Despite 20% strain applied on the serpentine sensor, the MWCNTs/PDMS composite actually only yield maximal 8% strain as described in the simulation. Hence, based on the explanations above, when the composite undergoes smaller strain, the friction force between MWCNTs and PDMS matrix will not be large and the phenomenon of MWCNTs fracture will be mitigated.

6.4 Conclusion

In this chapter, a stretchable sensor based on serpentine MWCNTs/PDMS composite encapsulated with PDMS was fabricated using a facile molding technique. It was demonstrated that the serpentine sensor could exhibit more excellent response linearity to the tension strain than the conventional rectangular MWCNTs/PDMS composite sensor. Furthermore, the serpentine sensor responded differently in resistance change when subjected to tensile strain in transverse or longitudinal direction. Even though the difference is not large enough, it gives inspiration to the further investigation. Also, based on the strain simulation of the FEM, the GF was theoretically estimated which was in good agreement with the experimentally measured GF. In addition, both the hysteresis and response time performances of the serpentine sensor were both improved compared to the conventional rectangular sensor. This stretchable sensor not only exhibits a great potential to develop a multifunctional sensor but also improves the overall performance of the conventional stretchable sensor based on polymer composites.

Chapter 7 Summary and Future Work

7.1 Research Summary

This chapter summarizes all the findings of this research, in spite of relevant descriptions in previous chapters. In this research, three parts are studied, including simulation of piezoresistive property of CNTs-based conductive polymers composites, preparation of MWCNTs/PDMS composite with excellent performance and the fabrication of stretchable sensors based on MWCNTs/PDMS composite.

In chapter 3, a model embedded with straight CNTs was randomly generated in order to seek the influencing factors on the electrical properties of the CNTs-based composites, which is helpful to the following experiments. Not only were the electrical resistance of the model acquired, but also influencing factors were listed and analyzed. Furthermore, the electrical conductive behavior caused by tensile strain was simulated to gain a fundamental understanding of the piezoresistivity of the CNTs-based composite.

The fabrication method of the MWCNTs/PDMS composite was illustrated in the chapter 4. As is well known, the key problem to prepare MWCNTs/PDMS composite is to uniformly disperse MWCNTs in the PDMS matrix. After a string of trial experiments, the conventional fabrication method of MWCNTs/PDMS composite was improved in this work. There are two issues regarding fabrication methods of MWCNTs/PDMS composites. One is the strong viscosity of the MWCNTs/PDMS composites which makes it difficult to coat the mixture on the mold without bubbles, and another is the re-agglomeration phenomenon of MWCNTs after ultrasonication. The mixture was coated onto the mold using a blade and then the bubbles were forced out in the vacuum state. Through repeating this step, the flat surface of the mixture could be formed without

bubbles. In addition, the pentane, which has a low boiling point, was adopted to diminish the evaporating time, thus resulting in the mitigation of the re-agglomeration of MWCNTs.

In chapter 5, a stretchable sensor based on MWCNTs/PDMS composite was devised and fabricated. In order to maintain the stretchability of the composite and prevent the conductive composite from contacting human skins, the sandwich-like structure was designed (MWCNTs/PDMS composite was in the middle layer and PDMS were made as the top and bottom layers). In addition, the sandwich-like sensor were characterized in terms of the sensing performances, including sensitivity, hysteresis, durability, and response time. Lastly, the sensor was successfully employed to detect the human motions, wrist and finger bending.

In chapter 6, the MWCNTs-based serpentine sensor capable of distinguishing tension in different directions is designed and made. Even though the difference of resistance response subjected to longitude and transverse tensile strain is not very big, the response linearity and hysteresis were enhanced.

7.2 Summary of Contributions

The works here have yielded a load of contributions to the body of research involving CNTs-based nanocomposites.

At first, the mechanism of electrical property of CNTs-based composites are investigated in detail through a 3D model simulation. The electrical conductivity of CNTs-based composites is associated with the CNTs network constructed in the polymer matrix. The property of CNTs plays an important role in influencing the electrical conductivity of the composites. If the CNT has a large aspect ratio, the CNT volume fraction for percolation

threshold will reduce. If the electrical conductivity of the CNT is high, its composite will also have better electrical conductivity, but with no influence on percolation threshold. As to the piezoresistivity, the Poisson's ratio of the stretchable polymer matrix produce a profound effect. The low Poisson's ratio of the polymer may give an excellent sensitivity to the CNTs-based composites. In addition, if the CNT volume fraction is slightly higher than the percolation threshold range, the sensitivity of the composite will be strengthened.

Secondly, conventional fabrication approach of CNTs-based polymer composites was modified and improved. With regards to the ultrasonication method, using the solvent with a low boiling point prevents CNTs from re-agglomeration during the period of the evaporation of solvent. Among solvents which are compatible with CNTs, pentane is the best choice due to its low boiling point. The MWCNTs/PDMS composite film with good mechanical and electrical properties are successfully made.

Thirdly, the sandwich-like stretchable sensor based on the rectangular MWCNTs/PDMS composite was designed and fabricated. It not only exhibited high sensitivity (Gauge factor up to 9), but also performed well in hysteresis. In addition, it had a good performance in term of the durability of stretching and response speed to applied tension strain. Furthermore, it was demonstrated that this stretchable sensor could be employed to detect human motions with high accuracy.

Finally, the serpentine stretchable sensor based on MWCNTs/PDMS composite was made, which could differentiate the stretching direction. Even though it might not be at once used in practical application due to the low accuracy, it still improved the response linearity to tensile strain and hysteresis compared to the sandwich-like sensor.

7.3 Recommendations of Future Work

More fruitful results may be acquired by continuing to do on this research. First, with regards to the simulation of CNTs-based composite model, the investigation of CNTs' waviness can effectively enhance the accuracy of the electrical conductivity estimation. In addition, the agglomerations of CNTs are common in the polymer matrix. If the simulation can take it into account, the model may be more realistic. Furthermore, in this research, the stretching simulation merely assumed that the composite cube model would be elastically deformed and the complication strain variations around CNTs were supposed to be uniform. Thus, the future research should lay emphasis on the mechanical deformation simulation, whereas current concentration lies in the CNTs network reconfiguration.

In addition, extension should be to devise the stretchable sensor which can possess several functions, such as simultaneous pressure and tension strain detection and even temperature sensing. At present, the conventional sandwich-like sensor can be utilized to detect simple human motions with high accuracy, like finger and wrist bending. As for the serpentine sensor, even though it can differentiate the tension strain in longitude and transverse direction, it still has far to go. In future, these simple and fundamental sensors can be developed to complicated sensors, like electronic skins, smart textile and so forth. Besides, the stretchable sensor should have some characters, like light weight, portability, self-power et al., so that can be widely employed in the wearable devices.

Chapter 8 Appendix: List of MATLAB Programs

The MATLAB programs used for the numerical simulation of the CNTs composite model are listed as follows with a brief description.

1. **CNT_Model:** this is the main script. It includes these outputs: a) CNTs percolation paths are found. b) the electrical conductivity of the model are calculated.
2. **CNT_Generation:** this function randomly generates the sticks of CNTs.
3. **Dist_Point:** this function calculates the distance between the two ending point of the CNT.
4. **DistBetween2Segment:** this function calculates the minimum distance between the two adjacent CNTs and records the corresponding coordinates of the points on two CNTs.
5. **Intersection_Boundary:** this functions determines whether a stick of CNT intersect a plane of the model and returns the coordinates of the intersecting point.
6. **AngleDiff:** this function supplies incremental changes in sticks of CNTs orientation angles due to applied strain.
7. **VolFraction:** this function computes the volume fraction of CNTs in the cube model.
8. **Net_Resistance:** this function calculates the whole resistance and electrical conductivity of the cube model.
9. **Stretched_Model:** this is script to generate the stretched model based on initial model with a fixed strain and updates the resistance and electrical conductivity of the whole.
10. **Stretch:** this function is used to update the coordinates of CNTs after stretching.

[CNT_Model]:

```
Clear; clc;

% the outputs includes:

% 1) CNTs randomly generated

% 2) find out all the effective conductive CNTs

% 3) calculate the electrical conductivity of the whole model.

% Xiang Fu

% Auckland University of Technology

% August 2016

time=100; % the cycle number

vf_group=zeros(100,1);

cond_n_group=zeros(100,1);

cond_range_group=zeros(100,2);

cnt_cell_group=zeros(100,time);

effective_percent_group=zeros(100,1);

time_N=1;

number_CNT=5000; % the number of CNTs

cnt_direction=zeros(number_CNT,1);

direction_serial=zeros(9,1);

for N=number_CNT

time_i=1;

cnt_num=zeros(time,1);

cnt_cell=zeros(time,10000);

cond_cell=zeros(1,time);

cond_percolation=zeros(1,time);

time_percolation=0;

while time_i<=time

Nt=N;

lMu=0.95; lSig=0.02*lMu; % unit is 1000 nm && mean length and stdev of
CNTs

rMu=0.0023; rSig=0.02*rMu; % mean radius and stdev of CNTs
```

```

Vn=3; % scaling factor

V=[0 2;0 2;0 2]*Vn*ceil(lMu)/2; % model size

Cnt=struct('P_c',zeros(1,3),'P_s',zeros(1,3),'P_e',zeros(1,3),'theta',zeros(1,1),'phi',z
eros(1,1),'L',zeros(1,1),'D',zeros(1,1),'cube',zeros(1,Vn^3)); % created CNTs

top_intersection_infors=zeros(2000,4);

it=1;

bottom_intersection_infors=zeros(2000,4);

ib=1;

cube=zeros(Vn^3,5000);

for i=1:N

    L=normrnd(lMu,1Sig); % length of CNT

    D=2*normrnd(rMu, rSig); % diameter of CNT

    [P_c,P_s,P_e,theta,phi]=cnt_generate(V,L); % single CNT generated

    [P_s,P_e,S]=intersection_boundary(P_s,P_e,V); % CNTs connected to boundary

    % recording all the intersections of CNTs with top and bottom plane

    c=sum(S);

    if c>=1

        P_c=(P_s+P_e)/2;

        L=dist_points(P_s,P_e); % update length of CNTs

        if P_s(3)==V(3,2)

            top_intersection=[i,P_s];

            top_intersection_infors(it,:)=top_intersection;

            it=it+1;

            clear top_intersection

        elseif P_s(3)==V(3,1)

            bottom_intersection=[i,P_s];

            bottom_intersection_infors(ib,:)=bottom_intersection;

            ib=ib+1;

            clear bottom_intersection

        end

        if P_e(3)==V(3,2)

            top_intersection=[i,P_e];

            top_intersection_infors(it,:)=top_intersection;

```

```

        it=it+1;

        clear top_intersection

    elseif P_e(3)==V(3,1)

        bottom_intersection=[i,P_e];

        bottom_intersection_infors(it,:)=bottom_intersection;

        it=it+1;

        clear bottom_intersection

    end

end

% divide the model to small regions for quick search of intersected CNTs
serial_cube=zeros(1,Vn^3);

if P_s(1)==0

    serial_cubel=ceil(P_s(1)+0.0000001)+Vn*floor(P_s(2))+Vn^2*floor(P_s(3));

elseif P_s(2)==Vn||P_s(3)==Vn

    serial_cubel=ceil(P_s(1))+Vn*floor(P_s(2)-0.0000001)+Vn^2*floor(P_s(3)-0.0000001);

else

    serial_cubel=ceil(P_s(1))+Vn*floor(P_s(2))+Vn^2*floor(P_s(3));

end

if P_e(1)==0

    serial_cube2=ceil(P_e(1)+0.0000001)+Vn*floor(P_e(2))+Vn^2*floor(P_e(3));

elseif P_e(2)==Vn||P_e(3)==Vn

    serial_cube2=ceil(P_e(1))+Vn*floor(P_e(2)-0.0000001)+Vn^2*floor(P_e(3)-0.0000001);

else

    serial_cube2=ceil(P_e(1))+Vn*floor(P_e(2))+Vn^2*floor(P_e(3));

end

Diff=serial_cubel-serial_cube2;

if abs(Diff)==Vn||abs(Diff)==Vn^2||abs(Diff)==1

    serial_cube(1:2)=[serial_cubel,serial_cube2];

elseif abs(Diff)==Vn+1||abs(Diff)==Vn-1

    max=max(serial_cubel,serial_cube2);

    min=min(serial_cubel,serial_cube2);

    serial_cube3=max-Vn;

    serial_cube4=min+Vn;

```

```

        serial_cube(1:4)=[serial_cubel,serial_cube2,serial_cube3,serial_cube4];
    elseif abs(Diff)==(Vn-
1)*Vn||abs(Diff)==Vn*(Vn+1)||abs(Diff)==Vn^2+1||abs(Diff)==Vn^2-1

        max=max(serial_cubel,serial_cube2);

        min=min(serial_cubel,serial_cube2);

        serial_cube3=max-Vn^2;

        serial_cube4=min+Vn^2;

        serial_cube(1:4)=[serial_cubel,serial_cube2,serial_cube3,serial_cube4];

elseif abs(Diff)==0

        serial_cube(1)=serial_cubel;

else

        max1=max(serial_cubel,serial_cube2);

        min1=min(serial_cubel,serial_cube2);

        serial_cube3=max1-Vn^2;

        serial_cube4=min1+Vn^2;

        max2=max(serial_cube3,min1);

        min2=min(serial_cube3,min1);

        serial_cube5=max2-Vn;

        serial_cube6=min2+Vn;

        max3=max(serial_cube4,max1);

        min3=min(serial_cube4,max1);

        serial_cube7=max3-Vn;

        serial_cube8=min3+Vn;

serial_cube=[serial_cubel,serial_cube2,serial_cube3,serial_cube4,serial_cube5,serial_cub
e6,serial_cube7,serial_cube8];

end

% storing the updated CNTs into CNTs strut group

    Cnt(i).P_c=P_c;

    Cnt(i).P_s=P_s;

    Cnt(i).P_e=P_e;

    Cnt(i).theta=theta;

    Cnt(i).phi=phi;

    Cnt(i).L=L;

    Cnt(i).D=D;

```

```

        Cnt(i).cube=serial_cube;

        serial_cube(serial_cube==0)=[];

        for ms=1:length(serial_cube)

            zerotemp=find(cube(serial_cube(ms),:)==0);

            cube(serial_cube(ms),zerotemp(1))=i;

        end

        clear serial_cube1 serial_cube2 serial_cube3 serial_cube4 serial_cube5 serial_cube6
        serial_cube7 serial_cube8 max min max1 min1 max2 min2 max3 min3 i

    end

% find out the effective conductive CNTs

%%

h=0.0018; % cut-off distance of tunneling distance

intersection_infors=zeros(5000,9);

ii=0;

intersection_infors_with_tunnel=zeros(5000,10);

iit=0;

cluster=zeros(10000,10000);

row_cluster=0;

effective_cluster_serial=zeros(5000,2000);

iec=0;

icc=1;

clusternum1=zeros(5000,1);

row_cn=0;

intersection_num=zeros(5000,1);

row_in=0;

effective_cnt_serial=[];

for i=2:N

    tempserical_cube=Cnt(i).cube;

    tempserical_cube(tempserical_cube==0)=[];

    tempcube=cube(tempserical_cube,:);

    tempcube(tempcube==0)=[];

    tempcube=unique(tempcube);

```

```

tempcube (tempcube==i)=[];

unique_tempcube=tempcube (tempcube<i);

for j=unique_tempcube

    [dmin,q,Pi_ints,Pj_ints] =
    DistBetween2Segment (Cnt (i) .P_s,Cnt (i) .P_e,Cnt (j) .P_s,Cnt (j) .P_e); % minimum distance
    between CNTs

    if dmin<=(Cnt (i) .D+Cnt (j) .D)/2+h           % judge whether CNTs are conducive

        intersection_numi=i;

        intersection_numi_point=Pi_ints;

        intersection_numj=j;

        intersection_numj_point=Pj_ints;
    intersection_infor=[intersection_numi,intersection_numi_point,intersection_numj,intersec
    tion_numj_point,dmin];

        ii=ii+1;

        iit=iit+1;

        intersection_infors(ii,:)=intersection_infor;
    intersection_infors_with_tunnel(iit,:)= [intersection_infor(1:4),0,intersection_infor(5:8
    ),0];

        if dmin>(Cnt (i) .D+Cnt (j) .D)/2

            Nt=Nt+1;

            intersection_infors_with_tunnel(iit,6)=Nt;

            intersection_infors_with_tunnel(iit,7:9)=intersection_infor(2:4);

            intersection_infors_with_tunnel(iit,10)=1;

            iit=iit+1;

            intersection_infors_with_tunnel(iit,1:4)=intersection_infor(5:8);

            intersection_infors_with_tunnel(iit,5)=0;

            intersection_infors_with_tunnel(iit,6)=Nt;

            intersection_infors_with_tunnel(iit,7:9)=intersection_infor(6:8);

            intersection_infors_with_tunnel(iit,10)=1;

        end

        clear intersection_numi intersection_numi_point intersection_numj
    intersection_numj_point intersection_infor

        clear dmin q Pi_ints Pj_ints

        [row1,~]=find(cluster==i);

        [row2,~]=find(cluster==j);

        D1=isempty(row1);

        D2=isempty(row2);

```

```

    if D1==1&&D2==1
        row_cluster=row_cluster+1;
        cluster(row_cluster,1:2)=[j,i];
    elseif D1==1&&D2==0
        zero_index1=find(cluster(row2,)==0);
        cluster(row2,zero_index1(1))=i;
    elseif D1==0&&D2==1
        zero_index2=find(cluster(row1,)==0);
        cluster(row1,zero_index2(1))=j;
    elseif D1==0&&D2==0
        if row1~=row2
            tempcluster=union(cluster(row1,:),cluster(row2,:));
            cluster(row1,1:length(tempcluster))=tempcluster;
            cluster(row1,:)=sort(cluster(row1(1),:),'descend');
            cluster(row2,:)=[];
            row_cluster=row_cluster-1;
            clear tempcluster
        end
    end
end

end

end

clear row1 row2 D1 D2

end

%%

[vf,as]=volFraction(Vn,lMu,Cnt,N); % volume fraction of CNTs

%%

% deleting CNTs cluster that do not connect to other groups as well as both top and
bottom plane

top_intersection_infors(all(top_intersection_infors==0,2),:)=[];

bottom_intersection_infors(all(bottom_intersection_infors==0,2),:)=[];

cluster(all(cluster==0,2),:)=[];

```

```

cluster_record=cluster;
intersect_A=[];
for i1=1:row_cluster
    AX=intersect(cluster(i1,:),top_intersection_infors(:,1)');
    BX=intersect(cluster(i1,:),bottom_intersection_infors(:,1)');
    if isempty(AX) || isempty(BX)
        row_cn=row_cn+1;
        clusternum1(row_cn,1)=i1;
    end
end
clear i1 i2
if sum(abs(clusternum1(:))~=0)
    clusternum1_delete=clusternum1;
    clusternum1_delete(clusternum1_delete==0)=[];
    cluster(clusternum1_delete,:)=[];
end
clear clusternum1_delete

% transfer storing matrix to storing vector
if sum(abs(cluster(:))~=0)
    effective_cnt_serial=cluster;
    effective_cnt_serial(effective_cnt_serial==0)=[];
end

%%

% find out effective CNT intersection points
if ~isempty(effective_cnt_serial)
    if h~=0
        intersection_infors_with_tunnel(all(intersection_infors_with_tunnel==0,2),:)=[];
        [m2,n2]=size(intersection_infors_with_tunnel);
        record_tunnel=intersection_infors_with_tunnel;
        for ix=1:m2
            if intersection_infors_with_tunnel(ix,10)==1

```

```

E=ismember(intersection_infors_with_tunnel(ix,1),effective_cnt_serial);
F=ismember(intersection_infors_with_tunnel(ix,6),effective_cnt_serial);
if E==0&&F==0
    row_in=row_in+1;
    intersection_num(row_in,1)=ix;
end
elseif intersection_infors_with_tunnel(ix,10)==0
    E=ismember(intersection_infors_with_tunnel(ix,1),effective_cnt_serial);
    F=ismember(intersection_infors_with_tunnel(ix,6),effective_cnt_serial);
    if E==0||F==0
        row_in=row_in+1;
        intersection_num(row_in,1)=ix;
    end
end
end
intersection_num(intersection_num==0)=[];
intersection_infors_with_tunnel(intersection_num,:)=[];
intersections=intersection_infors_with_tunnel;
else
    intersection_infors(all(intersection_infors==0,2),:)=[];
    [m3,n3]=size(intersection_infors);
    record_no_tunnel=intersection_infors;
    for ix=1:m3
        E=ismember(intersection_infors(ix,1),effective_cnt_serial);
        F=ismember(intersection_infors(ix,5),effective_cnt_serial);
        if E==0||F==0
            row_in=row_in+1;
            intersection_num(row_in,1)=ix;
        end
    end
end
intersection_num(intersection_num==0)=[];
intersection_infors(intersection_num,:)=[];
intersections=intersection_infors;

```

```

end

if h==0
    colx=5;
else
    colx=6;
end

intersection_union=[intersections(:,1);intersections(:,colx)];

temp_cnt=tabulate(intersection_union);

[row_temp,col_temp]=find(temp_cnt(:,2)==1);

effective_boundary=[bottom_intersection_infors(:,1);top_intersection_infors(:,1)];

% deleting needless CNTs

while ~isempty(row_temp)

    cntdelete=temp_cnt(row_temp,1);% cnt_serial appear once

    G=setdiff(cntdelete,effective_boundary);

    numd1=[];

    numd2=[];

    for i9=1:length(G)

        [rowdelete1,coldelete1]=find(intersections(:,1)==G(i9));

        [rowdelete2,coldelete2]=find(intersections(:,colx)==G(i9));

        if ~isempty(rowdelete1)

            numd1=[numd1;rowdelete1];

        elseif ~isempty(rowdelete2)

            numd2=[numd2;rowdelete2];

        end

    end

end

numd=union(numd1,numd2);

if isempty(numd)

    break

end

intersections(numd',:)=[];

intersection_union=[intersections(:,1);intersections(:,colx)];

temp_cnt=tabulate(intersection_union);

```

```

        [row_temp,col_temp]=find(temp_cnt(:,2)==1);
    end

    temp_cnt2=tabulate(intersection_union);

    effective_cnt_serial=unique(intersection_union);

    effective_cnt_serial(effective_cnt_serial==0)=[];

    effective_cnt_serial(effective_cnt_serial>N)=[];

end

%%

% calculating the resistance

delta_CNT=0.1;          % 1000S/nm

if ~isempty(effective_cnt_serial)

    if h~=0

        [cond,re]=net_resistance_tunnel(delta_CNT,top_intersection_infors,bottom_intersection_in
fors,intersections,rMu,lMu,Vn,N);

    else

        [cond,re]=net_resistance(delta_CNT,top_intersection_infors,bottom_intersection_infors,in
tersections,rMu,lMu,Vn);

    end

    if isnan(cond)

        continue

    end

else

    cond=0;

end

cond_cell(time_i)=cond;

if cond_cell(time_i)>1e-8

    cond_percolation(time_i)=1;

    time_percolation=time_percolation+1;

end

if ~isempty(effective_cnt_serial)

    cnt_cell(time_i,1:length(effective_cnt_serial))=effective_cnt_serial;

    cnt_num(time_i,1)=length(effective_cnt_serial);

end

```

```

%%

    time_i=time_i+1

end

cond_range=[min(cond_cell),max(cond_cell)];

cond_n=poissfit(cond_cell);

cnt_num_n=poissfit(cnt_num);

effective_percent=cnt_num_n/N;

cond_n_group(time_N,1)=cond_n;

effective_percent_group(time_N,1)=effective_percent;

cnt_cell_group(time_N,:)=cond_cell;

cond_range_group(time_N,1:2)=cond_range;

vf_group(time_N,1)=vf;

time_N=time_N+1;

if length(N)~=1

clearvars -except time_N cond_n_group effective_percent_group cnt_cell_group
cond_range_group vf_group N time cnt_cell Cnt V cube top_intersection_infors
bottom_intersection_infors Vn rMu lMu

end

end

%%

% plot the CNT model, blue lines represent for connected path of CNTs

if time==1

if ~isempty(cnt_cell)

    effective_cnts=cnt_cell(1,:);

    effective_cnts(effective_cnts==0)=[];

else effective_cnts=[];

end

for i8=1:N

    tf=ismember(i8,cnt_cell(1,:));

```

```

    if tf==1

plot3([Cnt(i8).P_s(1),Cnt(i8).P_e(1)], [Cnt(i8).P_s(2),Cnt(i8).P_e(2)], [Cnt(i8).P_s(3),Cnt(i8).P_e(3)], 'b', 'LineWidth',1.2)

        hold on

    elseif tf==0

plot3([Cnt(i8).P_s(1),Cnt(i8).P_e(1)], [Cnt(i8).P_s(2),Cnt(i8).P_e(2)], [Cnt(i8).P_s(3),Cnt(i8).P_e(3)], 'r', 'LineWidth',0.6);

        hold on

    end

    xlim(V(1,:))

    ylim(V(2,:))

    zlim(V(3,:))

end

box on

axis equal

ax=gca;

ax.BoxStyle='full';

set(gca,'linewidth',1.5)

set(gca,'xtick',[],'ytick',[],'ztick',[])

title('CNTS STRETCHING MODEL');

x1=xlabel('X AXIS');

x2=ylabel('Y AXIS');

x3=zlabel('Z AXIS STRETCHING' );

set(gca,'YGrid','on')

end

%% count the number of CNTs with fixed orientation

% cnt_direction=Cnt.theta;

% for i_direction=1:number_CNT

%     cnt_direction(i)=abs(cnt_direction(i))*90/pi;

%     if cnt_direction(i)<=10

```

```

%         direction_serial(1)=direction_serial(1)+1;
%     elseif 10<cnt_direction(i)<=20
%         direction_serial(2)=direction_serial(2)+1;
%             elseif 10<cnt_direction(i)<=20
%                 direction_serial(2)=direction_serial(2)+1;
%                     elseif 10<cnt_direction(i)<=20
%                         direction_serial(2)=direction_serial(2)+1;
%                             elseif 10<cnt_direction(i)<=20
%                                 direction_serial(2)=direction_serial(2)+1;
%                                     elseif 10<cnt_direction(i)<=20
%                                         direction_serial(2)=direction_serial(2)+1;
%                                             elseif 10<cnt_direction(i)<=20
%                                                 direction_serial(2)=direction_serial(2)+1;
%                                                     elseif 10<cnt_direction(i)<=20
%                                                         direction_serial(2)=direction_serial(2)+1;
%                                                             elseif 10<cnt_direction(i)<=20
%                                                                 direction_serial(2)=direction_serial(2)+1;
%                                                                     elseif 10<cnt_direction(i)<=20
%                                                                         direction_serial(2)=direction_serial(2)+1;
%                                                                                                     end
% end

% if time==1&&length(N)==1

% save('C:\Users\xfu\Desktop\matlab stretching cnt\mat\Cnt.mat','Cnt');

% save('C:\Users\xfu\Desktop\matlab stretching
cnt\mat\effective_cnt_serial.mat','effective_cnt_serial');

% save('C:\Users\xfu\Desktop\matlab stretching cnt\mat\re.mat','re');

% end

```

```

=====
=====

```

[CNT_Generation]

```

% this function randomly generates the coordinates (P_c, P_s, P_e) and the orientation
(theta, phi) of CNTs

```

```

function [P_c,P_s,P_e,theta,phi]=cnt_generate(V,L)

d=V(:,2)-V(:,1);

Lx=d(1);

Ly=d(2);

Lz=d(3);

x =Lx*rand;

y =Ly*rand;

z =Lz*rand;

theta=pi*(1-2*rand)/2;

phi=2*pi*rand;

P_c=[x,y,z];

```

```

x1=x+(L/2)*sin(theta)*cos(phi);

y1=y-(L/2)*sin(theta)*sin(phi);

z1=z-(L/2)*cos(theta);

P_s=[x1,y1,z1];

```

```

x2=x-(L/2)*sin(theta)*cos(phi);

y2=y+(L/2)*sin(theta)*sin(phi);

z2=z+(L/2)*cos(theta);

P_e=[x2,y2,z2];

```

```

=====
=====

```

[Dist_Point]

```

% this function is used to calculate the distance between two points

```

```

function d=dist_points(Pi,Pj)

d=sqrt(sum((Pi-Pj).^2));

end

```

```
=====
=====
```

[DistBetween2Segment]

```
% this function is to calculate the minimum distance between CNTs
```

```
function [distance, varargout] = DistBetween2Segment(p1, p2, p3, p4)
```

```
    u = p1 - p2;
```

```
    v = p3 - p4;
```

```
    w = p2 - p4;
```

```
    a = dot(u,u);
```

```
    b = dot(u,v);
```

```
    c = dot(v,v);
```

```
    d = dot(u,w);
```

```
    e = dot(v,w);
```

```
    D = a*c - b*b;
```

```
    sD = D;
```

```
    tD = D;
```

```
    SMALL_NUM = 0.00000001;
```

```
    % compute the line parameters of the two closest points
```

```
    if (D < SMALL_NUM) % the lines are almost parallel
```

```
        sN = 0.0; % force using point P0 on segment S1
```

```
        sD = 1.0; % to prevent possible division by 0.0 later
```

```
        tN = e;
```

```
        tD = c;
```

```
    else % get the closest points on the infinite lines
```

```
        sN = (b*e - c*d);
```

```
        tN = (a*e - b*d);
```

```

if (sN < 0.0)    % sc < 0 => the s=0 edge is visible

    sN = 0.0;

    tN = e;

    tD = c;

elseif (sN > sD)% sc > 1 => the s=1 edge is visible

    sN = sD;

    tN = e + b;

    tD = c;

end

end

if (tN < 0.0)          % tc < 0 => the t=0 edge is visible

    tN = 0.0;

    % recompute sc for this edge

    if (-d < 0.0)

        sN = 0.0;

    elseif (-d > a)

        sN = sD;

    else

        sN = -d;

        sD = a;

    end

elseif (tN > tD)      % tc > 1 => the t=1 edge is visible

    tN = tD;

    % recompute sc for this edge

    if ((-d + b) < 0.0)

        sN = 0;

    elseif ((-d + b) > a)

        sN = sD;

    else

        sN = (-d + b);

        sD = a;

    end

end

```

```

end

% finally do the division to get sc and tc
if(abs(sN) < SMALL_NUM)
    sc = 0.0;
else
    sc = sN / sD;
end

if(abs(tN) < SMALL_NUM)
    tc = 0.0;
else
    tc = tN / tD;
end

% get the difference of the two closest points
dP = w + (sc * u) - (tc * v); % = S1(sc) - S2(tc)

distance = norm(dP);
outV = dP;

varargout(1) = {outV}; % vector connecting the closest points
varargout(2) = {p2+sc*u}; % Closest point on object 1
varargout(3) = {p4+tc*v}; % Closest point on object 2

end

```

```

=====
=====

```

[Intersection_Boundary]

```
% this function is to check the contact of CNTs with model boundary and to update the
coordinate of CNTs.
```

```
function [P_s,P_e,S]=intersection_boundary(Ptemp_s,Ptemp_e,V)
```

```
S=zeros(1,6);%top,bottom,right,left,front,back
```

```
P_s=Ptemp_s;
```

```
P_e=Ptemp_e;
```

```
x1=Ptemp_s(1);
```

```
y1=Ptemp_s(2);
```

```
z1=Ptemp_s(3);
```

```
x2=Ptemp_e(1);
```

```
y2=Ptemp_e(2);
```

```
z2=Ptemp_e(3);
```

```
if z1>=V(3,2)% start point outside top
```

```
    S(1)=1;
```

```
    z=V(3,2);
```

```
    x=(z-z1)*(x1-x2)/(z1-z2)+x1;%update x
```

```
    y=(z-z1)*(y1-y2)/(z1-z2)+y1;%update y
```

```
    P_s=[x,y,z];%update P_s point
```

```
    x1=x;
```

```
    y1=y;
```

```
    z1=z;
```

```
elseif z1<=V(3,1)% start point outside bottom
```

```
    S(2)=1;
```

```
    z=V(3,1);
```

```
    x=(z-z1)*(x1-x2)/(z1-z2)+x1;%update x
```

```
    y=(z-z1)*(y1-y2)/(z1-z2)+y1;%update y
```

```
    P_s=[x,y,z];%update P_s point
```

```
    x1=x;
```

```

    y1=y;

    z1=z;

end

if z2>=V(3,2)% end point outside top

    S(1)=1;

    z=V(3,2);

    x=(z-z1)*(x1-x2)/(z1-z2)+x1;%update x
    y=(z-z1)*(y1-y2)/(z1-z2)+y1;%update y
    P_e=[x,y,z];%update P_e point

    x2=x;

    y2=y;

    z2=z;

elseif z2<=V(3,1)% end point outside bottom

    S(2)=1;

    z=V(3,1);

    x=(z-z1)*(x1-x2)/(z1-z2)+x1;%update x
    y=(z-z1)*(y1-y2)/(z1-z2)+y1;%update y
    P_e=[x,y,z];%update P_e point

    x2=x;

    y2=y;

    z2=z;

end

if y1>=V(2,2)% start point outside right

    S(3)=1;

    y=V(2,2);

    x=(y-y1)*(x1-x2)/(y1-y2)+x1;%update x
    z=(y-y1)*(z1-z2)/(y1-y2)+z1;%update z
    P_s=[x,y,z];%update P_s point

    x1=x;

    y1=y;

    z1=z;

```

```

elseif y1<=V(2,1)% start point outside left

    S(4)=1;

    y=V(2,1);

    x=(y-y1)*(x1-x2)/(y1-y2)+x1;%update x
    z=(y-y1)*(z1-z2)/(y1-y2)+z1;%update z

    P_s=[x,y,z];%update P_s point

    x1=x;

    y1=y;

    z1=z;

end

if y2>=V(2,2)% end point outside right

    S(3)=1;

    y=V(2,2);

    x=(y-y1)*(x1-x2)/(y1-y2)+x1;%update x
    z=(y-y1)*(z1-z2)/(y1-y2)+z1;%update z

    P_e=[x,y,z];%update P_e point

    x2=x;

    y2=y;

    z2=z;

elseif y2<=V(2,1)% end point outside left

    S(4)=1;

    y=V(2,1);

    x=(y-y1)*(x1-x2)/(y1-y2)+x1;%update x
    z=(y-y1)*(z1-z2)/(y1-y2)+z1;%update z

    P_e=[x,y,z];%update P_e point

    x2=x;

    y2=y;

    z2=z;

end

if x1>=V(1,2)% start point outside front

    S(5)=1;

```

```

x=V(1,2);

y=(x-x1)*(y1-y2)/(x1-x2)+y1;%update y

z=(x-x1)*(z1-z2)/(x1-x2)+z1;%update z

P_s=[x,y,z];%update P_s point

x1=x;

y1=y;

z1=z;

elseif x1<=V(1,1)% start point outside back

S(6)=1;

x=V(1,1);

y=(x-x1)*(y1-y2)/(x1-x2)+y1;%update y

z=(x-x1)*(z1-z2)/(x1-x2)+z1;%update z

P_s=[x,y,z];%update P_s point

x1=x;

y1=y;

z1=z;

end

if x2>=V(1,2)% end point outside front

S(5)=1;

x=V(1,2);

y=(x-x1)*(y1-y2)/(x1-x2)+y1;%update y

z=(x-x1)*(z1-z2)/(x1-x2)+z1;%update z

P_e=[x,y,z];%update P_e point

x2=x;

y2=y;

z2=z;

elseif x2<=V(1,1)% end point outside back

S(6)=1;

x=V(1,1);

y=(x-x1)*(y1-y2)/(x1-x2)+y1;%update y

z=(x-x1)*(z1-z2)/(x1-x2)+z1;%update z

P_e=[x,y,z];%update P_e point

x2=x;

```

```

y2=y;
z2=z;
end

```

```

=====
=====

```

[AngleDiff]

```

% this function yields the orientation variation of CNTs after stretched

```

```

%

```

```

% This was written by: Giang Pham

```

```

function[T,P]=angleDiff(t,p)

```

```

T=zeros(6,length(t));

```

```

P=T;

```

```

T(1,:)=sin(2*t).*cos(p).^2/2;

```

```

T(2,:)=sin(2*t).*sin(p).^2/2;

```

```

T(3,:)=sin(2*t)/2;

```

```

T(4,:)=sin(2*t).*sin(2*p)/2;

```

```

T(5,:)=sin(p).*cos(2*t);

```

```

=====
=====

```

[VolFraction]

```

% this function is to calculate the CNT volume fraction.

```

```

function [f,as1]=volFraction(Vn,lMu,g,N)

```

```

volR=0;

volV=(ceil(lMu)*Vn)^3;           % the model volume

sum=0;

for i=1:N

tempD=g(i).D;

tempL=g(i).L;

volcnt=pi*tempL*tempD^2/4;      % the CNT volume

volR=volR+volcnt;

as=tempL/tempD;

sum=sum+as;

clear tempD tempL;

end

f=volR/volV;

asl=sum/N;                       % the aspect ratio of CNTs in the model

=====
=====

```

[Net_Resistance]

```

% this function calculates the resistance and electrical conductivity of the model

function
[cond,RRR]=net_resistance_tunnel(delta_CNT,top_intersection_infors,bottom_intersection_i
nfors,intersection_infors_with_tunnel,rMu,lMu,Vn,N)

D=2*rMu;

VOLT=200;

node_top_L=length(top_intersection_infors);

node_bottom_L=length(bottom_intersection_infors);

[node_intersection_L,~]=size(intersection_infors_with_tunnel);

network_resistors=zeros(node_intersection_L,node_intersection_L);

```

```

num_vec=[intersection_infors_with_tunnel(:,1),intersection_infors_with_tunnel(:,6)];
for j=1:node_intersection_L
    nums=intersection_infors_with_tunnel(j,1);
    nume=intersection_infors_with_tunnel(j,6);
    ps=intersection_infors_with_tunnel(j,2:4);
    pe=intersection_infors_with_tunnel(j,7:9);
    [r,c,~]= find(num_vec==nums);
    if ~isempty(r)
        p=[];
        node=[];
        for kk=1:length(r)
            if r(kk)~=j
                node=[node;r(kk)];
                if c(kk)==1
                    p=[p;intersection_infors_with_tunnel(r(kk),2:4)];
                elseif c(kk)==2
                    p=[p;intersection_infors_with_tunnel(r(kk),7:9)];
                end
            end
        end
    end
    [m,~]=size(p);
    if m==1
        LC=dist_points(ps,p);
        RN=CNT_resistance(LC,delta_CNT,D);
        network_resistors(j,node)=1/RN;
    elseif m==2
        LC1=dist_points(ps,p(1,:));
        LC2=dist_points(ps,p(2,:));
        if sign(p(1,:)-ps)==sign(p(2,:)-ps)
            if LC1<LC2
                RN=CNT_resistance(LC1,delta_CNT,D);
                network_resistors(j,node(1))=1/RN;
            else

```

```

        RN=CNT_resistance(LC2,delta_CNT,D);
        network_resistors(j,node(2))=1/RN;
    end
else
    RN=CNT_resistance(LC1,delta_CNT,D);
    network_resistors(j,node(1))=1/RN;
    RN=CNT_resistance(LC2,delta_CNT,D);
    network_resistors(j,node(2))=1/RN;
end
elseif m>=3
    pl=p(1,:);
    pr=[];
    nodel=node(1);
    noder=[];
    for mk=2:m
        if sign(pl-ps)==sign(p(mk,:)-ps)
            LC1=dist_points(ps,pl);
            LC2=dist_points(ps,p(mk,:));
            if LC2<LC1
                pl=p(mk,:);
                nodel=node(mk);
            end
        else
            if isempty(pr)
                pr=p(mk,:);
                noder=node(mk);
            else
                LC1=dist_points(ps,pr);
                LC2=dist_points(ps,p(mk,:));
                if LC2<LC1
                    pr=p(mk,:);
                    noder=node(mk);
                end
            end
        end
    end
end

```

```

        end

    end

end

if ~isempty(pl)

    LC=dist_points(ps,pl);

    RN=CNT_resistance(LC,delta_CNT,D);

    network_resistors(j,nodel)=1/RN;

end

if ~isempty(pr)

    LC=dist_points(ps,pr);

    RN=CNT_resistance(LC,delta_CNT,D);

    network_resistors(j,noder)=1/RN;

end

end

end

clear r c v

[r,c,~]= find(num_vec==nume);

if ~isempty(r)

    p=[];

    node=[];

    for mm=1:length(r)

        if r(mm)~=j

            node=[node;r(mm)];

            if c(mm)==1

                p=[p;intersection_infors_with_tunnel(r(mm),2:4)];

            elseif c(mm)==2

                p=[p;intersection_infors_with_tunnel(r(mm),7:9)];

            end

        end

    end

end

[m,~]=size(p);

if m==1

    LC=dist_points(pe,p);

```

```

if intersection_infors_with_tunnel(j,10)==0
    RN=CNT_resistance(LC,delta_CNT,D);
elseif intersection_infors_with_tunnel(j,6)>N
    RN=tunnelling_resistance(LC-0.9*D,D);
end
network_resistors(j,node)=1/RN;
elseif m==2
    LC1=dist_points(pe,p(1,:));
    LC2=dist_points(pe,p(2,:));
    if sign(p(1,)-pe)==sign(p(2,)-pe)
        if LC1<LC2
            if intersection_infors_with_tunnel(j,10)==0
                RN=CNT_resistance(LC1,delta_CNT,D);
            elseif intersection_infors_with_tunnel(j,6)>N
                RN=tunnelling_resistance(LC1-0.9*D,D);
            end
            network_resistors(j,node(1))=1/RN;
        else
            if intersection_infors_with_tunnel(j,10)==0
                RN=CNT_resistance(LC2,delta_CNT,D);
            elseif intersection_infors_with_tunnel(j,6)>N
                RN=tunnelling_resistance(LC2-0.9*D,D);
            end
            network_resistors(j,node(2))=1/RN;
        end
    else
        if intersection_infors_with_tunnel(j,10)==0
            RN=CNT_resistance(LC1,delta_CNT,D);
        else
            RN=tunnelling_resistance(LC1-0.9*D,D);
        end
        network_resistors(j,node(1))=1/RN;
        if intersection_infors_with_tunnel(j,10)==0

```

```

        RN=CNT_resistance(LC2,delta_CNT,D);
    else
        RN=tunnelling_resistance(LC2-0.9*D,D);
    end
    network_resistors(j,node(2))=1/RN;
end
elseif m>=3
    pl=p(1,:);
    pr=[];
    nodel=node(1);
    noder=[];
    for mk=2:m
        if sign(pl-pe)==sign(p(mk,:)-pe)
            LC1=dist_points(pe,pl);
            LC2=dist_points(pe,p(mk,:));
            if LC2<LC1
                pl=p(mk,:);
                nodel=node(mk);
            end
        else
            if isempty(pr)
                pr=p(mk,:);
                noder=node(mk);
            else
                LC1=dist_points(pe,pr);
                LC2=dist_points(pe,p(mk,:));
                if LC2<LC1
                    pr=p(mk,:);
                    noder=node(mk);
                end
            end
        end
    end
end
end
end

```

```

    if ~isempty(pl)
        LC=dist_points(pe,pl);
        if intersection_infors_with_tunnel(j,10)==0
            RN=CNT_resistance(LC,delta_CNT,D);
        else
            RN=tunnelling_resistance(LC-0.9*D,D);
        end
        network_resistors(j,node1)=1/RN;
    end
end
if ~isempty(pr)
    LC=dist_points(pe,pr);
    if intersection_infors_with_tunnel(j,10)==0
        RN=CNT_resistance(LC,delta_CNT,D);
    else
        RN=tunnelling_resistance(LC-0.9*D,D);
    end
    network_resistors(j,noder)=1/RN;
end
end
end

clearvars -except network_resistors top_intersection_infors
intersection_infors_with_tunnel Vn bottom_intersection_infors node_intersection_L
node_top_L node_bottom_L delta_CNT D VOLT rMu lMu

network_resistors=-network_resistors;

for iii=1:node_intersection_L
    network_resistors(iii,iii)=-sum(network_resistors(iii,:));
end

clear iii

I=zeros(node_intersection_L,1);

R_Ins_T=[];

num_vec=[intersection_infors_with_tunnel(:,1),intersection_infors_with_tunnel(:,6)];

```

```

for iii=1:node_top_L
    num=top_intersection_infors(iii,1);
    p_top=top_intersection_infors(iii,2:4);
    [r,c,~]= find(num_vec==num);
    if ~isempty(r)
        p=[];
        node=[];
        for nn=1:length(r)
            node=[node;r(nn)];
            if c(nn)==1
                p=[p;intersection_infors_with_tunnel(r(nn),2:4)];
            elseif c(nn)==2
                p=[p;intersection_infors_with_tunnel(r(nn),7:9)];
            end
        end
    end
    [m,~]=size(p);
    if m==1
        LC=dist_points(p_top,p);
        RN=CNT_resistance(LC,delta_CNT,D);
        network_resistors(node,node)=network_resistors(node,node)+(1/RN);
        I(node)=I(node)+VOLT/RN;
        R_Ins_T=[R_Ins_T;[node,RN]];
    elseif m==2
        LC1=dist_points(p_top,p(1,:));
        LC2=dist_points(p_top,p(2,:));
        if LC1<LC2
            RN=CNT_resistance(LC1,delta_CNT,D);
            I(node(1))=I(node(1))+VOLT/RN;
            network_resistors(node(1),node(1))=network_resistors(node(1),node(1))+1/RN;
            R_Ins_T=[R_Ins_T;[node(1),RN]];
        else
            RN=CNT_resistance(LC2,delta_CNT,D);

```

```

I (node (2)) = I (node (2)) + VOLT / RN

network_resistors (node (2), node (2)) = network_resistors (node (2), node (2)) + (1 / RN);

R_Ins_T = [R_Ins_T; [node (2), RN]];

end

elseif m >= 3

p1 = p (1, :);

nodel = node (1);

for mk = 2 : m

LC1 = dist_points (p_top, p1);

LC2 = dist_points (p_top, p (mk, :));

if LC2 < LC1

p1 = p (mk, :);

nodel = node (mk);

end

end

LC = dist_points (p_top, p1);

RN = CNT_resistance (LC, delta_CNT, D);

I (nodel) = I (nodel) + VOLT / RN;

network_resistors (nodel, nodel) = network_resistors (nodel, nodel) + (1 / RN);

R_Ins_T = [R_Ins_T; [nodel, RN]];

end

end

clear iii

for iii = 1 : node_bottom_L

num = bottom_intersection_infors (iii, 1);

p_bottom = bottom_intersection_infors (iii, 2 : 4);

[r, c, ~] = find (num_vec == num);

if ~isempty (r)

p = [];

node = [];

for nn = 1 : length (r)

node = [node; r (nn)];

end

end

end

```

```

        if c(nn)==1
            p=[p;intersection_infors_with_tunnel(r(nn),2:4)];
        elseif c(nn)==2
            p=[p;intersection_infors_with_tunnel(r(nn),7:9)];
        end
    end
end
[m,~]=size(p);
if m==1
    LC=dist_points(p_bottom,p);
    RN=CNT_resistance(LC,delta_CNT,D);
    network_resistors(node,node)=network_resistors(node,node)+(1/RN);
elseif m==2
    LC1=dist_points(p_bottom,p(1,:));
    LC2=dist_points(p_bottom,p(2,:));

    if LC1<LC2
        RN=CNT_resistance(LC1,delta_CNT,D);

network_resistors(node(1),node(1))=network_resistors(node(1),node(1))+1/RN;
    else
        RN=CNT_resistance(LC2,delta_CNT,D);

network_resistors(node(2),node(2))=network_resistors(node(2),node(2))+1/RN;
    end
elseif m>=3
    pl=p(1,:);
    nodel=node(1);
    for mk=2:m
        LC1=dist_points(p_bottom,pl);
        LC2=dist_points(p_bottom,p(mk,:));

        if LC2<LC1
            pl=p(mk,:);
            nodel=node(mk);
        end
    end
end

```

```

end

LC=dist_points(p_bottom,pl);

RN=CNT_resistance(LC,delta_CNT,D);

network_resistors(nodel,nodel)=network_resistors(nodel,nodel)+(1/RN);

end

end

end

clearvars -except network_resistors top_intersection_infors
intersection_infors_with_tunnel bottom_intersection_infors I Vn R_Ins_T rMu lMu

%x= gaussj(network_resistors,I);

x = pcg(network_resistors,I,1e-6,10000);

C=0;

[mm,~]=size(R_Ins_T);

for inum=1:length(I)

    if(I(inum)>0)

        for rnum=1:mm

            if R_Ins_T(rnum,1)==inum

                C=C+(200-abs(x(inum)))/R_Ins_T(rnum,2);

            end

        end

    end

end

end

RRR=200/C;

RRR=abs(RRR);

cond=1/(RRR*Vn*lMu*1e-6);           % electrical conductivity

```

```

=====
=====

```

[Stretched_Model]

% This script is used to generate the stretched model and updated the coordinates of CNTs.

% The output includes:

```

% 1) the new effective conductive CNTs are found out

% 2) the resistance and the electrical conductivity of the stretched model are obtained.

clear

clc

% load the origin model

load('C:\Users\xfu\Desktop\matlab stretching cnt\mat\Cnt.mat','Cnt');

load('C:\Users\xfu\Desktop\matlab stretching
cnt\mat\effective_cnt_serial.mat','effective_cnt_serial');load('C:\Users\xfu\Desktop\mat
lab stretching cnt\mat\re.mat','re');

Stretched_Cnt=struct('P_c',zeros(1,3),'P_s',zeros(1,3),'P_e',zeros(1,3),'theta',zeros(1,
1),'phi',zeros(1,1),'L',zeros(1,1),'D',zeros(1,1));

s=0:0.05:0.1; % strain range from 0 to 1 and along the z-
axis 0:0.05:1

v=0.2; % Poisson's ratio

Vn=2;

V=[-1 1;-1 1;-1 1]*Vn/2;

delta_CNT=1; % unit is S/1000nm

delta_re=zeros(1,3);

ire=1;

N=length(Cnt);

vf=zeros(1,1);

for is=1:length(s)

    top_intersection_infors=zeros(2000,4);

    it=1;

    bottom_intersection_infors=zeros(2000,4);

    ib=1;

    intersection_infors=zeros(3000,9);

    ii=1;

    cluster=zeros(5000,2000); % storing the cnt cluster sorted

    row_cluster=0;

    effective_cluster_serial=zeros(5000,2000);

    iec=0;

    tempcnt=zeros(2000,2);

    itc=1;

```

```

count_cluster=zeros(2000,2);

icc=1;

clusternum1=zeros(1000,1);

row_cn=0;

clusternum2=zeros(1000,1);

row_cn2=0;

clusternum3=[];

intersection_num=zeros(1000,1);

row_in=0;

cluster_top=zeros(1000,2000);

cluster_top_serial=zeros(1000,1);

row_top=0;

cluster_bottom=zeros(1000,2000);

cluster_bottom_serial=zeros(1000,1);

row_bottom=0;

cluster_middle=zeros(1000,2000);

cluster_middle_serial=zeros(1000,1);

row_middle=0;

effective_cnt_serial=[];

temp_remain_serial=[];

if s(is)==0

    re_initial=re;

    delta_re(1)=(re-re_initial)/re_initial;

    figure(is)

    subplot(1,2,1)

    plot(s(is),delta_re(1),'b*');

    for i8=1:N

        tf=ismember(i8,effective_cnt_serial);

        if tf==0

            figure(is)

            subplot(1,2,2)

```

```

plot3([Cnt(i8).P_s(1),Cnt(i8).P_e(1)], [Cnt(i8).P_s(2),Cnt(i8).P_e(2)], [Cnt(i8).P_s(3),Cnt(i8).P_e(3)], 'r', 'LineWidth',0.5);

        hold on

        elseif tf==1

                figure(is)

                subplot(1,2,2)

plot3([Cnt(i8).P_s(1),Cnt(i8).P_e(1)], [Cnt(i8).P_s(2),Cnt(i8).P_e(2)], [Cnt(i8).P_s(3),Cnt(i8).P_e(3)], 'b', 'LineWidth',0.8)

        hold on

        end

end

xlim(V(1,:))

ylim(V(2,:))

zlim(V(3,:))

box on

ax=gca;

ax.BoxStyle='full';

set(gca,'linewidth',1.5)

set(gca,'xtick',[],'ytick',[],'ztick',[])

title('CNTS STRETCHING MODEL');

x1=xlabel('X AXIS');

x2=ylabel('Y AXIS');

x3=zlabel('Z AXIS STRETCHING' );

set(gca,'YGrid','on')

clear i8

elseif s(is)>0

        VS=V.*[1,1-v*s(is);1,1-v*s(is);1,1+s(is)];           % stretched smaple unit
volume

        for i=1:N

                Stretched_Cnt(i)=stretch(Cnt(i),s(is),v);

                if Stretched_Cnt(i).P_s(3)==VS(3,2)

                        top_intersection=[i,Stretched_Cnt(i).P_s];

                        top_intersection_infors(it,:)=top_intersection;

                        it=it+1;

```

```

clear top_intersection
elseif Stretched_Cnt(i).P_s(3)==VS(3,1)
    bottom_intersection=[i,Stretched_Cnt(i).P_s];
    bottom_intersection_infors(ib,:)=bottom_intersection;
    ib=ib+1;
    clear bottom_intersection
end
if Stretched_Cnt(i).P_e(3)==VS(3,2)
    top_intersection=[i,Stretched_Cnt(i).P_e];
    top_intersection_infors(it,:)=top_intersection;
    it=it+1;
    clear top_intersection
elseif Stretched_Cnt(i).P_e(3)==VS(3,1)
    bottom_intersection=[i,Stretched_Cnt(i).P_e];
    bottom_intersection_infors(it,:)=bottom_intersection;
    it=it+1;
    clear bottom_intersection
end
top_intersection_infors(all(top_intersection_infors==0,2),:)=[];
bottom_intersection_infors(all(bottom_intersection_infors==0,2),:)=[];

=====
=====

This section is similar to the CNT_Model.m so it is left out here.

=====
=====

%%

% calculating the resistance

if ~isempty(effective_cnt_serial)

cond_temp=net_resistance(delta_CNT,top_intersection_infors,bottom_intersection_infors,in
tersection_infors,rMu,lMu,Vn);

cond=cond_temp/(1-s(is)*v)^2;

re=1/cond;

```

```

delta_re=(re-re_initial)/re_initial;

ire=ire+1;

delta_re(1,ire)=delta_re;

temp_s=s(1:is);

figure(is)

subplot(1,2,1)

plot(temp_s,delta_re,'b*')

hold on

plot(temp_s,delta_re,'k-');

else

cond=0;

re=1000000;

end

for i9=1:N

tf=ismember(i9,effective_cnt_serial);

if tf==0

figure(is)

subplot(1,2,2)

plot3([Stretched_Cnt(i9).P_s(1),Stretched_Cnt(i9).P_e(1)], [Stretched_Cnt(i9).P_s(2),Stretched_Cnt(i9).P_e(2)], [Stretched_Cnt(i9).P_s(3),Stretched_Cnt(i9).P_e(3)]), 'r', 'LineWidth', 0.5);

hold on

elseif tf==1

figure(is)

subplot(1,2,2)

plot3([Stretched_Cnt(i9).P_s(1),Stretched_Cnt(i9).P_e(1)], [Stretched_Cnt(i9).P_s(2),Stretched_Cnt(i9).P_e(2)], [Stretched_Cnt(i9).P_s(3),Stretched_Cnt(i9).P_e(3)]), 'b', 'LineWidth', 0.8)

hold on

end

end

xlim(VS(1,:))

ylim(VS(2,:))

```

```

        zlim(VS(3,:))

        box on

        ax=gca;

        ax.BoxStyle='full';

        set(gca,'linewidth',1.5)

        set(gca,'xtick',[],'ytick',[],'ztick',[])

        title('CNTS STRETCHING MODEL');

        x1=xlabel('X AXIS');

        x2=ylabel('Y AXIS');

        x3=zlabel('Z AXIS STRETCHING' );

        set(gca,'YGrid','on')

    end

    clearvars -except Cnt s v is VS V N Vn delta_CNT ire delta_re re_initial

end

```

```

=====
=====

```

[Stretch]

```

% this function is used to generate the model that is stretched.

```

```

function Stretched_Cnt=stretch(Cnt,e,p)

```

```

P_c=Cnt.P_c;

```

```

L=Cnt.L;

```

```

theta=Cnt.theta;

```

```

phi=Cnt.phi;

```

```

x=P_c(:,1);

```

```

y=P_c(:,2);

```

```

z=P_c(:,3);

```

```

x=x*(1-e*p);

```

```

y=y*(1-e*p);
z=z*(1+e);           % change in location of CNTs due to strain e

tensor=[-e*p;-e*p;e;0;0;0];
maxStr=max(abs(tensor));
N1=round(maxStr/0.005);
incrE=tensor/N1;

for j=1:N1
    [dt,dp]=angleDiff(theta,phi);
    theta=theta+sum(dt.*incrE);
    phi=phi+sum(dp.*incrE);
end

x1=x+(L/2)*sin(theta)*cos(phi);
y1=y-(L/2)*sin(theta)*sin(phi);
z1=z-(L/2)*cos(theta);
P_s=[x1,y1,z1];

x2=x-(L/2)*sin(theta)*cos(phi);
y2=y+(L/2)*sin(theta)*sin(phi);
z2=z+(L/2)*cos(theta);
P_e=[x2,y2,z2];

Stretched_Cnt.P_c=[x,y,z];
Stretched_Cnt.P_s=P_s;
Stretched_Cnt.P_e=P_e;
Stretched_Cnt.theta=theta;
Stretched_Cnt.phi=phi;
Stretched_Cnt.L=L;
Stretched_Cnt.D=Cnt.D;

```

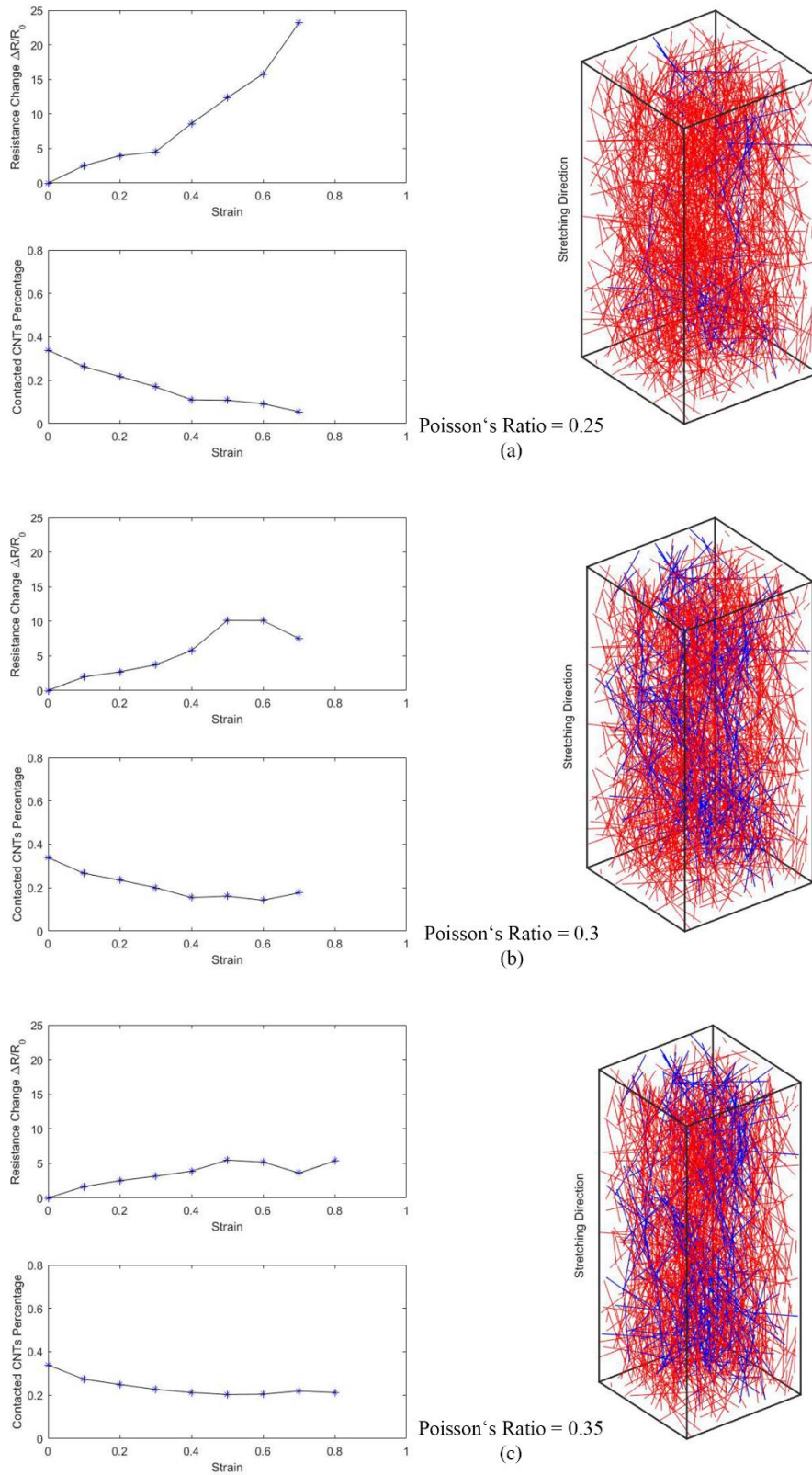


Figure 8-1 The resistance change of the CNTs composite model and the variation of the contacted CNTs percentage when the model is stretched with different polymer matrix Poisson's Ratio (a) 0.25, (b) 0.3 and (c) 0.35.

References

1. J. R. Windmiller, J. Wang, *Wearable electrochemical sensors and biosensors: a review*. *Electroanalysis*, 2013. **25**: p. 29.
2. R. C. Webb, A. P. Bonifas, A. Behnaz, Y. Zhang, K. J. Yu, H. Cheng, M. Shi, Z. Bian, Z. Liu, Y.-S. Kim, *Ultrathin conformal devices for precise and continuous thermal characterization of human skin*. *Nat. Mater.*, 2013. **12**: p. 938.
3. X. Wang, Y. Gu, Z. Xiong, Z. Cui, T. Zhang, *Silk-Molded Flexible, Ultrasensitive, and Highly Stable Electronic Skin for Monitoring Human Physiological Signals*. *Adv. Mater.*, 2014. **26**: p. 1336.
4. C. Pang, G.-Y. Lee, T.-i. Kim, S. M. Kim, H. N. Kim, S.-H. Ahn, K.-Y. Suh, *A flexible and highly sensitive strain-gauge sensor using reversible interlocking of nanofibres*. *Nat. Mater.*, 2012. **11**: p. 795.
5. G. Georgousis, C. Pandis, A. Kalamiotis, P. Georgiopoulos, A. Kyritsis, E. Kontou, P. Pissis, M. Micusik, K. Czanikova, J. Kulicek, *Strain sensing in polymer/carbon nanotube composites by electrical resistance measurement*. *Composites Part B*, 2015. **68**: p. 162.
6. H. B. Yao, J. Ge, C. F. Wang, X. Wang, W. Hu, Z. J. Zheng, Y. Ni, S. H. Yu, *A flexible and highly pressure - sensitive graphene –polyurethane sponge based on fractured microstructure design*. *Adv. Mater.*, 2013. **25**: p. 6692.
7. M. Cheng, X. Huang, C. Ma, Y. Yang, *A flexible capacitive tactile sensing array with floating electrodes*. *J. Micromech. Microeng.*, 2009. **19**: p. 115001.
8. X. Zhao, Q. Hua, R. Yu, Y. Zhang, C. Pan, *Flexible, Stretchable and Wearable Multifunctional Sensor Array as Artificial Electronic Skin for Static and Dynamic Strain Mapping*. *Adv. Electron. Mater.*, 2015. **1**: p. 1500142.
9. S. Ryu, P. Lee, J. B. Chou, R. Xu, R. Zhao, A. J. Hart, S.-G. Kim, *Extremely Elastic Wearable Carbon Nanotube Fiber Strain Sensor for Monitoring of Human Motion*. *ACS Nano*, 2015. **9**: p. 5929.
10. J. J. Park, W. J. Hyun, S. C. Mun, Y. T. Park, O. O. Park, *Highly Stretchable and Wearable Graphene Strain Sensors with Controllable Sensitivity for Human Motion Monitoring*. *ACS Appl. Mat. Interfaces*, 2015. **7**: p. 6317.
11. L. Cai, L. Song, P. Luan, Q. Zhang, N. Zhang, Q. Gao, D. Zhao, X. Zhang, M. Tu, F. Yang, *Super-stretchable, transparent carbon nanotube-based capacitive strain sensors for human motion detection*. *Sci. Rep.*, 2013. **3**: p. 3048.
12. J. Sebastian, N. Schehl, M. Bouchard, M. Boehle, L. Li, A. Lagounov, K. Lafdi, *Health monitoring of structural composites with embedded carbon nanotube coated glass fiber sensors*. *Carbon*, 2014. **66**: p. 191.

13. Y. Tang, Z. Zhao, H. Hu, Y. Liu, X. Wang, S. Zhou, J. Qiu, *Highly Stretchable and Ultrasensitive Strain Sensor Based on Reduced Graphene Oxide Microtubes–Elastomer Composite*. ACS Appl. Mat. Interfaces, 2015. **7**: p. 27432.
14. H. Yoon, J. Jang, *Conducting -polymer nanomaterials for high -performance sensor applications: issues and challenges*. Adv. Funct. Mater., 2009. **19**: p. 1567.
15. R. Yoo, J. Kim, M.-J. Song, W. Lee, J. S. Noh, *Nano-composite sensors composed of single-walled carbon nanotubes and polyaniline for the detection of a nerve agent simulant gas*. Sens. Actuators, B 2015. **209**: p. 444.
16. Y. Wang, H. Mi, Q. Zheng, H. Zhang, Z. Ma, S. Gong, *Highly stretchable and sensitive piezoresistive carbon nanotube/elastomeric triisocyanate-crosslinked polytetrahydrofuran nanocomposites*. J. Mater. Chem. C, 2016. **4**: p. 460.
17. C. Robert, J. F. o. Feller, M. I. Castro, *Sensing skin for strain monitoring made of PC–CNT conductive polymer nanocomposite sprayed layer by layer*. ACS Appl. Mat. Interfaces, 2012. **4**: p. 3508.
18. J. Hwang, J. Jang, K. Hong, K. N. Kim, J. H. Han, K. Shin, C. E. Park, *Poly(3-hexylthiophene) wrapped carbon nanotube/poly(dimethylsiloxane) composites for use in finger-sensing piezoresistive pressure sensors*. Carbon, 2011. **49**: p. 106.
19. S. Tadakaluru, W. Thongsuwan, P. Singjai, *Stretchable and flexible high-strain sensors made using carbon nanotubes and graphite films on natural rubber*. Sensors, 2014. **14**: p. 868.
20. S. Lim, D. Son, J. Kim, Y. B. Lee, J. K. Song, S. Choi, D. J. Lee, J. H. Kim, M. Lee, T. Hyeon, *Transparent and Stretchable Interactive Human Machine Interface Based on Patterned Graphene Heterostructures*. Adv. Funct. Mater., 2015. **25**: p. 375.
21. Z. Jing, Z. Guang-Yu, S. Dong-Xia, *Review of graphene-based strain sensors*. Chin. Phys. B. , 2013. **22**: p. 057701.
22. M. Amjadi, A. Pichitpajongkit, S. Lee, S. Ryu, I. Park, *Highly stretchable and sensitive strain sensor based on silver nanowire–elastomer nanocomposite*. ACS Nano, 2014. **8**: p. 5154.
23. S. Gong, W. Schwalb, Y. Wang, Y. Chen, Y. Tang, J. Si, B. Shirinzadeh, W. Cheng, *A wearable and highly sensitive pressure sensor with ultrathin gold nanowires*. Nat. Commun., 2014. **5**: p. 3132.
24. N. Angelidis, C. Wei, P. Irving, *The electrical resistance response of continuous carbon fibre composite laminates to mechanical strain*. Composites Part A, 2004. **35**: p. 1135.
25. M. F. De Volder, S. H. Tawfick, R. H. Baughman, A. J. Hart, *Carbon nanotubes: present and future commercial applications*. Science, 2013. **339**: p. 535.
26. R. Saito, G. Dresselhaus, M. S. Dresselhaus, *Physical properties of carbon nanotubes*, Imperial College Press, London 1998.
27. J. C. McDonald, G. M. Whitesides, *Poly (dimethylsiloxane) as a material for fabricating microfluidic devices*. Acc. Chem. Res., 2002. **35**: p. 491.

28. C. Martin, J. Sandler, M. Shaffer, M.-K. Schwarz, W. Bauhofer, K. Schulte, A. Windle, *Formation of percolating networks in multi-wall carbon-nanotube–epoxy composites*. *Compos. Sci. Technol.*, 2004. **64**: p. 2309.
29. J. Li, P. C. Ma, W. S. Chow, C. K. To, B. Z. Tang, J. K. Kim, *Correlations between percolation threshold, dispersion state, and aspect ratio of carbon nanotubes*. *Adv. Funct. Mater.*, 2007. **17**: p. 3207.
30. W. Ma, L. Liu, Z. Zhang, R. Yang, G. Liu, T. Zhang, X. An, X. Yi, Y. Ren, Z. Niu, *High-strength composite fibers: realizing true potential of carbon nanotubes in polymer matrix through continuous reticulate architecture and molecular level couplings*. *Nano Lett.*, 2009. **9**: p. 2855.
31. A. I. Zhanov, E. G. Pogorelov, Y.-C. Chang, *Van der Waals interaction between two crossed carbon nanotubes*. *ACS Nano*, 2010. **4**: p. 5937.
32. K. A. Shaikh, K. S. Ryu, E. D. Goluch, J.-M. Nam, J. Liu, C. S. Thaxton, T. N. Chiesl, A. E. Barron, Y. Lu, C. A. Mirkin, *A modular microfluidic architecture for integrated biochemical analysis*. *PNAS* 2005. **102**: p. 9745.
33. C.-W. Nan, Y. Shen, J. Ma, *Physical properties of composites near percolation*. *Annu. Rev. Mater. Res.*, 2010. **40**: p. 131.
34. C.-X. Liu, J.-W. Choi, *Patterning conductive PDMS nanocomposite in an elastomer using microcontact printing*. *J. Micromech. Microeng.*, 2009. **19**: p. 085019.
35. S. Yao, Y. Zhu, *Wearable multifunctional sensors using printed stretchable conductors made of silver nanowires*. *Nanoscale*, 2014. **6**: p. 2345.
36. K. K. Kim, S. Hong, H. M. Cho, J. Lee, Y. D. Suh, J. Ham, S. H. Ko, *Highly Sensitive and Stretchable Multidimensional Strain Sensor with Prestrained Anisotropic Metal Nanowire Percolation Networks*. *Nano Lett.*, 2015. **15**: p. 5240.
37. M. Amjadi, Y. J. Yoon, I. Park, *Ultra-stretchable and skin-mountable strain sensors using carbon nanotubes–Ecoflex nanocomposites*. *Nanotechnology*, 2015. **26**: p. 375501.
38. N. Lu, C. Lu, S. Yang, J. Rogers, *Highly Sensitive Skin -Mountable Strain Gauges Based Entirely on Elastomers*. *Adv. Funct. Mater.*, 2012. **22**: p. 4044.
39. F.-R. Fan, L. Lin, G. Zhu, W. Wu, R. Zhang, Z. L. Wang, *Transparent triboelectric nanogenerators and self-powered pressure sensors based on micropatterned plastic films*. *Nano Lett.*, 2012. **12**: p. 3109.
40. M. Ramuz, B. C. K. Tee, J. B. H. Tok, Z. Bao, *Transparent, optical, pressure -sensitive artificial skin for large -area stretchable electronics*. *Adv. Mater.*, 2012. **24**: p. 3223.
41. Y.-T. Lai, Y.-M. Chen, T. Liu, Y.-J. Yang, *A tactile sensing array with tunable sensing ranges using liquid crystal and carbon nanotubes composites*. *Sens. Actuators, A*, 2012. **177**: p. 48.

42. S. Jung, J. H. Kim, J. Kim, S. Choi, J. Lee, I. Park, T. Hyeon, D. H. Kim, *Reverse-Micelle -Induced Porous Pressure -Sensitive Rubber for Wearable Human –Machine Interfaces*. Adv. Mater., 2014. **26**: p. 4825.
43. G. Canavese, S. Stassi, C. Fallauto, S. Corbellini, V. Cauda, V. Camarchia, M. Pirola, C. F. Pirri, *Piezoresistive flexible composite for robotic tactile applications*. Sens. Actuators, A, 2014. **208**: p. 1.
44. J. Kim, M. Lee, H. J. Shim, R. Ghaffari, H. R. Cho, D. Son, Y. H. Jung, M. Soh, C. Choi, S. Jung, *Stretchable silicon nanoribbon electronics for skin prosthesis*. Nat. Commun., 2014. **5**: p.
45. T. Yamada, Y. Hayamizu, Y. Yamamoto, Y. Yomogida, A. Izadi-Najafabadi, D. N. Futaba, K. Hata, *A stretchable carbon nanotube strain sensor for human-motion detection*. Nat. Nanotechnol., 2011. **6**: p. 296.
46. D. J. Lipomi, M. Vosgueritchian, B. C. Tee, S. L. Hellstrom, J. A. Lee, C. H. Fox, Z. Bao, *Skin-like pressure and strain sensors based on transparent elastic films of carbon nanotubes*. Nat. Nanotechnol., 2011. **6**: p. 788.
47. W. Obityayo, T. Liu, *A review: Carbon nanotube-based piezoresistive strain sensors*. J. Sens., 2012. **2012**: p.
48. E. T. Thostenson, Z. Ren, T.-W. Chou, *Advances in the science and technology of carbon nanotubes and their composites: a review*. Compos. Sci. Technol., 2001. **61**: p. 1899.
49. P.-C. Ma, N. A. Siddiqui, G. Marom, J.-K. Kim, *Dispersion and functionalization of carbon nanotubes for polymer-based nanocomposites: a review*. Composites Part A, 2010. **41**: p. 1345.
50. Z. Zhu, L. Garcia-Gancedo, A. J. Flewitt, H. Xie, F. Moussy, W. I. Milne, *A critical review of glucose biosensors based on carbon nanomaterials: carbon nanotubes and graphene*. Sensors, 2012. **12**: p. 5996.
51. S. Iijima, *Helical microtubules of graphitic carbon*. Nature, 1991. **354**: p. 56.
52. S. Rana, R. Alagirusamy, M. Joshi, *A review on carbon epoxy nanocomposites*. J. Reinf. Plast. Compos., 2009. **28**: p. 461.
53. B. Demczyk, Y. Wang, J. Cumings, M. Hetman, W. Han, A. Zettl, R. Ritchie, *Direct mechanical measurement of the tensile strength and elastic modulus of multiwalled carbon nanotubes*. Mater. Sci. Eng., A, 2002. **334**: p. 173.
54. K. Liew, Z. Lei, L. Zhang, *Mechanical analysis of functionally graded carbon nanotube reinforced composites: a review*. Compos. Struct., 2015. **120**: p. 90.
55. J. Jyoti, S. Basu, B. P. Singh, S. Dhakate, *Superior mechanical and electrical properties of multiwall carbon nanotube reinforced acrylonitrile butadiene styrene high performance composites*. Composites Part B, 2015. **83**: p. 58.
56. Q. Li, Y. Li, X. Zhang, S. B. Chikkannanavar, Y. Zhao, A. M. Dangelewicz, L. Zheng, S. K. Doorn, Q. Jia, D. E. Peterson, *Structure -dependent electrical properties of carbon nanotube fibers*. Adv. Mater., 2007. **19**: p. 3358.

57. R. H. Baughman, A. A. Zakhidov, W. A. De Heer, *Carbon nanotubes--the route toward applications*. Science, 2002. **297**: p. 787.
58. B. Gao, Y. Chen, M. Fuhrer, D. Glatli, A. Bachtold, *Four-point resistance of individual single-wall carbon nanotubes*. Phys. Rev. Lett., 2005. **95**: p. 196802.
59. C. Berger, Y. Yi, Z. Wang, W. De Heer, *Multiwalled carbon nanotubes are ballistic conductors at room temperature*. Appl. Phys. A 2002. **74**: p. 363.
60. H. Dai, E. W. Wong, C. M. Lieber, *Probing electrical transport in nanomaterials: conductivity of individual carbon nanotubes*. Science, 1996. **272**: p. 523.
61. Y. Y. Huang, E. M. Terentjev, *Dispersion of carbon nanotubes: mixing, sonication, stabilization, and composite properties*. Polymers, 2012. **4**: p. 275.
62. Y. Y. Huang, T. P. Knowles, E. M. Terentjev, *Strength of Nanotubes, Filaments, and Nanowires From Sonication-Induced Scission*. Adv. Mater., 2009. **21**: p. 3945.
63. E. T. Thostenson, T.-W. Chou, *Processing-structure-multi-functional property relationship in carbon nanotube/epoxy composites*. Carbon, 2006. **44**: p. 3022.
64. F. H. Gojny, M. H. G. Wichmann, U. Köpke, B. Fiedler, K. Schulte, *Carbon nanotube-reinforced epoxy-composites: enhanced stiffness and fracture toughness at low nanotube content*. Compos. Sci. Technol., 2004. **64**: p. 2363.
65. A. Esawi, K. Morsi, A. Sayed, M. Taher, S. Lanka, *The influence of carbon nanotube (CNT) morphology and diameter on the processing and properties of CNT-reinforced aluminium composites*. Composites Part A, 2011. **42**: p. 234.
66. A. Esawi, K. Morsi, A. Sayed, M. Taher, S. Lanka, *Effect of carbon nanotube (CNT) content on the mechanical properties of CNT-reinforced aluminium composites*. Compos. Sci. Technol., 2010. **70**: p. 2237.
67. Z. Y. Liu, S. J. Xu, B. L. Xiao, P. Xue, W. G. Wang, Z. Y. Ma, *Effect of ball-milling time on mechanical properties of carbon nanotubes reinforced aluminum matrix composites*. Composites Part A, 2012. **43**: p. 2161.
68. H. Choi, J. Shin, B. Min, J. Park, D. Bae, *Reinforcing effects of carbon nanotubes in structural aluminum matrix nanocomposites*. J. Mater. Res., 2009. **24**: p. 2610.
69. A. M. Esawi, H. G. Salem, H. M. Hussein, A. R. Ramadan, *Effect of processing technique on the dispersion of carbon nanotubes within polypropylene carbon nanotube - composites and its effect on their mechanical properties*. Polym. Compos., 2010. **31**: p. 772.
70. T. Villmow, B. Kretschmar, P. Pötschke, *Influence of screw configuration, residence time, and specific mechanical energy in twin-screw extrusion of polycaprolactone/multi-walled carbon nanotube composites*. Compos. Sci. Technol., 2010. **70**: p. 2045.
71. E. Bilotti, R. Zhang, H. Deng, M. Baxendale, T. Peijs, *Fabrication and property prediction of conductive and strain sensing TPU/CNT nanocomposite fibres*. J. Mater. Chem., 2010. **20**: p. 9449.

72. A. M. K. Esawi, K. Morsi, A. Sayed, A. A. Gawad, P. Borah, *Fabrication and properties of dispersed carbon nanotube–aluminum composites*. Mater. Sci. Eng., A, 2009. **508**: p. 167.
73. P. C. Ma, S. Q. Wang, J.-K. Kim, B. Z. Tang, *In-situ amino functionalization of carbon nanotubes using ball milling*. J. Nanosci. Nanotechnol., 2009. **9**: p. 749.
74. A. Isayev, R. Kumar, T. M. Lewis, *Ultrasound assisted twin screw extrusion of polymer–nanocomposites containing carbon nanotubes*. Polymer, 2009. **50**: p. 250.
75. M. Rahmat, P. Hubert, *Carbon nanotube–polymer interactions in nanocomposites: A review*. Compos. Sci. Technol., 2011. **72**: p. 72.
76. Z. Wang, Z. Liang, B. Wang, C. Zhang, L. Kramer, *Processing and property investigation of single-walled carbon nanotube (SWNT) buckypaper/epoxy resin matrix nanocomposites*. Composites Part A, 2004. **35**: p. 1225.
77. B. Arash, Q. Wang, V. Varadan, *Mechanical properties of carbon nanotube/polymer composites*. Sci. Rep., 2014. **4**: p. 6479.
78. R. G. De Villoria, A. Miravete, *Mechanical model to evaluate the effect of the dispersion in nanocomposites*. Acta Mater., 2007. **55**: p. 3025.
79. P.-C. Ma, S.-Y. Mo, B.-Z. Tang, J.-K. Kim, *Dispersion, interfacial interaction and re-agglomeration of functionalized carbon nanotubes in epoxy composites*. Carbon, 2010. **48**: p. 1824.
80. T. Ramanathan, A. Abdala, S. Stankovich, D. Dikin, M. Herrera-Alonso, R. Piner, D. Adamson, H. Schniepp, X. Chen, R. Ruoff, *Functionalized graphene sheets for polymer nanocomposites*. Nat. Nanotechnol., 2008. **3**: p. 327.
81. J.-M. Yuan, Z.-F. Fan, X.-H. Chen, X.-H. Chen, Z.-J. Wu, L.-P. He, *Preparation of polystyrene–multiwalled carbon nanotube composites with individual-dispersed nanotubes and strong interfacial adhesion*. Polymer, 2009. **50**: p. 3285.
82. E. H. Fort, L. T. Scott, *Carbon nanotubes from short hydrocarbon templates. Energy analysis of the Diels–Alder cycloaddition/rearomatization growth strategy*. J. Mater. Chem., 2011. **21**: p. 1373.
83. R. Kaur, A. Paul, A. Deep, *Conjugation of chlorinated carbon nanotubes with quantum dots for electronic applications*. Mater. Lett., 2014. **117**: p. 165.
84. J. L. Stevens, A. Y. Huang, H. Peng, I. W. Chiang, V. N. Khabashesku, J. L. Margrave, *Sidewall amino-functionalization of single-walled carbon nanotubes through fluorination and subsequent reactions with terminal diamines*. Nano Lett., 2003. **3**: p. 331.
85. X. Bai, C. Wan, Y. Zhang, Y. Zhai, *Reinforcement of hydrogenated carboxylated nitrile–butadiene rubber with exfoliated graphene oxide*. Carbon, 2011. **49**: p. 1608.
86. A. Osorio, I. Silveira, V. Bueno, C. Bergmann, *H₂SO₄/HNO₃/HCl–functionalization and its effect on dispersion of carbon nanotubes in aqueous media*. Appl. Surf. Sci., 2008. **255**: p. 2485.

87. P. Slobodian, P. Riha, R. Olejník, U. Cvelbar, P. Sáha, *Enhancing effect of KMnO₄ oxidation of carbon nanotubes network embedded in elastic polyurethane on overall electro-mechanical properties of composite*. Compos. Sci. Technol., 2013. **81**: p. 54.
88. M.-L. Sham, J.-K. Kim, *Surface functionalities of multi-wall carbon nanotubes after UV/Ozone and TETA treatments*. Carbon, 2006. **44**: p. 768.
89. S. Wang, K. Chang, C. Yuan, *Enhancement of electrochemical properties of screen-printed carbon electrodes by oxygen plasma treatment*. Electrochim. Acta, 2009. **54**: p. 4937.
90. I.-Y. Jeon, D. W. Chang, N. A. Kumar, J.-B. Baek, in *Carbon nanotubes-Polymer nanocomposites*, InTech, 2011.
91. J. Gao, M. A. Loi, E. J. F. de Carvalho, M. C. dos Santos, *Selective wrapping and supramolecular structures of polyfluorene-carbon nanotube hybrids*. ACS Nano, 2011. **5**: p. 3993.
92. Y. Geng, M. Y. Liu, J. Li, X. M. Shi, J. K. Kim, *Effects of surfactant treatment on mechanical and electrical properties of CNT/epoxy nanocomposites*. Composites Part A, 2008. **39**: p. 1876.
93. Z. Liu, G. Liao, S. Li, Y. Pan, X. Wang, Y. Weng, X. Zhang, Z. Yang, *Efficient encapsulation of conducting polyaniline chains inside carbon nanotubes: a new strategy to prepare endohedral CNT materials*. J. Mater. Chem. A, 2013. **1**: p. 13321.
94. Z.-y. Zhang, X.-c. Xu, *Wrapping carbon nanotubes with poly (sodium 4-styrenesulfonate) for enhanced adsorption of methylene blue and its mechanism*. Chem. Eng. J., 2014. **256**: p. 85.
95. S. S. Tallury, M. A. Pasquinelli, *Molecular dynamics simulations of flexible polymer chains wrapping single-walled carbon nanotubes*. J. Phys. Chem. B, 2010. **114**: p. 4122.
96. A. Hirsch, *Functionalization of single-walled carbon nanotubes*. Angew. Chem. Int. Ed., 2002. **41**: p. 1853.
97. M. Kaleemullah, S. U. Khan, J.-K. Kim, *Effect of surfactant treatment on thermal stability and mechanical properties of CNT/polybenzoxazine nanocomposites*. Compos. Sci. Technol., 2012. **72**: p. 1968.
98. W. H. Duan, Q. Wang, F. Collins, *Dispersion of carbon nanotubes with SDS surfactants: a study from a binding energy perspective*. Chem. Sci., 2011. **2**: p. 1407.
99. I. Madni, C.-Y. Hwang, S.-D. Park, Y.-H. Choa, H.-T. Kim, *Mixed surfactant system for stable suspension of multiwalled carbon nanotubes*. Colloids Surf., A 2010. **358**: p. 101.
100. L. Vaisman, H. D. Wagner, G. Marom, *The role of surfactants in dispersion of carbon nanotubes*. Adv. Colloid Interface Sci., 2006. **128**: p. 37.
101. C. Klumpp, K. Kostarelos, M. Prato, A. Bianco, *Functionalized carbon nanotubes as emerging nanovectors for the delivery of therapeutics*. Biochim. Biophys. Acta, Biomembr., 2006. **1758**: p. 404.

102. V. Georgakilas, D. Gournis, V. Tzitzios, L. Pasquato, D. M. Guldi, M. Prato, *Decorating carbon nanotubes with metal or semiconductor nanoparticles*. J. Mater. Chem., 2007. **17**: p. 2679.
103. P. C. Ma, B. Z. Tang, J.-K. Kim, *Effect of CNT decoration with silver nanoparticles on electrical conductivity of CNT-polymer composites*. Carbon, 2008. **46**: p. 1497.
104. H.-S. Kim, Y. S. Chae, B. H. Park, J.-S. Yoon, M. Kang, H.-J. Jin, *Thermal and electrical conductivity of poly (L-lactide)/multiwalled carbon nanotube nanocomposites*. Curr. Appl Phys., 2008. **8**: p. 803.
105. C. Tang, G. Long, X. Hu, K.-w. Wong, W.-m. Lau, M. Fan, J. Mei, T. Xu, B. Wang, D. Hui, *Conductive polymer nanocomposites with hierarchical multi-scale structures via self-assembly of carbon-nanotubes on graphene on polymer-microspheres*. Nanoscale, 2014. **6**: p. 7877.
106. H. Li, J. Zhang, G. Li, F. Tan, R. Liu, R. Li, T. Zhang, H. Jin, Q. Li, *Triton assisted fabrication of uniform semiconducting single-walled carbon nanotube networks for highly sensitive gas sensors*. Carbon, 2014. **66**: p. 369.
107. N. Grossiord, J. Loos, O. Regev, C. E. Koning, *Toolbox for dispersing carbon nanotubes into polymers to get conductive nanocomposites*. Chem. Mater., 2006. **18**: p. 1089.
108. J. Gao, W. Li, H. Shi, M. Hu, R. K. Li, *Preparation, morphology, and mechanical properties of carbon nanotube anchored polymer nanofiber composite*. Compos. Sci. Technol., 2014. **92**: p. 95.
109. L. Cao, D. Su, Z. Su, X. Chen, *Fabrication of multiwalled carbon nanotube/polypropylene conductive fibrous membranes by melt electrospinning*. Ind. Eng. Chem. Res., 2014. **53**: p. 2308.
110. K. Suemori, Y. Watanabe, S. Hoshino, *Carbon nanotube bundles/polystyrene composites as high-performance flexible thermoelectric materials*. Appl. Phys. Lett., 2015. **106**: p. 113902.
111. S. Maiti, S. Suin, N. K. Shrivastava, B. Khatua, *Low percolation threshold in polycarbonate/multiwalled carbon nanotubes nanocomposites through melt blending with poly (butylene terephthalate)*. J. Appl. Polym. Sci., 2013. **130**: p. 543.
112. M. Liebscher, L. Tzounis, P. Pötschke, G. Heinrich, *Influence of the viscosity ratio in PC/SAN blends filled with MWCNTs on the morphological, electrical, and melt rheological properties*. Polymer, 2013. **54**: p. 6801.
113. J. Cha, S. Jin, J. H. Shim, C. S. Park, H. J. Ryu, S. H. Hong, *Functionalization of carbon nanotubes for fabrication of CNT/epoxy nanocomposites*. Mater. Des., 2016. **95**: p. 1.
114. D. K. Rathore, R. K. Prusty, D. S. Kumar, B. C. Ray, *Mechanical performance of CNT-filled glass fiber/epoxy composite in in-situ elevated temperature environments emphasizing the role of CNT content*. Composites Part A, 2016. **84**: p. 364.
115. C.-F. Wang, P.-K. Huang, P.-R. Hung, C.-C. Hsu, S.-R. Jian, P.-F. Yang, M.-H. Chung, *Synthesis and characterization of polydopamine modified carbon nanotube (CNT)/polydimethylsiloxane (PDMS) composites*, presented at 2015 International

Conference on Electronics Packaging and iMAPS All Asia Conference (ICEP-IAAC), Kyoto, Japan, 2015.

116. S. Leyva Egurrola, T. del Castillo Castro, M. M. Castillo Ortega, J. C. Encinas, H. Franco, P. Jesús, J. Bonilla Cruz, T. E. Lara Cenicerros, *Electrical, mechanical, and piezoresistive properties of carbon nanotube–polyaniline hybrid filled polydimethylsiloxane composites*. J. Appl. Polym. Sci., 2017. **134**: p. 44780.
117. Y. Dong, Q.-Q. Ni, L. Li, Y. Fu, *Novel vapor-grown carbon nanofiber/epoxy shape memory nanocomposites prepared via latex technology*. Mater. Lett., 2014. **132**: p. 206.
118. J. i. Masuda, J. M. Torkelson, *Dispersion and major property enhancements in polymer/multiwall carbon nanotube nanocomposites via solid-state shear pulverization followed by melt mixing*. Macromolecules, 2008. **41**: p. 5974.
119. E. Roh, B.-U. Hwang, D. Kim, B.-Y. Kim, N.-E. Lee, *Stretchable, Transparent, Ultrasensitive, and Patchable Strain Sensor for Human–Machine Interfaces Comprising a Nanohybrid of Carbon Nanotubes and Conductive Elastomers*. ACS Nano, 2015. **9**: p. 6252.
120. M. M. Rodgers, V. M. Pai, R. S. Conroy, *Recent advances in wearable sensors for health monitoring*. IEEE Sens. J., 2015. **15**: p. 3119.
121. N. Hu, H. Fukunaga, S. Atobe, Y. Liu, J. Li, *Piezoresistive strain sensors made from carbon nanotubes based polymer nanocomposites*. Sensors, 2011. **11**: p. 10691.
122. W. Bauhofer, J. Z. Kovacs, *A review and analysis of electrical percolation in carbon nanotube polymer composites*. Compos. Sci. Technol., 2009. **69**: p. 1486.
123. J. Sandler, J. Kirk, I. Kinloch, M. Shaffer, A. Windle, *Ultra-low electrical percolation threshold in carbon-nanotube-epoxy composites*. Polymer, 2003. **44**: p. 5893.
124. T. Hertel, R. E. Walkup, P. Avouris, *Deformation of carbon nanotubes by surface van der Waals forces*. Phys. Rev. B, 1998. **58**: p. 13870.
125. R. S. Ruoff, J. Tersoff, D. C. Lorents, S. Subramoney, B. Chan, *Radial deformation of carbon nanotubes by van der Waals forces*. Nature, 1993. **364**: p. 514.
126. H. Duan, B. L. Karihaloo, *Thermo-elastic properties of heterogeneous materials with imperfect interfaces: Generalized Levin's formula and Hill's connections*. J. Mech. Phys. Solids 2007. **55**: p. 1036.
127. C. Li, E. T. Thostenson, T.-W. Chou, *Dominant role of tunneling resistance in the electrical conductivity of carbon nanotube–based composites*. Appl. Phys. Lett., 2007. **91**: p. 223114.
128. S. Gong, Z. H. Zhu, S. A. Meguid, *Carbon nanotube agglomeration effect on piezoresistivity of polymer nanocomposites*. Polymer, 2014. **55**: p. 5488.
129. M. Vatani, Y. Lu, K.-S. Lee, H.-C. Kim, J.-W. Choi, *Direct-write stretchable sensors using single-walled carbon nanotube/polymer matrix*. J. Electron. Packag., 2013. **135**: p. 011009.

130. T. Akter, W. S. Kim, *Reversibly stretchable transparent conductive coatings of spray-deposited silver nanowires*. ACS Appl. Mat. Interfaces, 2012. **4**: p. 1855.
131. Y. R. Jeong, H. Park, S. W. Jin, S. Y. Hong, S. S. Lee, J. S. Ha, *Highly stretchable and sensitive strain sensors using fragmented graphene foam*. Adv. Funct. Mater., 2015. **25**: p. 4228.
132. J. Li, S. Zhao, X. Zeng, W. Huang, Z. Gong, G. Zhang, R. Sun, C.-P. Wong, *Highly Stretchable and Sensitive Strain Sensor Based on Facilely Prepared Three-Dimensional Graphene Foam Composite*. ACS Appl. Mat. Interfaces, 2016. **8**: p. 18954.
133. S. Luo, T. Liu, *Structure–property–processing relationships of single-wall carbon nanotube thin film piezoresistive sensors*. Carbon, 2013. **59**: p. 315.
134. Y. Wang, L. Wang, T. Yang, X. Li, X. Zang, M. Zhu, K. Wang, D. Wu, H. Zhu, *Wearable and highly sensitive graphene strain sensors for human motion monitoring*. Adv. Funct. Mater., 2014. **24**: p. 4666.
135. J. Park, Y. Lee, J. Hong, Y. Lee, M. Ha, Y. Jung, H. Lim, S. Y. Kim, H. Ko, *Tactile-Direction-Sensitive and Stretchable Electronic Skins Based on Human-Skin-Inspired Interlocked Microstructures*. ACS Nano, 2014. **8**: p. 12020.
136. H.-K. Lee, J. Chung, S.-I. Chang, E. Yoon, *Real-time measurement of the three-axis contact force distribution using a flexible capacitive polymer tactile sensor*. J. Micromech. Microeng., 2011. **21**: p. 035010.
137. A. Frutiger, J. T. Muth, D. M. Vogt, Y. Mengüç, A. Campo, A. D. Valentine, C. J. Walsh, J. A. Lewis, *Capacitive Soft Strain Sensors via Multicore–Shell Fiber Printing*. Adv. Mater., 2015. **27**: p. 2440.
138. D. J. Cohen, D. Mitra, K. Peterson, M. M. Maharbiz, *A highly elastic, capacitive strain gauge based on percolating nanotube networks*. Nano Lett., 2012. **12**: p. 1821.
139. Z. L. Wang, J. Song, *Piezoelectric nanogenerators based on zinc oxide nanowire arrays*. Science, 2006. **312**: p. 242.
140. G. Buchberger, R. Schwödiauer, S. Bauer, *Flexible large area ferroelectret sensors for location sensitive touchpads*. Appl. Phys. Lett., 2008. **92**: p. 123511.
141. K. I. Park, J. H. Son, G. T. Hwang, C. K. Jeong, J. Ryu, M. Koo, I. Choi, S. H. Lee, M. Byun, Z. L. Wang, *Highly - Efficient, Flexible Piezoelectric PZT Thin Film Nanogenerator on Plastic Substrates*. Adv. Mater., 2014. **26**: p. 2514.
142. I. Graz, M. Krause, S. Bauer-Gogonea, S. Bauer, S. P. Lacour, B. Ploss, M. Zirkl, B. Stadlober, S. Wagner, *Flexible active-matrix cells with selectively poled bifunctional polymer-ceramic nanocomposite for pressure and temperature sensing skin*. J. Appl. Phys., 2009. **106**: p. 034503.
143. C. Pan, L. Dong, G. Zhu, S. Niu, R. Yu, Q. Yang, Y. Liu, Z. L. Wang, *High-resolution electroluminescent imaging of pressure distribution using a piezoelectric nanowire LED array*. Nat. Photonics, 2013. **7**: p. 752.

144. L. Persano, C. Dagdeviren, Y. Su, Y. Zhang, S. Girardo, D. Pisignano, Y. Huang, J. A. Rogers, *High performance piezoelectric devices based on aligned arrays of nanofibers of poly (vinylidene fluoride-co-trifluoroethylene)*. Nat. Commun., 2013. **4**: p. 1633.
145. Q. Fan, Z. Qin, S. Gao, Y. Wu, J. Pionteck, E. Mäder, M. Zhu, *The use of a carbon nanotube layer on a polyurethane multifilament substrate for monitoring strains as large as 400%*. Carbon, 2012. **50**: p. 4085.
146. X.-G. Yu, Y.-Q. Li, W.-B. Zhu, P. Huang, T.-T. Wang, N. Hu, S.-Y. Fu, *A wearable strain sensor based on a carbonized nano-sponge/silicone composite for human motion detection*. Nanoscale, 2017. **9**: p. 6680.
147. R. Rahimi, M. Ochoa, W. Yu, B. Ziaie, *Highly Stretchable and Sensitive Unidirectional Strain Sensor via Laser Carbonization*. ACS Appl. Mat. Interfaces, 2015. **7**: p. 4463.
148. H. Lee, B. Seong, H. Moon, D. Byun, *Directly printed stretchable strain sensor based on ring and diamond shaped silver nanowire electrodes*. RSC Adv., 2015. **5**: p. 28379.
149. C.-X. Liu, J.-W. Choi, *Analyzing resistance response of embedded PDMS and carbon nanotubes composite under tensile strain*. Microelectron. Eng., 2014. **117**: p. 1.
150. C. Mattmann, F. Clemens, G. Tröster, *Sensor for measuring strain in textile*. Sensors, 2008. **8**: p. 3719.
151. L. Lin, S. Liu, Q. Zhang, X. Li, M. Ji, H. Deng, Q. Fu, *Towards tunable sensitivity of electrical property to strain for conductive polymer composites based on thermoplastic elastomer*. ACS Appl. Mat. Interfaces, 2013. **5**: p. 5815.
152. R. Zhang, H. Deng, R. Valenca, J. Jin, Q. Fu, E. Bilotti, T. Peijs, *Strain sensing behaviour of elastomeric composite films containing carbon nanotubes under cyclic loading*. Compos. Sci. Technol., 2013. **74**: p. 1.
153. S. Gong, D. T. Lai, B. Su, K. J. Si, Z. Ma, L. W. Yap, P. Guo, W. Cheng, *Highly Stretchy Black Gold E-Skin Nanopatches as Highly Sensitive Wearable Biomedical Sensors*. Adv. Electron. Mater., 2015. **1**: p.
154. L. Pan, A. Chortos, G. Yu, Y. Wang, S. Isaacson, R. Allen, Y. Shi, R. Dauskardt, Z. Bao, *An ultra-sensitive resistive pressure sensor based on hollow-sphere microstructure induced elasticity in conducting polymer film*. Nat. Commun., 2014. **5**: p.
155. C. L. Choong, M. B. Shim, B. S. Lee, S. Jeon, D. S. Ko, T. H. Kang, J. Bae, S. H. Lee, K. E. Byun, J. Im, *Highly stretchable resistive pressure sensors using a conductive elastomeric composite on a micropylamid array*. Adv. Mater., 2014. **26**: p. 3451.
156. J. Park, Y. Lee, J. Hong, M. Ha, Y.-D. Jung, H. Lim, S. Y. Kim, H. Ko, *Giant tunneling piezoresistance of composite elastomers with interlocked microdome arrays for ultrasensitive and multimodal electronic skins*. ACS Nano, 2014. **8**: p. 4689.
157. J.-H. Kong, N.-S. Jang, S.-H. Kim, J.-M. Kim, *Simple and rapid micropatterning of conductive carbon composites and its application to elastic strain sensors*. Carbon, 2014. **77**: p. 199.

158. F. Panozzo, M. Zappalorto, M. Quaresimin, *Analytical model for the prediction of the piezoresistive behavior of CNT modified polymers*. Composites Part B, 2017. **109**: p. 53.
159. R. Taherian, *Experimental and analytical model for the electrical conductivity of polymer-based nanocomposites*. Compos. Sci. Technol., 2016. **123**: p. 17.
160. T. C. Theodosiou, D. A. Saravanos, *Numerical investigation of mechanisms affecting the piezoresistive properties of CNT-doped polymers using multi-scale models*. Compos. Sci. Technol., 2010. **70**: p. 1312.
161. S. Xu, O. Rezvanian, K. Peters, M. Zikry, *The viability and limitations of percolation theory in modeling the electrical behavior of carbon nanotube–polymer composites*. Nanotechnology, 2013. **24**: p. 155706.
162. A. Amini, B. Bahreyni, *Behavioral model for electrical response and strain sensitivity of nanotube-based nanocomposite materials*. J. Vac. Sci. Technol., B, 2012. **30**: p. 022001.
163. N. Hu, Z. Masuda, C. Yan, G. Yamamoto, H. Fukunaga, T. Hashida, *The electrical properties of polymer nanocomposites with carbon nanotube fillers*. Nanotechnology, 2008. **19**: p. 215701.
164. N. Hu, Y. Karube, M. Arai, T. Watanabe, C. Yan, Y. Li, Y. Liu, H. Fukunaga, *Investigation on sensitivity of a polymer/carbon nanotube composite strain sensor*. Carbon, 2010. **48**: p. 680.
165. N. Hu, Y. Karube, C. Yan, Z. Masuda, H. Fukunaga, *Tunneling effect in a polymer/carbon nanotube nanocomposite strain sensor*. Acta Mater., 2008. **56**: p. 2929.
166. Z. Wang, X. Ye, *A numerical investigation on piezoresistive behaviour of carbon nanotube/polymer composites: mechanism and optimizing principle*. Nanotechnology, 2013. **24**: p. 265704.
167. R. Rahman, P. Servati, *Effects of inter-tube distance and alignment on tunnelling resistance and strain sensitivity of nanotube/polymer composite films*. Nanotechnology, 2012. **23**: p. 055703.
168. Y. Wang, G. J. Weng, in *Micromechanics and Nanomechanics of Composite Solids*, Springer, Cham, 2018, 123.
169. G. Ambrosetti, C. Grimaldi, I. Balberg, T. Maeder, A. Danani, P. Ryser, *Solution of the tunneling-percolation problem in the nanocomposite regime*. Phys. Rev. B, 2010. **81**: p. 155434.
170. Y. Wang, G. J. Weng, S. A. Meguid, A. M. Hamouda, *A continuum model with a percolation threshold and tunneling-assisted interfacial conductivity for carbon nanotube-based nanocomposites*. J. Appl. Phys., 2014. **115**: p. 193706.
171. J. G. Simmons, *Generalized formula for the electric tunnel effect between similar electrodes separated by a thin insulating film*. J. Appl. Phys., 1963. **34**: p. 1793.

172. R. Barrett, M. Berry, T. F. Chan, J. Demmel, J. Donato, J. Dongarra, V. Eijkhout, R. Pozo, C. Romine, H. Van der Vorst, *Templates for the solution of linear systems: building blocks for iterative methods*, SIAM, Philadelphia 1994.
173. A. Gbaguidi, S. Namilae, D. Kim, *Monte Carlo Model for Piezoresistivity of Hybrid Nanocomposites*. J. Eng. Mater. Technol., 2018. **140**: p. 011007.
174. M. Taya, W. Kim, K. Ono, *Piezoresistivity of a short fiber/elastomer matrix composite*. Mech. Mater., 1998. **28**: p. 53.
175. M. M. Shokrieh, R. Rafiee, *On the tensile behavior of an embedded carbon nanotube in polymer matrix with non-bonded interphase region*. Compos. Struct., 2010. **92**: p. 647.
176. M. A. Bhuiyan, R. V. Pucha, J. Worthy, M. Karevan, K. Kalaitzidou, *Defining the lower and upper limit of the effective modulus of CNT/polypropylene composites through integration of modeling and experiments*. Compos. Struct., 2013. **95**: p. 80.
177. E. Mohammadpour, M. Awang, S. Kakooei, H. M. Akil, *Modeling the tensile stress–strain response of carbon nanotube/polypropylene nanocomposites using nonlinear representative volume element*. Mater. Des., 2014. **58**: p. 36.
178. A. Ferreira, M. T. Martínez, A. Ansón-Casaos, L. E. Gómez-Pineda, F. Vaz, S. Lanceros-Mendez, *Relationship between electromechanical response and percolation threshold in carbon nanotube/poly(vinylidene fluoride) composites*. Carbon, 2013. **61**: p. 568.
179. L. Gao, X. Zhou, Y. Ding, *Effective thermal and electrical conductivity of carbon nanotube composites*. Chem. Phys. Lett., 2007. **434**: p. 297.
180. A. Lagarkov, A. Sarychev, *Electromagnetic properties of composites containing elongated conducting inclusions*. Phys. Rev. B, 1996. **53**: p. 6318.
181. L. Gao, Z. Li, *Effective medium approximation for two-component nonlinear composites with shape distribution*. J. Phys.: Condens. Matter 2003. **15**: p. 4397.
182. N. Hu, H. Fukunaga, C. Lu, M. Kameyama, B. Yan, *Prediction of elastic properties of carbon nanotube reinforced composites*. Proc. Royal Soc. A: Math. Phys. Eng. Sci., 2005. **461**: p. 1685.
183. J. Li, W. Ma, L. Song, Z. Niu, L. Cai, Q. Zeng, X. Zhang, H. Dong, D. Zhao, W. Zhou, *Superfast-response and ultrahigh-power-density electromechanical actuators based on hierarchal carbon nanotube electrodes and chitosan*. Nano Lett., 2011. **11**: p. 4636.
184. Y. Huang, S. Ahir, E. Terentjev, *Dispersion rheology of carbon nanotubes in a polymer matrix*. Phys. Rev. B, 2006. **73**: p. 125422.
185. P. Costa, J. Silva, A. Ansón-Casaos, M. T. Martinez, M. Abad, J. Viana, S. Lanceros-Mendez, *Effect of carbon nanotube type and functionalization on the electrical, thermal, mechanical and electromechanical properties of carbon nanotube/styrene–butadiene–styrene composites for large strain sensor applications*. Composites Part B, 2014. **61**: p. 136.
186. N. Tagmatarchis, M. Prato, *Functionalization of carbon nanotubes via 1, 3-dipolar cycloadditions*. J. Mater. Chem., 2004. **14**: p. 437.

187. T. Fujigaya, N. Nakashima, *Non-covalent polymer wrapping of carbon nanotubes and the role of wrapped polymers as functional dispersants*. *Sci. Technol. Adv. Mater.*, 2015. **16**: p. 024802.
188. S. Parveen, S. Rana, R. Fanguero, *A review on nanomaterial dispersion, microstructure, and mechanical properties of carbon nanotube and nanofiber reinforced cementitious composites*. *J. Nanomater.*, 2013. **2013**: p. 80.
189. B. Krause, M. Mende, P. Pötschke, G. Petzold, *Dispersability and particle size distribution of CNTs in an aqueous surfactant dispersion as a function of ultrasonic treatment time*. *Carbon*, 2010. **48**: p. 2746.
190. V. V. Gobre, A. Tkatchenko, *Scaling laws for van der Waals interactions in nanostructured materials*. *Nat. Commun.*, 2013. **4**: p. 2341.
191. C. Xue, G.-Q. Du, L.-J. Chen, J.-G. Ren, J.-X. Sun, F.-W. Bai, S.-T. Yang, *A carbon nanotube filled polydimethylsiloxane hybrid membrane for enhanced butanol recovery*. *Sci. Rep.*, 2014. **4**: p. 5925.
192. D. Kwon, T.-I. Lee, M. Kim, S. Kim, T.-S. Kim, I. Park, *Porous dielectric elastomer based ultra-sensitive capacitive pressure sensor and its application to wearable sensing device*, presented at *Solid-State Sensors, Actuators and Microsystems (TRANSDUCERS), 2015 Transducers-2015 18th International Conference on*, 2015.
193. Q. Li, Y.-L. Kang, W. Qiu, Y.-L. Li, G.-Y. Huang, J.-G. Guo, W.-L. Deng, X.-H. Zhong, *Deformation mechanisms of carbon nanotube fibres under tensile loading by in situ Raman spectroscopy analysis*. *Nanotechnology*, 2011. **22**: p. 225704.
194. Z. Zhao, K. Teng, N. Li, X. Li, Z. Xu, L. Chen, J. Niu, H. Fu, L. Zhao, Y. Liu, *Mechanical, thermal and interfacial performances of carbon fiber reinforced composites flavored by carbon nanotube in matrix/interface*. *Compos. Struct.*, 2017. **159**: p. 761.
195. J. Z. Kovacs, B. S. Velagala, K. Schulte, W. Bauhofer, *Two percolation thresholds in carbon nanotube epoxy composites*. *Compos. Sci. Technol.*, 2007. **67**: p. 922.
196. S. Yao, Y. Zhu, *Nanomaterial-enabled stretchable conductors: strategies, materials and devices*. *Adv. Mater.*, 2015. **27**: p. 1480.
197. C. Pang, J. H. Koo, A. Nguyen, J. M. Caves, M. G. Kim, A. Chortos, K. Kim, P. J. Wang, J. B. H. Tok, Z. Bao, *Highly Skin-Conformal Microhairry Sensor for Pulse Signal Amplification*. *Adv. Mater.*, 2015. **27**: p. 634.
198. G. Shi, Z. Zhao, J. H. Pai, I. Lee, L. Zhang, C. Stevenson, K. Ishara, R. Zhang, H. Zhu, J. Ma, *Highly sensitive, wearable, durable strain sensors and stretchable conductors using graphene/silicon rubber composites*. *Adv. Funct. Mater.*, 2016. **26**: p. 7614.
199. T. Yan, Z. Wang, Y.-Q. Wang, Z.-J. Pan, *Carbon/graphene composite nanofiber yarns for highly sensitive strain sensors*. *Mater. Des.*, 2018. **143**: p. 214.
200. B.-U. Hwang, J.-H. Lee, T. Q. Trung, E. Roh, D.-I. Kim, S.-W. Kim, N.-E. Lee, *Transparent Stretchable Self-Powered Patchable Sensor Platform with Ultrasensitive Recognition of Human Activities*. *ACS Nano*, 2015. **9**: p. 8801.

201. D. Chen, Q. Pei, *Electronic muscles and skins: A review of soft sensors and actuators*. Chem. Rev., 2017. **117**: p. 11239.
202. A. Atalay, V. Sanchez, O. Atalay, D. M. Vogt, F. Haufe, R. J. Wood, C. J. Walsh, *Batch Fabrication of Customizable Silicone-Textile Composite Capacitive Strain Sensors for Human Motion Tracking*. Advanced Materials Technologies, 2017. **2**: p.
203. X. Li, Z.-H. Lin, G. Cheng, X. Wen, Y. Liu, S. Niu, Z. L. Wang, *3D Fiber-Based Hybrid Nanogenerator for Energy Harvesting and as a Self-Powered Pressure Sensor*. ACS Nano, 2014. **8**: p. 10674.
204. Z. Niu, H. Dong, B. Zhu, J. Li, H. H. Hng, W. Zhou, X. Chen, S. Xie, *Highly Stretchable, Integrated Supercapacitors Based on Single-Walled Carbon Nanotube Films with Continuous Reticulate Architecture*. Adv. Mater., 2013. **25**: p. 1058.
205. C. Wong, Z.-Q. Zhang, B. Lo, G.-Z. Yang, *Wearable Sensing for Solid Biomechanics: A Review*. IEEE Sens. J., 2015. **15**: p. 2747.
206. P. Lee, J. Lee, H. Lee, J. Yeo, S. Hong, K. H. Nam, D. Lee, S. S. Lee, S. H. Ko, *Highly stretchable and highly conductive metal electrode by very long metal nanowire percolation network*. Adv. Mater., 2012. **24**: p. 3326.
207. T. Del Castillo-Castro, M. Castillo-Ortega, J. Encinas, P. H. Franco, H. Carrillo-Escalante, *Piezo-resistance effect in composite based on cross-linked polydimethylsiloxane and polyaniline: Potential pressure sensor application*. J. Mater. Sci., 2012. **47**: p. 1794.
208. L. A. Jandro, Y. K. César, P. T. Gilles, C. N. S. Emílio, *Strain gauge sensors comprised of carbon nanotube yarn: parametric numerical analysis of their piezoresistive response*. Smart Mater. Struct. , 2015. **24**: p. 075018.
209. G. Georgousis, C. Pandis, A. Kalamiotis, P. Georgiopoulos, A. Kyritsis, E. Kontou, P. Pissis, M. Micusik, K. Czanikova, J. Kulicek, M. Omastova, *Strain sensing in polymer/carbon nanotube composites by electrical resistance measurement*. Composites Part B, 2015. **68**: p. 162.
210. M. Park, H. Kim, J. P. Youngblood, *Strain-dependent electrical resistance of multi-walled carbon nanotube/polymer composite films*. Nanotechnology, 2008. **19**: p. 055705.
211. F. Michelis, L. Bodelot, Y. Bonnassieux, B. Lebental, *Highly reproducible, hysteresis-free, flexible strain sensors by inkjet printing of carbon nanotubes*. Carbon, 2015. **95**: p. 1020.
212. T. K. Kim, J. K. Kim, O. C. Jeong, *Measurement of nonlinear mechanical properties of PDMS elastomer*. Microelectron. Eng., 2011. **88**: p. 1982.
213. Q. Qin, Y. Zhu, *Static friction between silicon nanowires and elastomeric substrates*. ACS Nano, 2011. **5**: p. 7404.
214. J. Suhr, N. Koratkar, P. Koblinski, P. Ajayan, *Viscoelasticity in carbon nanotube composites*. Nat. Mater., 2005. **4**: p. 134.
215. L. Jin, C. Bower, O. Zhou, *Alignment of carbon nanotubes in a polymer matrix by mechanical stretching*. Appl. Phys. Lett., 1998. **73**: p. 1197.

216. C. Park, J. Wilkinson, S. Banda, Z. Ounaies, K. E. Wise, G. Sauti, P. T. Lillehei, J. S. Harrison, *Aligned single-wall carbon nanotube polymer composites using an electric field*. J. Polym. Sci., Part B: Polym. Phys. , 2006. **44**: p. 1751.
217. X. Li, R. Zhang, W. Yu, K. Wang, J. Wei, D. Wu, A. Cao, Z. Li, Y. Cheng, Q. Zheng, *Stretchable and highly sensitive graphene-on-polymer strain sensors*. Sci. Rep., 2012. **2**: p.
218. S. C. Mukhopadhyay, *Wearable sensors for human activity monitoring: A review*. IEEE Sens. J., 2015. **15**: p. 1321.
219. M. Amjadi, K. U. Kyung, I. Park, M. Sitti, *Stretchable, skin-mountable, and wearable strain sensors and their potential applications: a review*. Adv. Funct. Mater., 2016. **26**: p. 1678.
220. C. S. Boland, U. Khan, C. Backes, A. O'Neill, J. McCauley, S. Duane, R. Shanker, Y. Liu, I. Jurewicz, A. B. Dalton, *Sensitive, high-strain, high-rate bodily motion sensors based on graphene–rubber composites*. ACS Nano, 2014. **8**: p. 8819.
221. J. T. Muth, D. M. Vogt, R. L. Truby, Y. Mengüç, D. B. Kolesky, R. J. Wood, J. A. Lewis, *Embedded 3D printing of strain sensors within highly stretchable elastomers*. Adv. Mater., 2014. **26**: p. 6307.
222. Y. P. Lian, X. Zhang, F. Zhang, X. X. Cui, *Tied interface grid material point method for problems with localized extreme deformation*. Int. J. Impact Eng., 2014. **70**: p. 50.
223. M. A. Puso, T. A. Laursen, *A mortar segment-to-segment contact method for large deformation solid mechanics*. Comput. Methods Appl. Mech. Eng., 2004. **193**: p. 601.
224. K. Kim, J. Park, J.-h. Suh, M. Kim, Y. Jeong, I. Park, *3D printing of multi-axial force sensors using carbon nanotube (CNT)/thermoplastic polyurethane (TPU) filaments*. Sens. Actuators, A, 2017. **263**: p. 493.
225. C. Lozano-Pérez, J. Cauich-Rodríguez, F. Avilés, *Influence of rigid segment and carbon nanotube concentration on the cyclic piezoresistive and hysteretic behavior of multi-wall carbon nanotube/segmented polyurethane composites*. Compos. Sci. Technol., 2016. **128**: p. 25.